LIFETIME PREDICTION MODELING OF AIRFOILS FOR ADVANCED POWER GENERATION

by

Ventzislav Gueorguiev Karaivanov

Mechanical Engineer, Technical University, Sofia, Bulgaria, 1995

Submitted to the Graduate Faculty of

Swanson School of Engineering in partial fulfillment

of the requirements for the degree of

Doctor of Philosophy

University of Pittsburgh

2009

UNIVERSITY OF PITTSBURGH

SWANSON SCHOOL OF ENGINEERING

This dissertation was presented

by

Ventzislav Gueorguiev Karaivanov

It was defended on

June 16th, 2009

and approved by

Dr. Minking K. Chyu, Professor, Department of Mechanical Engineering and Materials Science

Dr. Brian Gleeson, Professor, Department of Mechanical Engineering and Materials Science

Dr. Patrick Smolinski, Professor, Department of Mechanical Engineering and Materials Science

Dissertation Director: Dr. William S. Slaughter, Professor, Department of Mechanical Engineering and Materials Science

LIFETIME PREDICTION MODELING OF AIRFOILS FOR ADVANCED POWER GENERATION

Ventzislav Karaivanov, PhD

University of Pittsburgh, 2009

The use of gases produced from coal as a turbine fuel offers an attractive means for efficiently generating electric power from our Nation's most abundant fossil fuel resource. The oxy-fuel and hydrogen-fired turbine concepts promise increased efficiency and low emissions on the expense of increased turbine inlet temperature (TIT) and different working fluid. Developing the turbine technology and materials is critical to the creation of these near-zero emission power generation technologies. A computational methodology, based on three-dimensional finite element analysis (FEA) and damage mechanics is presented for predicting the evolution of creep and fatigue in airfoils. We took a first look at airfoil thermal distributions in these advanced turbine systems based on CFD analysis. The damage mechanics-based creep and fatigue models were implemented as user modified routine in commercial package ANSYS. This routine was used to visualize the creep and fatigue damage evolution over airfoils for hydrogen-fired and oxy-fuel turbines concepts, and regions most susceptible to failure were indentified. Model allows for interaction between creep and fatigue damage thus damage due to fatigue and creep processes acting separately in one cycle will affect both the fatigue and creep damage rates in the next cycle. Simulation results were presented for various thermal conductivity of the top coat. Surface maps were created on the airfoil showing the development of the TGO scale and the Al depletion of the bond coat.

In conjunction with model development, laboratory-scale experimental validation was executed to evaluate the influence of operational compressive stress levels on the performance of the TBC system. TBC coated single crystal coupons were exposed isothermally in air at 900, 1000, 1100^{o}C with and without compressive load. Exposed samples were cross-sectioned and evaluated with scanning electron microscope (SEM). Performance data was collected based on image analysis. Energy-dispersive x-ray (EDX) was employed to study the elemental distribution in TBC system after exposure. Nanoindentation was used to study the mechanical properties (Young's modulus and hardness) of the components in the TBC system and their evolution with temperature and time.

TABLE OF CONTENTS

LIST OF TABLES

LIST OF FIGURES

PREFACE

This technical effort was performed in support of the National Energy Technology Laboratory's on-going research in aero-thermal-material integrated thermal protection under the RDS contract DE-AC26-04NT41817.606.01.01. The author would like to specifically acknowledge Mary Anne Alvin (NETL) for her continued support and help.

I would like to express my deepest gratitude to the Department of Mechanical Engineering and Materials science for the support and the opportunity to be part of and contribute to this project. More specifically to my advisor - Dr. William S. Slaughter for his invaluable guidance and providing an excellent atmosphere for research, and to the committee members - Dr. Minking K. Chyu, Dr. Brian Gleeson, and Dr. Patrick Smolinski for their contribution and guidance throughout.

I would like to acknowledge the work of Dr. Minking K. Chyu and his students - Danny Mazzotta, Sean Siw and Pavin Ganmol, on aero-thermal modeling of the hydrogen-fired and oxy-fuel turbine concepts without which our research could not have started.

I would like to thank to my friend Dr. Serge Sidorov and Dr. Ilya Avdeev (Ansys Inc.) for their guidance and help in becoming an Ansys user.

The author acknowledge the facilities, scientific and technical assistance of the Materials Micro-Characterization Laboratory of the Department of Mechanical Engineering and Materials

Science, Swanson School of Engineering, University of Pittsburgh, specifically to the Director of MMCL Dr. Jorg M.K. Wiezorek and Mr. Albert Stewart.

Special thanks to Dr. Meltem Yanar for her support throughout the experimental part of our project.

My deepest gratitude to all faculty and students at the Department of Mechanical Engineering and Materials Science.

Last but not least to my wife Mina Pantcheva M.D. and our families who made all this possible.

1.0 INTRODUCTION

The use of gases produced from coal as a turbine fuel offers an attractive means for efficiently generating electric power from our Nation's most abundant fossil fuel resource. The Department of Energy is developing key technologies that will enable advanced turbines to operate cleanly and efficiently when fueled with coal derived synthesis gas and hydrogen fuels [1]. Developing the turbine technology is critical to the creation of these near-zero emission power generation technologies.

The concept of ultra low or near-zero emission power generation has focused on an oxy-fuel combustion process that burns pulverized coal in a mix of oxygen and re-circulates waste gases to create a high concentration of carbon dioxide (CO_2) in the gases exiting the boiler. The exhaust stream of the oxy-fuel process is separated into concentrated CO_2 and water. The power generation turbine inlet temperature (TIT) is expected to reach 1760^{o}C [1].

Alternatively, hydrogen-fired turbine systems are conceptually based on a complex cycle composed of a closed Brayton cycle and a Rankine cycle. Hydrogen and oxygen are supplied as the fuel and oxidant, respectively, to a compressor, and burned in steam. The pressurized steam feed enters the turbine at about 1400°C [2].

Creep, fatigue, oxidation and hot corrosion of industrial land-based power generation gas turbines are the principal concerns, particularly in view of long-term operation (30,000 hrs) and operation with advanced combustion cycles that potentially target turbine inlet temperatures of more than 1400°C [3]. Single crystal Ni-based superalloys have been used for manufacturing turbine blades because they can withstand high temperatures and resist creep [4]. However,

when operating in advanced combustion cycles, exposed to turbine inlet temperature of more than 1400^{o}C, they will need appropriate thermal protection. Current technology employs different techniques simultaneously – external, internal cooling and thermal barrier coatings (TBCs) [5, 6]. Turbine blades are cooled by air extracted from the turbine compressor and directed through cooling passages designed into the component. The TBC system's role is thermal and, to some extent, oxidation protection. This system usually consists of an inter-metallic bond coat, a thermally grown oxide layer and a ceramic top coat. It is designed to have very low thermal conductivity as well as thermal expansion very close to that of the underlying superalloy substrate.

Every component is subjected to diverse potential failure processes, which require good understanding in order to properly model the system behavior under complex thermo-mechanical loading [5, 6]. Modeling of those processes is needed to guide the development and application of stable TBCs with better insulation properties, as well as implementation of acceptable internal component cooling techniques, in order to achieve extended operational life of oxy-fuel and hydrogen fired land-based turbines.

Previous models [7] for thermal-mechanical life prediction have typically assumed that the loading state of the turbine airfoil along its staking line does not deviate significantly from that at its midsection. Therefore, in order to lower computational cost, a two-dimensional thermo-mechanical analysis is performed on a representative cross section. Increasing the work fluid temperature and diversifying the chemical content changes the aerodynamic and thermal loading. This demands better understanding of the development and evolution of critical zones over the entire blade structure.

There are several models capable of good life prediction of the individual elements of the system but challenges are arising when combining the failure modes and effects of one constituent (i.e. TBC spalling) over the rest of the system. A good life prediction methodology could be an essential tool for improving design and material development.

Durability designs and component life assessment for advanced turbine airfoils subjected to high rotational speeds and gas temperatures require in-depth understanding of thermal-mechanical coupling on the fatigue and creep damage mechanisms in the superalloy substrate. Therefore, a modeling effort should start with a thorough study of the material structure, characteristics, creep, and fatigue capabilities. We used a damage mechanics approach for the failure models development. Starting with one-dimensional models for creep and fatigue, fitted well to experimental data, we extended them for three-dimensional use and implemented them as a user-modified routine for the commercial software package ANSYS. Thus, the models can readily be used for other similar applications. The models developed required information for the three-dimensional temperature, stress and strain fields. Thus, as a first step, the field calculations were performed, followed by determination of the local creep and fatigue damage in time and their interaction over the entire airfoil domain. Accomplishments in this area are discussed in Chapters 2 and 3. Micro-structural and phase changes in the ceramic top coat part of the TBC system, and their influence on all other damage mechanisms are discussed in Chapter 3.

In general, a TBC system reduces thermal load to the airfoil and oxidation and corrosion rate into the airfoil substrate [5, 6]. Typical thermal barrier coatings are made of a top layer of yttria stabilized zirconia (YSZ) and inter-metallic plasma sprayed bond coat (BC). During high temperature exposure the bond coat forms an Al-rich thermally grown oxide (TGO) scale and it

has a critical role in the failure of the TBC system [5, 6, 8, 9]. The goal is to achieve longer replacement intervals through a stable system and continuous protection. Maps are created on the surface of the airfoil showing the development of the TGO scale and the Al depletion of the bond coat. The modeling approach is based on the kinetics of the protective scale and uses performance data from the literature [10] and also from our own experimental work.

In conjunction with the model development, laboratory-scale experimental validation was executed to evaluate the influence of operational compressive stress levels on the performance of the TBC system. TBC coated single crystal coupons were exposed isothermally in air at 900, 1000, 1100^{o}C with and without compressive load. Exposed samples were cross-sectioned and evaluated using a scanning electron microscope (SEM). Performance data were collected based on image analysis. Electron dispersive spectrometry (EDS) was employed to study the elemental distribution in the TBC system after exposure. Nanoindentation was used to study the mechanical properties (Young's modulus and hardness) of the components in the TBC system and their evolution with temperature and time.

2.0 NICKEL BASED SUPERALLOYS

Single crystal nickel based superalloys are commonly employed as a high temperature creep and oxidation resistant blade alloys at the first stages of modern gas turbines. A *superalloy* is a metallic alloy which can be used at high temperatures, often in excess of 70% of their absolute melting temperature. Creep and oxidation resistance are usually the prime design criteria.

2.1 SUPERALLOY MICROSTRUCRURE

Superalloys can be based on iron, cobalt or nickel, the latter being best suited for aeroengine and advanced land based turbine applications. The essential solutes in nickel based superalloys are aluminum and/or titanium, with a total concentration which is typically less than 10 atomic percent. This generates a two-phase equilibrium microstructure, consisting of gamma (γ) and gamma-prime (γ'). It is the γ' which is largely responsible for the elevated-temperature strength of the material and its incredible resistance to creep deformation. The γ phase forms the matrix in which the γ' precipitates. The amount of γ' depends on the chemical composition and temperature [4, 11].

The single-crystal superalloys are often classified into first, second and third generation alloys. The second and third generations contain about 3 wt% and 6wt% of rhenium respectively. Rhenium is a very expensive addition but leads to an improvement in the creep

strength. Typical chemical composition of several first, second and third generation proprietary alloys are listed in table 1:

Table 1. Chemical composition of superalloys [4, 11].

Alloy	Cr	Co	Mo	W	Ta	Nb	Al	Ti	Re	Hf
CMSX2	8	4.6	0.6	7.9	5.8		5.6	0.9		
CMSX4	5.7	11	0.42	5.2	5.6		5.2	0.74	3	0.1
CMSX6	9.8	5	3		2.1		4.8	4.7		
CSMX10	2	3	0.4	5	8	0.1	5.7	0.2	6	0.03
Rene N5	7	8	2	5	7		6.2		3	0.2
Rene N6	4.2	12.5	1.4	6	7.2		5.75		5	0.15
RR2000	10	15	3				0.05	4		
SRR99	8.5	5		9.5	2.8		5.5	2.2		

Of particular modeling interest here are the CMSX-4 and Rene N5 alloys. Both of them are second generation (3% Re) and have comparable characteristics. The former has been extensively studied and experimental results were published in number of journal articles. The later is used by National Energy Technology Laboratory (NETL) as a substrate material.

For a given chemical composition, the fraction of γ' decreases as the temperature is increased. This phenomenon is used in order to dissolve the γ' at a sufficiently high temperature *(*a solution treatment*)* followed by ageing at a lower temperature in order to generate a uniform and fine dispersion of strengthening precipitates [11].

The γ-phase is a solid solution with a cubic-F (face centered) lattice and a random distribution of the different species of atoms. By contrast, γ' has a cubic-P (primitive cubic) lattice in which the nickel atoms are at the face-centers and the aluminum or titanium atoms at the cube corners. This atomic arrangement has the chemical formula Ni_3Al, Ni_3Ti or $Ni_3(Al,Ti)$. In addition to aluminium and titanium, niobium, hafnium and tantalum can partition preferentially into γ'. The γ phase has a random distribution of Ni, Al and Ti atoms, whereas the γ' has its nickel atoms located at the face-centers, as illustrated on Figure 1 a) and b).

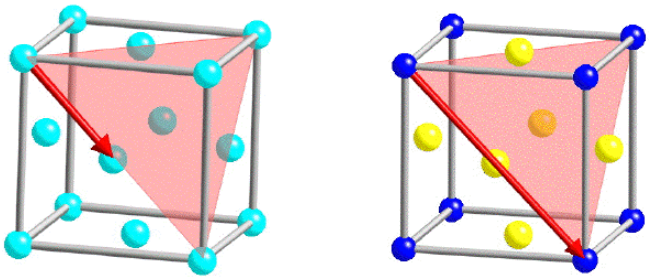

a) b)

Figure 1. Crystal structure of γ and γ'. Lattice vectors along <110> directions, lying on the {111} planes [11].

The γ phase forms the matrix in which the γ' precipitates. Since both the phases have a cubic lattice with similar lattice parameters, the γ' precipitates in a cube-cube orientation relationship with the γ. This means that its cell edges are exactly parallel to corresponding edges of the γ phase. Furthermore, because their lattice parameters are similar, the γ' is coherent with the γ when the precipitate size is small. Dislocations in the γ nevertheless find it difficult to penetrate γ', partly because the γ' is an atomically ordered phase. The order interferes with dislocation motion and hence strengthens the alloy.

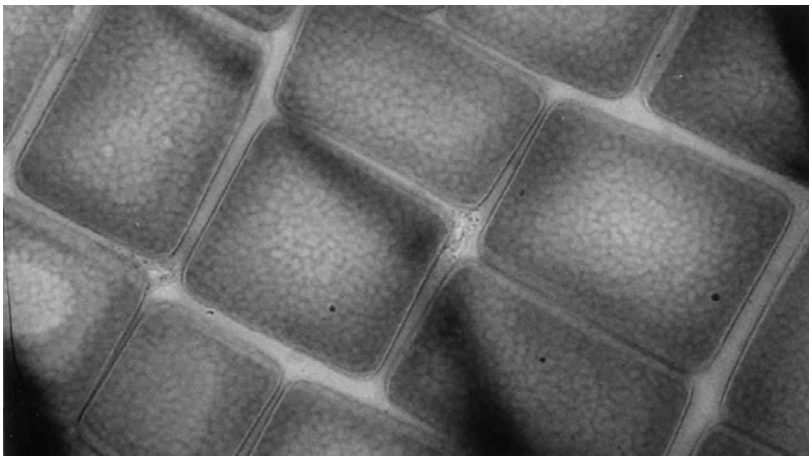

Figure 2. TEM of CMSX-4 γ / γ' microstructure, [12].

In all nickel based superalloys, the presence of the γ' phase hinders the motion of dislocations even though it is coherent with the matrix. This is because it has an ordered crystal structure. In

γ the Burgers vector of a dislocation is $\frac{a}{2}\langle 110\rangle$, which is, a lattice vector (fig. 1a) so that slip does not alter the crystal structure. However, for γ' $\frac{a}{2}\langle 110\rangle$ is not a lattice vector, actually $a\langle 110\rangle$ (fig. 1b) is the lattice vector for a primitive cubic lattice. It follows that the motion of an $\frac{a}{2}\langle 110\rangle_{\gamma}$ dislocation into the γ' will disrupt the order, leaving behind an anti-phase domain boundary. However, the passage of a second such dislocation through γ' on the same slip plane restores the order [4, 11]. As a consequence, the penetration of γ' has to occur by pairs of γ dislocations, or `super dislocations'. The requirement for pairing makes it more difficult for dislocations to penetrate the γ' and hence improves the resistance to creep deformation.

The small misfit between the γ and γ' lattices is important for two reasons. Firstly, when combined with the cube-cube orientation relationship, it ensures a low γ/γ' interfacial energy. The ordinary mechanism of precipitate coarsening is driven entirely by the minimization of total interfacial energy. A coherent or semi-coherent interface therefore makes the microstructure stable, a property which is useful for elevated temperature applications.

The magnitude and sign of the misfit also influences the development of microstructure under the influence of a stress at elevated temperatures. The misfit is said to be positive when the γ' has a larger lattice parameter than γ. The misfit can be controlled by altering the chemical composition, particularly the aluminum to titanium ratio. A negative misfit stimulates the formation of rafts of γ', essentially layers of the phase in a direction normal to the applied stress. This can help reduce the creep rate if the mechanism involves the climb of dislocations across the precipitate rafts.

The strength of most metals decreases as the temperature is increased, simply because assistance from thermal activation makes it easier for dislocations to surmount obstacles. However, nickel based superalloys containing γ', which essentially is an inter-metallic compound based on the formula $Ni_3(Al,Ti)$, are particularly resistant to temperature [11].

Ordinary slip in both γ and γ' occurs on the {111}<110>. If slip was confined to these planes at all temperatures then the strength would decrease as the temperature is raised. However, there is a tendency for dislocations in γ' to cross-slip on to the {100} planes where they have a lower anti-phase domain boundary energy. This is because the energy decreases with temperature. Situations arise where the extended dislocation is then partly on the close-packed plane and partly on the cube plane. Such a dislocation becomes locked, leading to an increase in strength. The strength, however, decreases beyond about 800^{o}C where the thermal activation is sufficiently high to allow the dislocations to overcome the obstacles.

In summary, the presence of γ' is responsible for the fact that the strength of nickel based superalloys is relatively insensitive to temperature. Figure 3 shows a plot of the ultimate tensile strength (UTS) versus temperature for four superalloys including the second generation CMSX-4 [12].

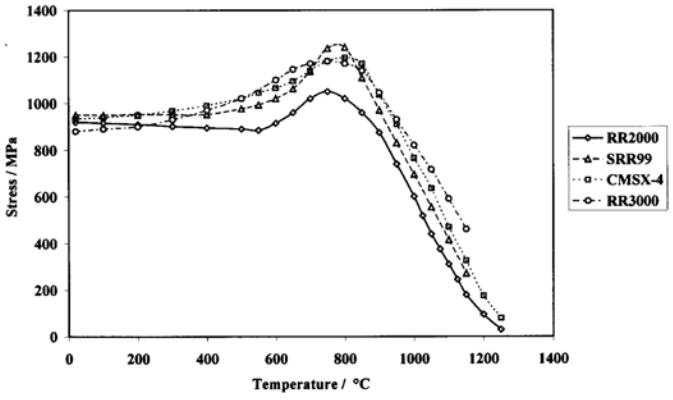

Figure 3. Experimental Ultimate Tensile Stress (UTS) values for four superalloys including single crystal CMSX-4. [12].

2.2 CREEP IN NICKEL SUPERALLOYS

The creep deformation behavior of single crystal superalloys is strongly temperature, stress, orientation and alloy dependant. They also exhibit the usual primary, secondary and tertiary creep behavior. There are two mechanisms of slip deformation dominating creep and plasticity of these superalloys. They occur under different operating conditions and are usually referred as Type I and Type II slip. The next two sections look into more details of both mechanisms and why they are important from modeling point of view.

2.2.1 Type I slip

This deformation mechanism occurs on <101>{111} slip system and is found under condition set of temperatures over 800^{o}C, lower stresses, and orientations close to <001> crystallographic axis [13]. It is responsible for the secondary or steady-state creep behavior. It results in stable homogeneous deformation, where all matrix channels are populated with dislocations, forming a three dimensional network which is then maintained throughout the steady-state creep. Precipitates are particularly resistant to Type I deformation except at very high stresses where a passage of dislocations results in anti phase boundary as explained in section 2.1. Figure 4a shows the effect of the magnitude of the applied stress on the creep strain evolution at 950^{o}C for samples within 10^{o} from <001>. There is strong dependence upon the stress level, however, there is a weak dependence upon disorientation from <001> axis as seen in figure 4b). In this regime creep strain rate increases monotonically with creep strain in a linear fashion.

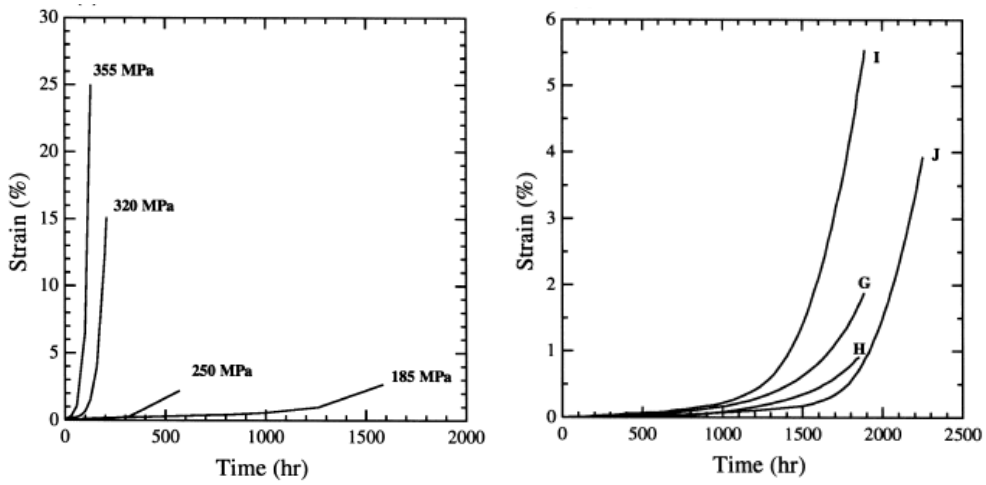

a) b)

Figure 4. a) Experimental creep curves from CMSX-4 tested at 950°C and various stress levels for orientation within 10° from <001>. **b)** at 185 MPa and varying angle away from<001>. [13].

2.2.2 Type II slip

This deformation mechanism occurs on <112>{111} slip system and is found under condition set of lower temperatures especially around 750°C and high stress. Type II slip has the ability to shear both the matrix (γ) and the precipitate (γ') phases, and it is responsible for the primary creep behavior. It is also favored by orientations more that 25 degrees away from <001> and for stress states with shear components. Figure 5 a) illustrates the effect of magnitude of the applied stress on creep strain evolution at 750°C. The creep strain is relatively insensitive to the magnitude of the stress once the stress level exceeds some border value between 600 and 750MPa. Figure 5 b) illustrates the effect of disorientation from <001>. Primary creep varies significantly for the same applied stress and different angle of orientation. Here K, L, M, and N samples have orientation respectively 5.27, 7.98, 17.47, and 19.83 degrees away from <001> [13].

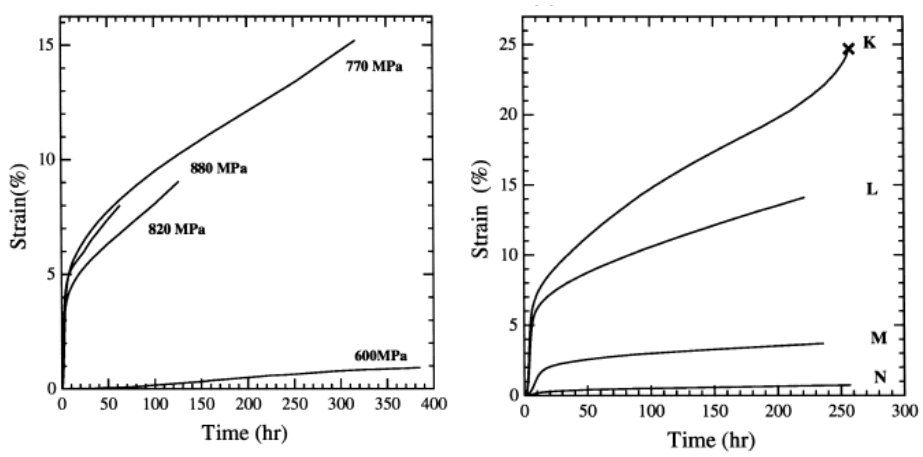

a) b)

Figure 5. Experimental creep curves from CMSX-4 tested at 750°C: **a)** at various stress levels for orientation within 10° from <001>. **b)** at 750 MPa and varying angle away from<001> [13].

Airfoils in advanced land based Hydrogen and Oxy-fuel turbine applications are projected to experience metal surface temperatures of 900-1100°C (as shown in section 2.5.3 and 3.2) on the outside metal interface and 550-800°C at the internal cooling channels core. Because of this wide range of temperatures within different parts of the component it is expected that both deformation mechanism described above will be active. The very high creep resistance of the modern single crystal superalloy for temperatures from 700 to 800°C is enabling the concept of internally cooled airfoils. Stress analysis of turbine blades shows that because of significant thermal stresses and stress redistribution from high temperature areas can increase the stresses experienced from the internal channels to 600 – 700 MPa and may be possible to exceed the border value and activate Type II deformation. MacLachlan et al. [12, 14-15] found that rupture life of CMSX-4 reduces from 5000h for 600MPa to 400h for 750 MPa at temperature of 750°C and attributed this change to orientation and the onset of deleterious type II slip mechanism.

2.3 FATIGUE IN SINGLE CRISTAL SUPERALLOYS

In general Fatigue damage is divided in *two types*:

High-cycle fatigue (HF) is a micro-structural damage mechanism that results from small stress amplitude cyclic loading, such as vibrations. Failure is expected after a relatively large number of cycles. 10^5 cycles is the dividing number between both types fatigue.

Low-cycle fatigue (LF) is a micro-structural damage mechanism that results form large stress amplitude cyclic loading. Failure is expected after a relatively short number of cycles. Very abrupt thermal changes, such as start and stop cycles are the usual driving force for this failure mode. Land-based turbine engines have very long running times in between very few start stop cycles. It is expected that low-cycle fatigue may not be a life limiting factor for most of these applications.

Since the amplitude of the cyclic loading has a major effect on the fatigue performance, the Stress-Number of cycles (S-N) relationship is usually determined for one specific loading amplitude. The amplitude is express as the R ratio value, which is the minimum peak stress divided by the maximum peak stress or

$$R = \frac{\sigma_{\min}}{\sigma_{\max}}, \tag{1}$$

where R=0 for "on-off" stress application, R=-1 for fully reversible loading and R=1 for no change in the applied stress.

MacLachlan et al. [16] performed series of interrupted and uninterrupted fatigue tests on CMSX-4. Here are some of the characteristic findings for HF and LF at different temperatures. Failure during HF cycling at 750 and 850^{o}C is entirely crystallographic. Initiation usually occurs at a casting pore at intersection of three crystallographic planes. For HF, from this point on,

failure is distinguished by whether the crystallographic surfaces are formed by cyclic crack growth or by catastrophic shear failure. At these lower temperatures, intense shear band are found on crystallographic planes and it is evident that crack growth occurs along these bands on the weakened planes. The crack usually forms vary late in life and it takes only one or two thousand cycles to propagate to sufficient length for failure.

For HF cycling at 950^{o}C failure is different from the lower temperatures. Initiation occurs at a casting pore in the center of a circular flat region. After a brief growth on crystallographic planes it adopts a planar growth (perpendicular to primary stress axis). When the crack reaches certain length is shears on different crystallographic planes during final shear and there are no indications for cyclic growth [16].

Low-cycle fatigue test usually show similar failure mechanisms at all temperatures. The crack initiates from pore or oxide spike, planar crack propagation follows, and final shear occurs on crystallographic planes. The difference in failure mechanism with increasing temperature are restricted to the method of initiation, where at 750^{o}C crack initiates internally, and at higher temperatures crack usually begins at oxide spike on the surface. Internal crack would grow radially, whether surface one would join few other smaller cracks and shear together.

2.4 DAMAGE MECHANICS

Concepts from continuum damage mechanics will be used in the development of the life prediction methodology. A brief overview of some of the relevant previous work involving damage mechanics follows.

Damage mechanics theory was developed over the last few decades by Kachanov, Lemaitre, and Chaboche [17-21], and has been applied to a wide variety of problems, as well as creep and stress-rupture of a range of materials.

For phenomenological descriptions of microstructural changes it is usual to introduce some internal variables. A damage parameter, ω, is a state variable and is a measure of change in the material from its fully heat-treated condition, which affects its ability to resist monotonic or cyclic deformation. It has a value of zero for undamaged material and a value of one at failure. However, failure usually occurs at values less than one and most models correct for this by use of an additional parameter. Because there is no recovery, ω is a monotonically increasing quantity.

Turbine blades are complex layered structures, operating in high temperature and stress fields, which are subject to different damage mechanisms. In cases where several mechanisms of damage occur simultaneously, each of them may be represented by a state variable ω_i. The choice of damage parameter is made by either a physical microstructural analysis or by generalization of experimental data. Kachanov considered the damage variable as a surface density of intersections and cavities, and in the simplest case it is a scalar function [19]. In general, different mechanisms of damage are discriminated both by the function used to describe how they evolve with time/cycles, and by the function used to describe how they affect material properties.

In order to describe the influence of damage on creep deformation, Kachanov and Rabotnov introduced a damage parameter in the creep equation, wherein the damage rate is a function of the damage state and operating conditions [19],

$$\frac{d\omega_{cr}}{dt} = g(\sigma, T, \omega_{cr}) \ . \tag{2}$$

Rabotnov introduced the concept of effective (actual) stress acting on a representative volume element as the nominal stress modified by the damage,

$$\sigma_{eff} = \frac{\sigma}{(1-\omega_{cr})} \ . \tag{3}$$

The stress-strain behavior of the material can be represented by the constitutive equation of the as-manufactured material with the stress replaced by the effective stress. It is also assumed that the rate of damage growth is controlled primarily by the level of actual stress [19]. If it is also assumed that the temperature locally is constant, a popular choice for the function describing damage evolution is [12, 14, 15, 19]

$$\frac{d\omega_{cr}}{dt} = C\left(\frac{\sigma}{1-\omega_{cr}}\right)^{v}, \tag{4}$$

where C and v are material parameters. This equation can easily be integrated analytically for ω_{cr} from 0 to 1, and for t between 0 and time to rupture T_r.

The substrate, or bulk material of a turbine blade for advanced turbines is usually a single-crystal superalloy, which in their second (René N5, CMSX-4) and third generation have excellent high-temperatures creep and fatigue resistance. MacLachlan, et al. [12, 14, 15], have applied continuum damage mechanics in life assessment models for stress rupture, creep and fatigue of first, second and third generation superalloys. Their formulation is based on modified Kachanov-Rabotnov equations and shows a very good ability to describe the evolution of

damage and strains as a function of time, temperature, and applied stress in uniaxial creep tests. Their version of equation (4) corrects for the fact that failure would occur as stress goes to infinity rather than ultimate tensile stress, and provides a correlation of short-term stress-rupture and tensile data and longer term creep data. MacLahlan et al. [12, 14, 15], have developed a damage mechanics based model for analyzing uniaxial behavior of superalloy single crystals, implemented on a slip system level and using single crystal plasticity theory. In order to account for the effects of rotation and bending, they modeled the entire creep specimen using finite element (FE) software and employing a user material subroutine. In this model they based damage accumulation on strain and strain rate [15].

Chaboche and Gallerneau applied damage mechanics models to evaluate durability at elevated temperatures. The continuum damage model is stress-based and assumes that the progressive deterioration processes can be described by scalar damage variables. Their formulation includes the interaction effect between creep, fatigue and oxidation for coated and uncoated superalloys through four separate damage variables [17].

2.4.1 Stress – Rupture Modeling

The creep damage model uses concepts from damage mechanics as explained above. The damage parameter is a state variable, ω_{cr}, and it is a measure of change in the material from its fully heat-treated condition which affects its ability to resist monotonic or cyclic deformation. In general, ω_{cr} varies from 0 to 1. However failure would actually occur before ω_{cr} reaches one.

As explained above, MacLachlan et al. [12, 14, 15] modified equation (4) as:

$$\frac{d\omega_{cr}}{dt} = C\left(\frac{\sigma_{eff}}{UTS - \sigma_{eff}}\right)^{v} . \tag{5}$$

Thus, the ultimate tensile strength (UTS) is used as an upper bound on rupture strength and the rate of damage accumulation. It is also consistent with the concept of effective stress and the principle of strain equivalence that the material should fail when the effective stress or the initial stress acting upon undamaged material reaches the UTS [12, 14, 15].

At creep failure the damage parameter $\omega_{cr} = \omega_{crf}$, thus

$$\sigma_{eff} = UTS = \frac{\sigma}{1-\omega_{crf}}, \omega_{crf} = \frac{UTS - \sigma}{UTS} , \tag{6}$$

provides a correlation of short-term stress-rupture and tensile data and longer-term creep data. By integrating equation (5) for $0 < \omega_{cr} < \omega_{crf}$ and $0 < t < T_r$, we have an expression for the total time to rupture in terms of applied stress and ultimate tensile strength:

$$T_r = \frac{\left(UTS - \sigma\right)^{v+1}}{C\left(v+1\right)UTS\,\sigma^{v}} . \tag{7}$$

The material parameter C is found empirically to follow a Boltzmann function of temperature:

$$C = \frac{1}{A\exp\left(\Delta H_1 / \bar{R}T\right) + B\exp\left(-\Delta H_2 / \bar{R}T\right)} . \tag{8}$$

It reflects the role of creep softening with temperature of the γ matrix on damaging the overall structure. The first term in the denominator of (8) accounts for this effect. Rafting, which is a diffusion controlled process, has the opposite effect on damage or reduced flow occurring in the vertical matrix channels, and thus an attenuation parameter is used. The second term in (8) describes the effect of rafting and the rate of attenuation again assumes a Boltzman temperature

function [12, 14]. $\bar{R}$ is the universal gas constant, T is the absolute temperature, A and B are material parameters. ΔH_1 is similar to the activation energy for self diffusion of nickel, ΔH_2 is the activation energy for attenuation of matrix flow. In general, these two energies are different as the diffusion processes involved in rafting are unlikely to be the same as those in creep. For second generation superalloys (CMSX-4) they have the same value of 278 (kJ/mol), which is similar for self diffusion of nickel. The constants A and B are found to be $3.1\text{x}10^{-10}$ and $2.63\text{x}10^{12}$, respectively. The material parameter v is independent of temperature and is 3.2 for CMSX-4. All of the above values are found to give good results for both CMSX-4 and third generation CMSX-10 for a temperature range of 1023 to 1423 K [12,14, 15].

The damage profile for constant initial stress can be obtained by integrating equation (5) up to time t and damage ω to derive an expression for the damage state:

$$\omega_{cr} = \omega_{cr\,f}\left[1-\left(1-\frac{t}{T_r}\right)^{1/(v+1)}\right], \tag{9}$$

where $\omega_{cr\,f}$ is given by (6).

As previously indicated, the damage parameter ω_{cr} will vary from 0, at $t=0$, to $\omega_{cr\,f}$ at $t=T_r$, where $\omega_{cr\,f}$ assumes values between 0 and 1, but depends on the initial stress state. Simplifying, we define damage D such that

$$D=\frac{\omega_{cr}}{\omega_{cr\,f}}, \tag{10}$$

And now D assumes value $D=0$ at $t=0$, and $D=1$ at $\omega_{cr}=\omega_{crf}$ or $t=T_r$. Figure 6 shows damage parameter evolution for several loading conditions at constant stress and temperature. This damage parameter will be used in presenting creep damage for Hydrogen and Oxy-fuel turbine applications.

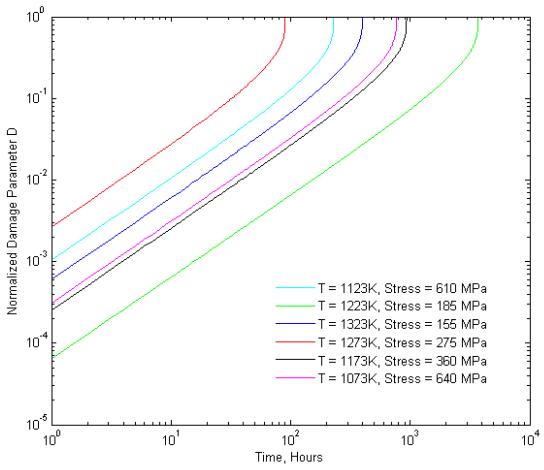

Figure 6. Damage parameter versus time at constant stress and temperature.

2.4.2 Creep Modeling

If it is assumed that the parameter controlling the evolution of damage during steady state and tertiary creep is the same as that controlling rupture life, the damage rate equation can also be coupled with a strain rate of similar form,

$$\frac{d\varepsilon_{cr}}{dt}=E_0\left[\frac{\sigma_{eff}}{UTS-\sigma_{eff}}\right]^u, \tag{11}$$

E_0 and u are another two material parameters in addition to C and v. C and v are usually determined first by the stress-rupture behavior, then E_0 and u are obtained from the shape and position of the creep curve [12,14, 15]. This equation is capable of modeling the secondary and

tertiary creep behavior, which is made possible because of the use of effective stress (3). Although UTS is temperature dependant, in order to model creep strain over wide range of temperatures, E_0 has to take several different values. To overcome this issue E_0 can take a form of activation function

$$E_0 = C_2 \exp\left(-\mathrm{V}H_1 \big/ \overline{R}T\right). \tag{12}$$

Equation (12) cannot model primary creep, and having in mind the complex behavior shown in figures 4 and 5, it will obviously be very difficult to find a single equation that can represent all three creep regimes over the entire range of temperatures and stresses. On first approximation Cunha et al. [22] used modified time hardening constitutive equation in a similar form to the one Chen et al. [23] used to model creep behavior:

$$\varepsilon_{cr} = \varepsilon_{pr} + \varepsilon_{ss} = C_1 \sigma^m t^n \exp\left(\mathrm{V}H_2 \big/ \overline{R}T\right) + C_2 \sigma^{m'} t \exp\left(-\mathrm{V}H_1 \big/ \overline{R}T\right), \tag{13}$$

where C_1, C_2, m, n, m' are material parameters, $\mathrm{V}H_1$ and $\mathrm{V}H_2$ are activation energies, and σ is the applied stress. This equation has two parts: the first one models primary creep as non-linear function of time and the second one models steady-state creep as a linear function in time. In general activation energies are not the same in order to have contributions from both parts $\left(\varepsilon_{pr} \text{ and } \varepsilon_{ss}\right)$ over different temperatures. In order to describe the steady-state over wider range of stresses we propose to modify ε_{ss} by changing the stress dependence as follows:

$$\varepsilon_{ss} = C_2 \left(\frac{\sigma}{UTS - \sigma}\right)^u t \exp\left(-\mathrm{V}H_1 \big/ RT\right). \tag{14}$$

This model has the advantages of simplicity and convenience for computation. Considering that large-scale plasticity or tertiary creep will not appear during service periods of turbine blades, the

first two creep stages are usually involved. However, if it is desired to model tertiary creep the applied stress can be substituted with the effective stress σ_{eff} (3) to give:

$$\varepsilon_{cr} = \varepsilon_{pr} + \varepsilon_{ss+ter} = C_1 \sigma_{eff}^{m} t^{n} \exp\left(VH_2 / \bar{R}T\right) + C_2 \left(\frac{\sigma_{eff}}{UTS - \sigma_{eff}}\right)^{u} t \exp\left(-VH_1 / \bar{R}T\right). \qquad (15)$$

Effective stress is used not only in the secondary but in the primary formulation because there are loadings combinations (low temperature / high stress, or Type II slip) where creep behavior changes from primary directly to tertiary, without any steady state region.

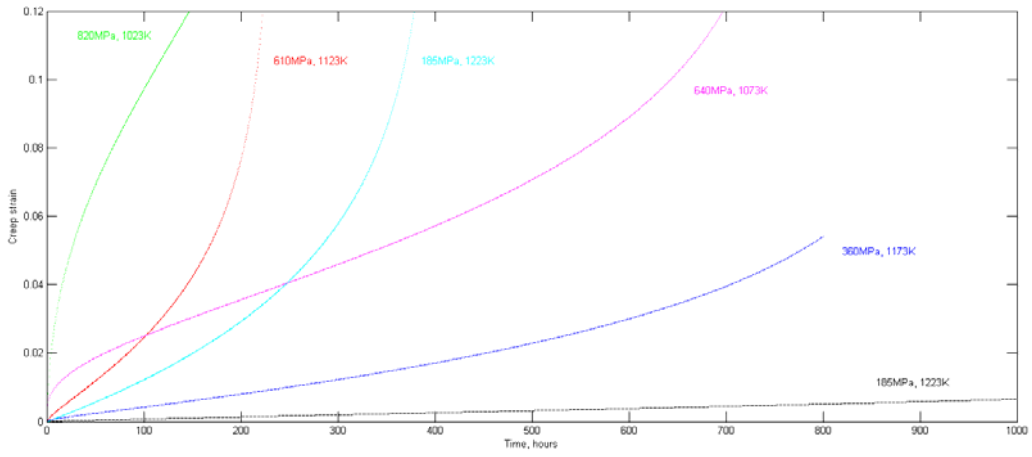

Figure 7. Creep strain versus time, modeled by equation (15), at different constant stresses and temperatures.

2.4.3 Fatigue Modeling

There are several different ways to approach fatigue modeling. For example, the commercial package ANSYS [24] has a fatigue module that can perform two type of analysis based on different loading type, mean stress effects and correction, only at predetermined points of interest. Claudio et al. [25] used finite element methods to obtain the *J* integral and stress intensity factor solutions for a disc with two types of cracks. Chen et al. [23] used FEA

simulation results to determine assessment positions and predicted the life of turbine blades using five different models for creep-fatigue interaction. Chaboche and Gallerneau [17] showed use of damage mechanics in creep-fatigue interaction.

As oppose to creep, where during tertiary creep multiple crack initiation occur and the creep failure is a result of linking of these cracks, at LF and HF cycle fatigue failure generally results from a single dominant crack. Despite the fact that the final failure is caused by a single macroscopic crack, fatigue damage accumulation in single crystals is controlled by initiation and can be regarded as a continuous process. The simplest form of linear damage accumulation is Miner's law, assuming that fatigue damage evolves linearly as a function of the life fraction, or:

$$\sum_i \frac{N_i}{N_{fi}} = 1, \tag{16}$$

where N_i is the number of cycles at certain stress level and N_f is the number of cycles to failure at that same stress level. In rate form this equation becomes:

$$\frac{d\omega_{fat}}{dN} = \frac{1}{N_f}, \tag{17}$$

where ω_{fat} is the fatigue damage state variable and it still evolves linearly. Where it is found that damage does not accumulate in liner fashion, as the case it is here, damage mechanics offers different formulation, expressing the cyclic life as a power function of the stress [18-21]:

$$\frac{d\omega_{fat}}{dN} = \frac{A\sigma^b}{\left(1-\omega_{fat}\right)^v}, \tag{18}$$

where A, b, and v are material parameters. In order to account for the stress level and allow for the effect of the mean stress to be included last equation can be written as [18-21]:

$$\frac{d\omega_{fat}}{dN}=\frac{A\left(\sigma_{\max}-\bar{\sigma}\right)^{b}}{\left(1-\omega_{fat}\right)^{v\left(\sigma_{\max},\bar{\sigma}\right)}}, \tag{19}$$

where $\bar{\sigma}$ is the mean stress and the damage variable is raised to a power which is function of the stress level. MacLachlan et al. evaluated different techniques to include the effect of the load ratio and found that using the Walker factor (w) is the best fit for relate the contributions of the stress range and the maximum stress to fatigue life. The Walker factor was first proposed to relate stress ration to crack propagation but is also used in fatigue lifing:

$$\sigma_{\max}\left(1-R\right)^{w}=\sigma_{\max}^{1-w}\Delta\sigma^{w}, \tag{20}$$

$$\frac{d\omega_{fat}}{dN}=A\left(\frac{\sigma_{\max}\left(1-R\right)^{w}}{1-\omega_{fat}}\right)^{v}. \tag{21}$$

In single crystal super alloy, as strain rate is increased in tensile testing, the value of the maximum tensile strength increases as well as the temperature at which it occurs. For LF, with typical low strain rates, yield strength increases slightly up to 700°C and then decreases. At HF, with typical high strain rates, both maximum yield stress and peak temperature are increased. To quantify this effect MacLachlan et al. [16] normalized the cyclic stress by the yield stress (0.1%) as a measure of the resistance of the material to micro-plasticity and crack initiation. And in order to quantify the effect of strain rate on yield strength they fit the yield strength as a function of strain rate and temperature as:

$$\sigma_{y,0.1\%}\left(\dot{\varepsilon},T\right)=A\exp\left(\frac{-\Delta Q_1}{\bar{R}T}\right)\left[1-\left(\frac{\dot{\varepsilon}}{\dot{\varepsilon}_0}\right)^{-B}\exp\left(\frac{-\Delta Q_2}{\bar{R}T}\right)\right]. \tag{22}$$

Here $A, B, \dot{\varepsilon}_0$ are material parameters, $\Delta Q_1, \Delta Q_2$ are activation energies, $\bar{R}$ and T are the gas constant and temperature respectively. The modified fatigue damage rate equation becomes [16]:

$$\frac{d\omega_{fat}}{dN} = A\left(\frac{\sigma_{\max}\left(1-R\right)^{w}}{\sigma_{y,0,1\%}\left(\&T\right)\left(1-\omega_{fat}\right)}\right)^{v}. \tag{23}$$

For cases when creep and fatigue processes occur simultaneously (ex. LF), there is a need to combine the effects of both on the overall damage of the material. The simplest way is to use linear accumulation of fatigue and creep through the use of combination of Miner's law for fatigue and Robinson's rule for creep. The combination of both leads to the linear life fraction rule:

$$\frac{1}{N} = \frac{1}{N_f} + \frac{1}{N_{cr}}, \tag{24}$$

where N_f, and N_{cr} are the number of pure fatigue cycles and number of cycle in pure creep respectively. Although been very popular, this equation does not predict any significant creep-fatigue interaction. However, if interaction does occur, eq. (24) can be modified as combination of the rates for fatigue and creep damage:

$$\begin{aligned} d\omega_{cr} &= f_{cr}\left(\sigma, \omega_{cr} + \omega_{fat}\right) \\ d\omega_{fat} &= f_{fat}\left(\sigma, \omega_{cr} + \omega_{fat}\right) \\ d\omega &= d\omega_{cr} + d\omega_{fat} = f_{cr}\left(\sigma, \omega\right) + f_{fat}\left(\sigma, \omega\right) \end{aligned} \tag{25}$$

where ω_{cr} and ω_{fat} are creep and fatigue accumulated damage. This way damage due to fatigue and creep processes acting separately in one cycle affects both the fatigue and creep damage rates in the next cycle and a synergism is created. The amount of creep-fatigue interaction depends on the individual accumulation laws chosen for both processes. MacLachlan et al. [16] have found that the amount of life reduction predicted by eq. (25) is not significant compared to the one from eq. (24), which could mean that there is no substantial interaction, and failure occurs either by creep of fatigue only.

2.4.4 Damage Equivalent Stress

Our concept is to apply this model at every material point (node) and thus obtain damage evolution over the entire airfoil domain. In order to be able to do that, we need to relate the three-dimensional state of stress experienced by every node to the uniaxial stress used to describe the above relations. Starting from the strain energy density release rate, Lemaitre and Desmorat [20, 21] defined a triaxiality function in order to find a damage equivalent stress. This damage equivalent stress is defined as the one-dimensional stress σ^* which, for the same value of the damage yields the same value of elastic strain energy density as that of a three-dimensional state. For the case of linear isotropic elasticity they defined:

$$\sigma^* = \sigma_{eq}\sqrt{R_v}\,, \tag{26}$$

$$R_v = \frac{2}{3}(1+\nu) + 3(1-2\nu)\left(\frac{\sigma_H}{\sigma_{eq}}\right)^2, \tag{27}$$

Where σ_H is hydrostatic stress and σ_{eq} is von Mises equivalent stress. However, since our material has cubic symmetry, we need to define a different function in order to relate both stress states. Starting again from the strain energy density release rate for anisotropic material, we then define strain energy density release rate for a material with cubic symmetry and for the degenerate case of uniaxial loading.

Energy density release rate: (J.L. Chaboche 1976):

$$Y = \rho\frac{\partial \psi_e^*}{\partial D} = \frac{\omega_e^*}{1-D}, \tag{28}$$

where ω_e^* is the elastic strain energy density, and for the case of anisotropic elasticity without any damage:

$$\omega_e^* = \frac{1}{2} S_{ijkl}\sigma_{ij}\sigma_{kl} = \frac{1}{2} S_{ijkl}\sigma_{ij}^D\sigma_{kl}^D + \frac{1}{2} S_{ijkl}\sigma_H^2\delta_{ij}\delta_{kl}\,, \tag{29}$$

$$\sigma_H = \frac{1}{3}\sigma_{kk}\,, \tag{30}$$

$$\sigma_{ij}^D = \sigma_{ij} - \sigma_H\delta_{ij}\,. \tag{31}$$

Next step is to define the damage equivalent stress σ^*, or the uniaxial stress which would give the same amount of elastic strain energy density as multiaxial state of stress following the approach of J. Lemaitre (isotropic):

From equation (28) and using the results: (A 1), (A 2):

$$Y = \frac{\omega_e^*}{(1-D)} = \frac{1}{2}\frac{S_{ijkl}}{(1-D)}\sigma_{ij}^D\sigma_{kl}^D + \frac{1}{2}\frac{S_{ijkl}}{(1-D)}\sigma_H^2\delta_{ij}\delta_{kl} =$$

$$= \frac{1}{2(1-D)}\left[\left(\sigma_{11}^{D^2} + \sigma_{22}^{D^2} + \sigma_{33}^{D^2}\right)S_{1111} + 2\left(\sigma_{11}^D\sigma_{22}^D + \sigma_{11}^D\sigma_{33}^D + \sigma_{22}^D\sigma_{33}^D\right)S_{1122} + 4\left(\sigma_{23}^{D^2} + \sigma_{13}^{D^2} + \sigma_{12}^{D^2}\right)S_{2323}\right] +$$

$$+ \frac{1}{2(1-D)}\frac{\sigma_{kk}^2}{9}\left[3S_{1111} + 6S_{1122}\right] =$$

$$= \frac{1}{2(1-D)}\left[\begin{array}{l}\left(\sigma_{11}^{D^2} + \sigma_{22}^{D^2} + \sigma_{33}^{D^2} + \frac{\sigma_{kk}^2}{3}\right)S_{1111} + 2\left(\sigma_{11}^D\sigma_{22}^D + \sigma_{11}^D\sigma_{33}^D + \sigma_{22}^D\sigma_{33}^D + \frac{\sigma_{kk}^2}{3}\right)S_{1122} + \\ +4\left(\sigma_{23}^{D^2} + \sigma_{13}^{D^2} + \sigma_{12}^{D^2}\right)S_{2323}\end{array}\right] \tag{32}$$

For the case of uniaxial stress, using the result of equation (A 8):

$$Y = \frac{1}{2(1-D)}S_{1111}\left(\sigma^*\right)^2 \tag{33}$$

After equating (32) and (33) and solving for equivalent stress σ^*:

$$\left(\sigma^*\right)^2 = \left(\sigma_{11}^{D^2} + \sigma_{22}^{D^2} + \sigma_{33}^{D^2} + \sigma_{kk}^2/3\right) + 2\left(\sigma_{11}^D\sigma_{22}^D + \sigma_{11}^D\sigma_{33}^D + \sigma_{22}^D\sigma_{33}^D + \sigma_{kk}^2/3\right)\frac{S_{1122}}{S_{1111}} +$$
$$+ 4\left(\sigma_{23}^{D^2} + \sigma_{13}^{D^2} + \sigma_{12}^{D^2}\right)\frac{S_{2323}}{S_{1111}} \tag{34}$$

where $\sigma_{ij}^{D} = \sigma_{ij} - \frac{\sigma_{kk}}{3}\delta_{ij}$ is the deviatoric stress, and S_{1111}, S_{1122}, and S_{2323} are the three independent constants of the compliance tensor characterizing cubic material. Elastic constants are also temperature dependant. This would be the stress value used in the calculations for creep strain and damage evolution.

2.5 FINITE ELEMENT IMPLEMENTATION

Implementation of the models described above is performed by using commercial software package ANSYS v.11 through the means of customizable user routine. Such approach allows us to use ANSYS's geometry integration, meshing algorithms, standard elements, robust solvers, visualizing capabilities, and post processing environment along side customized creep-fatigue routine that makes use of state variables, such as the creep and fatigue damage parameters. The next three subchapters are devoted to FE modeling, creation of the user modified creep-fatigue routine and results obtained by using this approach.

2.5.1 Finite element model, boundary conditions and loading steps

In order to reduce computational time, previous efforts for thermal-mechanical life prediction have typically assumed that the loading state of the turbine blade along its stacking line does not deviate significantly from that at its mid-section. Therefore, two-dimensional analysis was performed on this representative cross-section [7, 22]. Increasing the working fluid temperature and altering its chemical composition changes the aerodynamic and thermal loading, thus

demanding better understanding of the development and evolution of critical zones over the entire blade structure in order to evaluate the capability of proposed designs. Thus, three-dimensional analyses are required.

For simulation purposes, a solid model of the NASA E^3 blade was created using Pro/Engineer. Based on available data for the root, mean, and tip cross-sections and the corresponding diameters and stacking line a blend protrusion was created that formed the airfoil body [26]. With the geometry data available, the airfoil was created without its base and tip sections and with a "serpentine" geometry for internal cooling channels using the originally specified wall thickness. The "serpentine" cooling geometry stands for channels running alongside from the bottom to the top of the blade, and the cooling air can circulate the channels in many different ways depending on overall design. In general, this implies that the cooling air temperature and heat transfer coefficient are not constant through the length of the channel. The methodology could, however, be applied to other designs.

Table 2. Projected Gas composition (vol%), Turbine Inlet Temperature (K) and pressure (MPa) for Hydrogen and Oxy-fuel turbines [1].

	Hydrogen-fired Turbine	Oxy-fuel Turbine
Turbine Inlet Temperature, ^{o}C (K)	1425 (1698)	1760 (2033)
Turbine Inlet Pressure, MPa	2.07	4.3
Combustor Exhaust Composition, (%)	H_2O (17.3) CO_2 (1.4) O2 (8.2) N2 (72.2) Ar (0.9)	H_2O (75-90) CO_2 (25-10) O_2 N_2 Ar (1.7)

To begin the thermal-mechanical analysis of the solid substrate, the level of thermal load or heat transfer coefficient and pressure distributions on the airfoil's external surface were previously

determined via three-dimensional CFD simulation modeling using commercial package FLUENT [2, 7, 27]. Boundary conditions were made available for both Hydrogen-fired and Oxy-fuel turbines with projected gas compositions, turbine inlet temperature (TIT), and turbine inlet pressure as shown in Table 2.

Steady state thermo-mechanical analysis was performed using ANSYS. The airfoil geometry was imported into ANSYS and the entire volume meshed with tetrahedral elements. Two types of solid elements were used - structural Solid 187 and its thermal counterpart Solid 87. In order to apply the boundary conditions obtained from the CFD simulation (surface heat transfer coefficient and pressure), the entire surface was meshed with surface effects elements, namely Surf 154 and Surf 152. Approximately 576000 solid tetrahedral elements were used to mesh the blade volume and ~146000 3D surface effects elements were used to mesh all surface areas. In order to simulate the effect of the coating mass on the substrate under centrifugal loading from rotation the outside surface elements have mass assigned to them.

As the airfoil was modeled without the base and the tip section, in order to apply the mechanical constraints properly an extension was modeled such that the airfoil extended from the root cross-section. The length and form of this extension was created such that the effect of the boundary would be negligible on the blade volume (root to tip).

No layers have been created on the geometric model in order to model the presence and effect of the TBC. Rather, an overall effective heat transfer coefficient, related to the thermal resistance of the TBC, is imposed as a boundary condition on the external airfoil surface. Once the surface heat transfer coefficient on the airfoil is obtained from the FLUENT flow simulation, the effective heat transfer coefficient $(\bar{h})$ can be evaluated as follows:

$$\frac{1}{\bar{h}} = \left[\left(\frac{1}{h} \right) + \left(\frac{l_a}{k_a} \right) + \left(\frac{l_b}{k_b} \right) + \left(\frac{l_c}{k_c} \right) \right], \tag{35}$$

where h is the surface local heat transfer coefficient, and l and k are the thickness and thermal conductivity of each TBC layer, respectively. The properties of the yttria-stabilized zirconia (YSZ) based thermal barrier coating used in this effort are given in Table 3. This effective heat transfer coefficient and the local distribution of pressure determined from the CFD analysis were included as boundary conditions to the finite element model.

Table 3. TBC properties

	Thermal Conductivity, k [W/mK]	Thickness, l [μm]
Top Coat (a)	0.9	250
Thermally grown oxide (b)	0.9	10
Bond Coat (c)	1.7	100

The internal heat transfer coefficient depends strongly on the actual surface enhancement and the internal coolant passage design. Based on modern-day power turbine designs, the internal heat transfer coefficient (h_c) typically varies between 1000 and 3000 W/m^{2}K, and the coolant temperature (T_c) ranges between 800 and 1000 K. Here, as an approximation, a constant surface heat transfer coefficient is imposed on the internal surface of the airfoil. We considered two cases:

A - h_c = 1000 W/m^{2}K and T_c = 800 K, and

B - h_c = 3000 W/m^{2}K and T_c = 800 K for Hydrogen turbine,

and only B for Oxy-fuel turbine.

On the tip cross-section of the airfoil and the external areas of the extension no heat transfer is assumed.

An angular velocity of 376.8 rad/s (3600 rpm) is applied with respect to an axis of rotation, where the root radius is 0.6m. This completes the boundary condition statement.

The airfoil's substrate is modeled as a single-crystal superalloy which has cubic symmetry and the <001> crystallographic axis is coincident with the pull direction of the centrifugal force experienced by the blade. Material parameters used are those of the second-generation Ni-based superalloy CMSX-4 [28]. Since material parameters are temperature dependant, care is taken to specify this relation properly for elastic constants, density, thermal expansion, and thermal conductivity.

Finite element analysis is performed in three steps. First, a thermal solution is generated. After solving for the thermal distribution, it is later imposed as a body force loading. Together with the pressure load determined form CFD simulation and the angular velocity, they complete the loading for the subsequent step - a static, elastic structural analysis. Additionally, we assume and also verify that the stress is below the yield stress corresponding to the temperature thus this initial instantaneous response is entirely elastic. Third step is time dependant creep-fatigue analysis described in the next section.

2.5.2 User creep-fatigue routine

The creep damage model, described in sections 2.3.1-2.3.3, can be implemented as a post processor based on results from FEA simulation in either FEA package itself or other program, MatLab for example. However, this approach leads to over estimation of creep damage because the effect of stress relaxation is not included. In order to include this effect, we developed a creep-fatigue user routine for ANSYS which simulates the creep strain based on the model

described above, and calculates the damage equivalent stress, the damage parameter, and its evolution simultaneously.

The fatigue damage method based on equations (22) and (23) was implemented as a part of the time dependant user routine for ANSYS, where both damage accumulations can be computed simultaneously with or without interaction between them. This approach allows us to monitor creep and fatigue damage evolution at every time step over the whole blade domain. Creep and fatigue damage parameters are monotonically increasing and assigned to user state variables recorded at the end of each time step. Subsequent time steps use this end values as an initial condition to build up upon, thus preserving the loading history. Thus we have the opportunity to change the loading (or boundary conditions) at subsequent time steps and not lose the damage history. This routine is called at every element integration point. Creep and fatigue damage can be allow to interact at the required level with respect to different assumptions for material behavior. This way damage due to fatigue and creep processes acting separately in one cycle affects both the fatigue and creep damage rates in the next cycle and a synergism is created. Implementation based on this approach allows us to calculate fatigue damage caused from one loading ratio at a single simulation run. If it is assumed that there is no significant creep-fatigue interaction then two separate accumulation rules can be used as:

$$d\omega_{cr} = f_{cr}(\sigma, \omega_{cr}), \quad d\omega_{fat} = f_{fat}(\sigma, \omega_{fat}) .$$

In this case the fatigue model can be implemented in such way that in a single simulation several load ratios / frequencies can be evaluated. In this effort we implemented the fatigue damage accumulation for four loading cases where the loading ratios were assumed to be uniform over the entire airfoil, and the local $\sigma_{\max}$ was the same for all simulations.

These ratios and frequencies were:

- R = 0 at 1 cycle / hour
- R = 0.33 at 1 cycle / 6 hours
- R = 0.95 at 100Hz
- R = 0.85 at 100Hz,

thus representing two low cycle and two high cycle fatigue cases. Loading ratios were achieved by imposing different variations on the maximum stress.

User routines for ANSYS v.11 are written in Fortran, then by using Intel Fortran compiler a custom ANSYS executable is created, which is later used to run the program. As with all customizable features rigorous verification is left to the user. Verification at varying temperatures and stress loads was done by simulating one directional loading on three dimensional bar meshed with the same element used for meshing the volume of the airfoil. Results matched analytical solution for time steps up to 0.25 hours. The one exception is found to be equi-axed hydrostatic compressive pressure. This is because the creep models in ANSYS are plastic models and therefore assumed incompressible.

The third load step – time dependant creep-fatigue analysis uses the results obtained from the first two load steps and depending on the technological cycle can simulate different loading time lengths. This routine is called at every element integration point. The modified usercreep.F file is included in Appendix B. The version listed uses equation (14) to calculate strain increment. Sample input illustrating the use of state variables for the above routine is listed at the end of Appendix B.

2.5.3 Finite Element Modeling Results – Hydrogen-fired turbine

Results from the FEA first step – thermal solutions are shown in figures 8 and 9 for Hydrogen turbine projected operating conditions and internal cooling heat transfer coefficient h_c respectively 1000 and 3000W/m^{2}K. The later h_c value represents the current state of the art capabilities to enhance surface heat transfer. External film cooling is not considered in these two cases. Plot shows the pressure and suction sides of the airfoil, as well as cross section perpendicular to the stacking line at 30 mm from the root (approximately in the middle). It is found that in the second case the maximum temperature does not exceed 904^{o}C (1177K). For the materials of interest (CMSX-4, Rene N5) this would allow longer running times if all boundary conditions do not change in time. However, as discussed in the next chapter this may not be the case because the thermal conductivity of the YSZ ceramic coating can change with its exposure to elevated temperature.

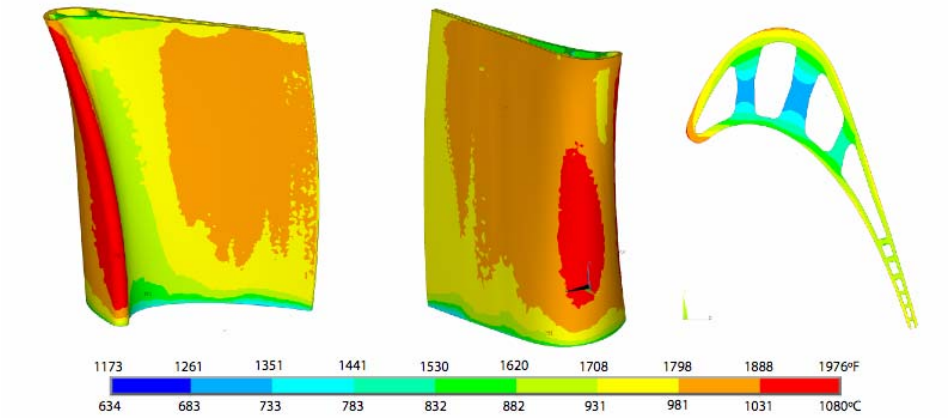

Figure 8. Temperature distribution for Hydrogen turbine, h_c = 1000W/m^{2}K .

Highest temperatures are found on the leading edge and first part of the suction side. This is also where it is usual to consider for external film cooling. Through thickness gradient is found to be

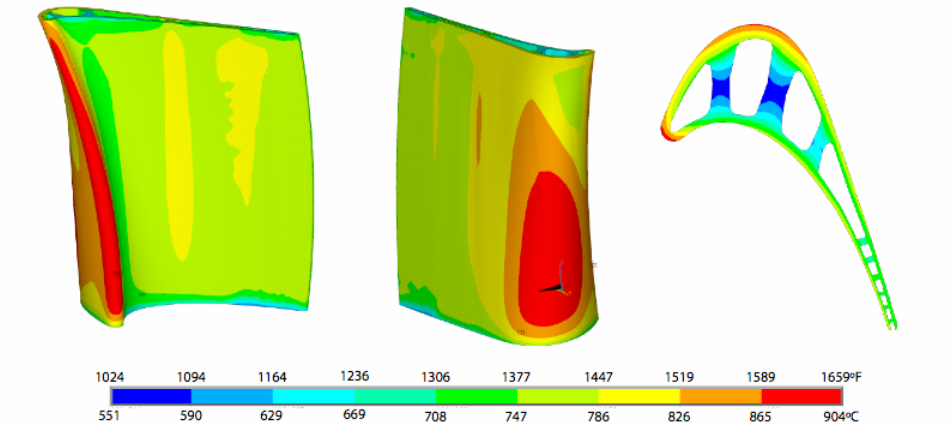

Figure 9. Temperature distribution for Hydrogen turbine, $h_c = 3000 W/m^2K$.

highest at the leading edge. The lowest temperatures are found in the internal ribs where conditions are created for type II slip and consequent creep damage.

Based on the temperature distribution, pressure loading and angular velocity a stress distribution is obtained in the second loading step. Von Mises stress is shown for this initial loading in figure 10 under "0 hours". As described earlier at this point the time dependant analysis begins. Results for stress distribution following relaxation from creep strain at three different running times can be seen in the plots to the right in figure 10.

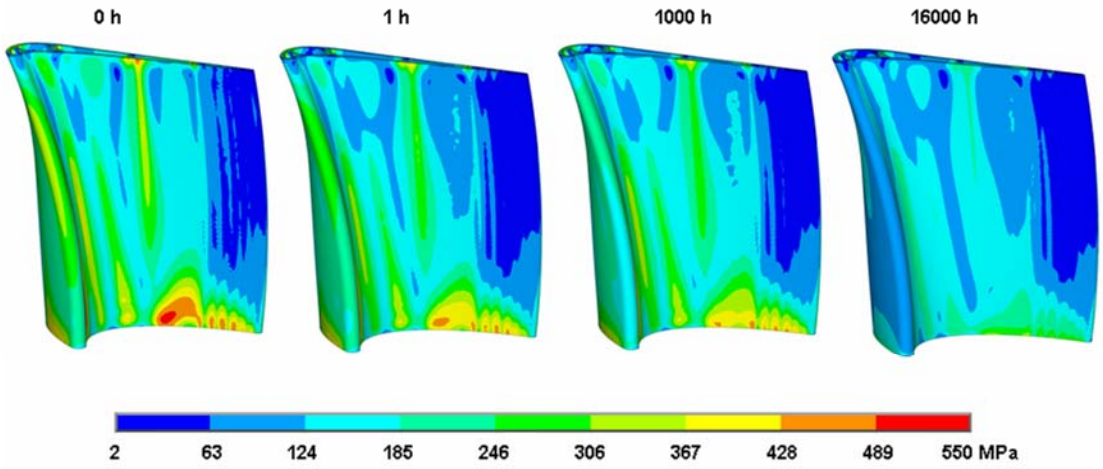

Figure 10. Stress distribution for Hydrogen turbine in MPa, for $h_c = 3000 W/m^2K$.

Simultaneously creep damage evolution has been calculated be the user creep-fatigue routine and is results are presented on figure 11 for hydrogen turbine. Simulation was extended to 16000 hours or approximately two years. Results are presented in color plot and the scale is logarithmic. At 16000 hours the highest creep damage developed at the surface of the suction side where we find high stresses combined with high temperature. However, there is no significant damage being developed through thickness. Although this surface area indicates high creep accumulation, it is very important to look at the actual damage values or replot on different scale. The highest creep damage in the area of interest was found to be *D=0.23*, which indicates that the material response is still in the steady state region. Reaching value of *D=~0.5* would indicate a transition to the highly non-linear tertiary creep state.

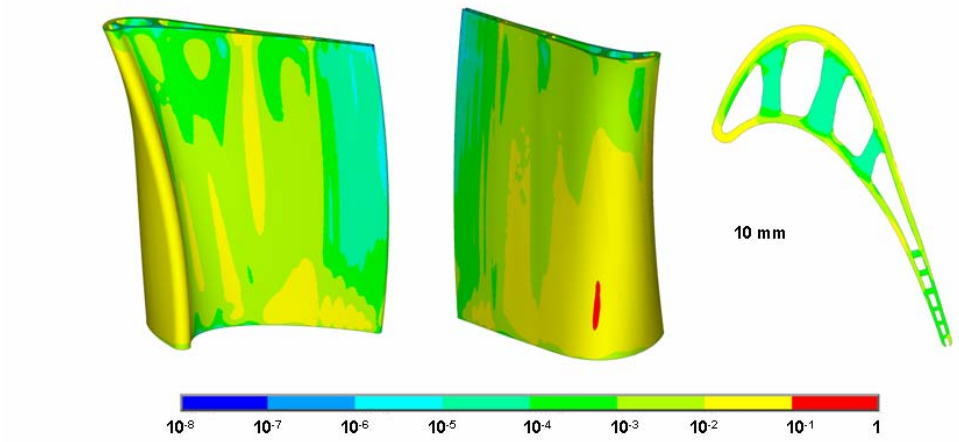

Figure 11. Creep damage evolution for Hydrogen turbine at 16000 hours, for $h_c = 3000 W/m^2K$.

Fatigue damage was calculated simultaneously over the whole blade for four loading ratios at three frequencies. By far the highest fatigue damage was found for loading ratio of zero or load unload variation, simulation a shut down and restart process. As expected, highest values are found at the greatly stressed parts of the blade.

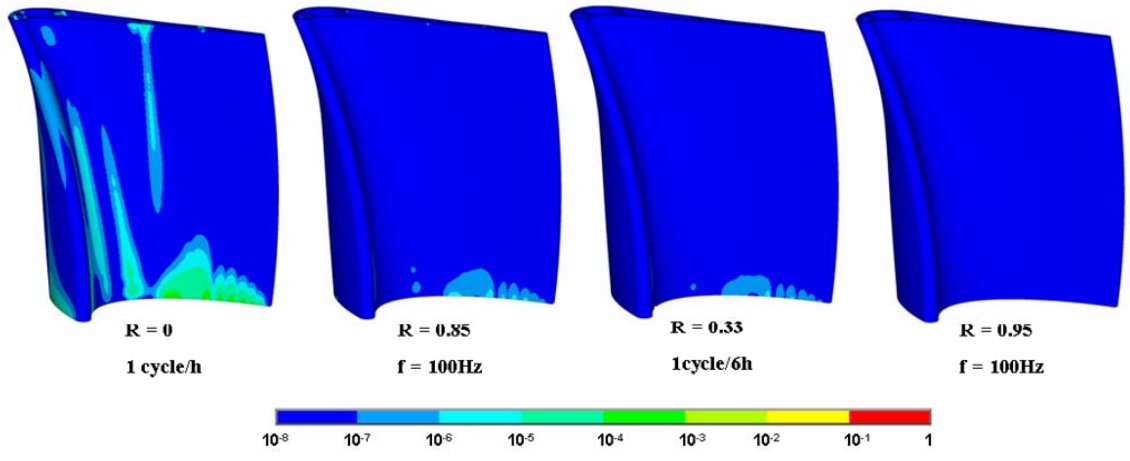

Figure 12. Fatigue damage evolution for Hydrogen turbine at 16000 hours, for $h_c = 3000 W/m^2K$.

The highest fatigue damage was found to be orders of magnitude lower than damage from creep. There was no interaction between creep and fatigue in this case. This was considered after tests were run on a small model to evaluate the possible interaction for the temperatures and stresses found in our model. In figure 13 a) we see the damage evolution for creep and fatigue allowed to develop without interaction. In fig. 13 b), damage from both creep and fatigue affects the damage evolutions in the next cycle. Until the creep damage enters a tertiary phase very small influence is found on the fatigue damage evolution. On other hand, fatigue damage values are orders of magnitude lower than creep thus they have very little influence on creep damage evolution. Because of this we did not allow for interaction in this simulation and thus were able to evaluate four (possibly more) loading ratios at once. Otherwise four runs would be needed.

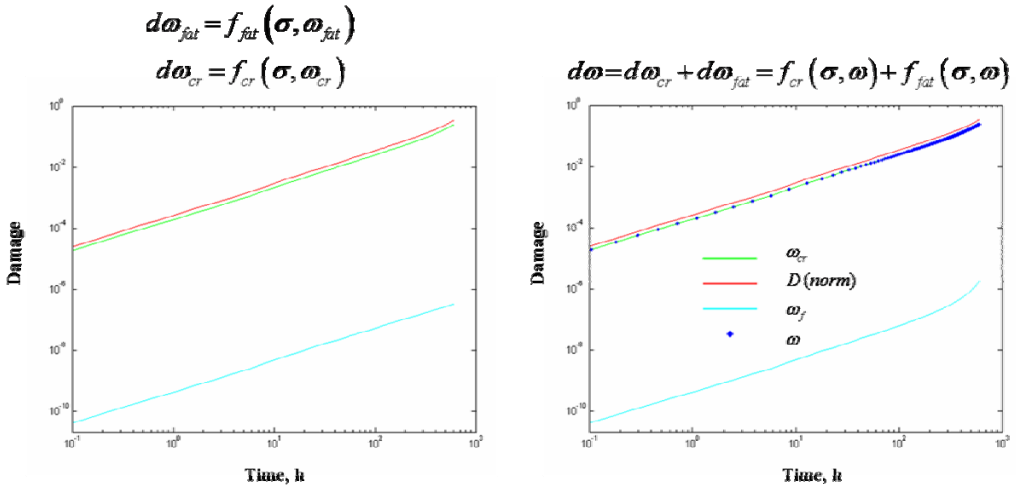

Figure 13. Creep-fatigue interaction:

a) no interaction;

b) Damage from creep and fatigue in one cycle affects the overall damage in the next cycle.

Calculations for 250MPa maximum stress at 950^{o}C and loading ratio R = 0.

3.0 AIR PLASMA SPRAYED YSZ TOP COAT

YSZ ceramic top coat is applied over the bond coat by either Electron-Beam Physical Vapor Deposition (EB-PVD) or Air Plasma Spray (APS). The final result from the former method has a "tooth" like structure with cracks oriented vertically, and the later method produces structure with cracks embedded in it (splat boundaries) and parallel to the surface. The top coat is designed to have a low thermal conductivity, high oxygen permeability, high coefficient of thermal expansion, and strain tolerant. These goals are achieved by depositing a structure that contains a large number of cracks and pathways. However, both micro-structure and phase composition are dynamic during service. Both methods have their advantages, with EB-PVD being favored for aeroengine applications because of its better surface roughness and higher adhesion strength. APS applied YSZ have a lower thermal conductivity, are less expensive, and preferred for land-based applications [5, 6].

3.1 APS YTTRIA STABILIZED ZIRCONIA

3.1.1 Phase change

During deposition the molten YSZ undergoes rapid cooling upon impact with the bond coat and forms yttria-rich non-equilibrium phase. This phase contains 7 wt% yttria, whether the $Y_2O_3 - ZrO_2$ phase diagram (fig. 14) would predict tetragonal $t - ZrO_2$ to contain 4wt% yttria.

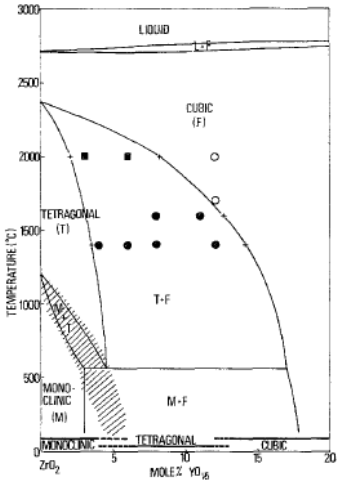

Figure 14. $Y_2O_3 - ZrO_2$ phase diagram [29].

Upon heating, the excess yttria starts diffusing out until it reaches an equilibrium concentration. That concentration is dependant on the heat treatment temperature. The yttria that diffuses out forms a new $c - ZrO_2$ phase with approximately 14 wt% Y_2O_3. According to Trice *et al*.[30], this conversion happens at ~50 hours exposure to 1200°C for the system they tested. After exposure to 1400°C final transformation would take place with the tetragonal phase completely transformed to monoclinic $m - Y_2O_3$ and cubic $c - ZrO_2$.

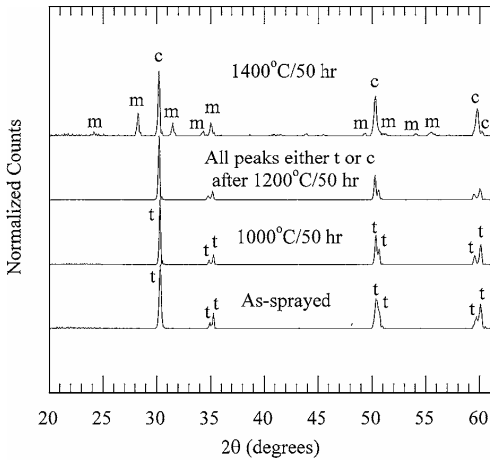

Figure 15. X-ray diffraction pattern of YSZ, as processed and after heat treatment [30].

3.1.2 Micro-structure changes

In as sprayed condition, the YSZ has lamellar morphology with each lamella comprised of columnar grains, submicron porosity between adjacent lamellae - intra-lamellar porosity, as seen on figure 16, and intra-lamellar cracks. Trice et al. have found that after exposure to 1000°C for 50 hours, intra-lamellar cracks are closed but the long columnar grains and lamellar

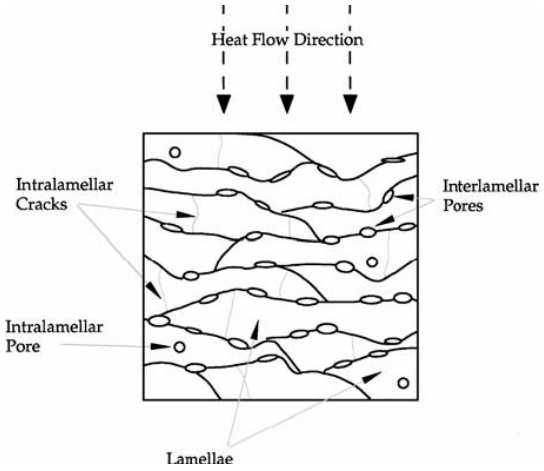

Figure 16. APS YSZ schematic microstructure [23].

morphology are still present. After exposure to 1200°C for 50 hours, the lamellar morphology is largely eliminated by changes in the grain shape with some elongated grains still present ($t-ZrO_2$) but mostly replaced by equiaxed grains ($c-ZrO_2$). After 50 hours at 1400°C, the grains are rounded with porosity at triple points of grain clusters.

3.1.3 Thermal conductivity

In thermal insulators as ZrO_2, heat transported by lattice vibrations and radiation. This means that thermal conductivity can be reduced by increasing phonon or photon scattering in the lattice structure of the ceramic [5]. Thermal conductivity of the sprayed YSZ is reduced compared to that of the sintered bulk $Y_2O_3-ZrO_2$ by the various defects in the microstructure introduced by the application process. Most significant contribution in lowering the thermal conductivity comes from porosity and microcracks oriented perpendicular to the direction of heat flow through the coating. Changes in the shape, distribution and surface area of the defects that occur during upon exposure to high temperature alter the thermal conductivity. Figure 17 shows plots of thermal conductivity versus temperature for YSZ as processed and heat treated.

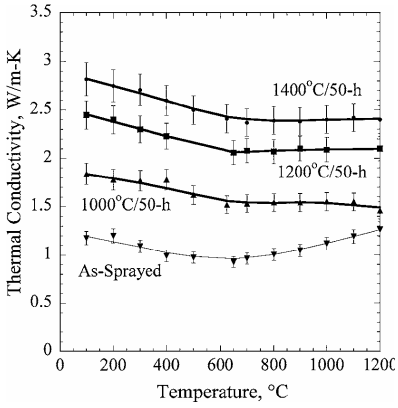

Figure 17. YSZ thermal conductivity versus temperature [30].

The increase of thermal conductivity at 1000°C is attributed to the intra-lamellar microcracks closure. Since they are oriented mostly normal to the coating surface their relative contribution is not expected to be big, but crack scatter around the normal increases it. Further increase of conductivity at 1200°C is attributed to the reduction of porosity as a result of sintering between the adjacent lamellae. At 1400°C, the increase of conductivity is attributed to the phase change from $t-ZrO_2$ to $m-ZrO_2$, as explained in the two previous sub-chapters, because significant volume fraction of the coating is replaced by a phase with higher conductivity. The thermal conductivity of 98% dense $m-ZrO_2$ at 800°C is 3.6 W/mK compared to 2.8 W/mK for similar density $t-ZrO_2$.

3.2 MODELING CHALLENGES

As shown, both YSZ's micro-structure and phase composition are dynamic during service. Taking into account YSZ's role in the TBC system, these changes mean that the thermal load on the airfoil will evolve in time. Changed stiffness of the YSZ top coat should also be expected as a direct result of densification, which may affect the TGO/YSZ interface and adherence. So far, for all modeling results presented, it was assumed that the thermal conductivity of the top coat is constant in time and has a value of *k=0.9 W/mK,* presenting the best possible value. Obviously, this is simplification which can be justified in some cases but ultimately will lead to over estimation of the component capability.

To illustrate the significance of this factor we completed simulations where the thermal conductivity of the top coat was assumed to be *k=1.5, 2.1, and 2.4 W/mK*, corresponding to 50

hours of exposure at 1000°C, 1200°C, and 1400°C respectively [30]. Results from the thermal solution over the airfoil for Hydrogen turbine projected conditions are presented in figures 18 and 19.

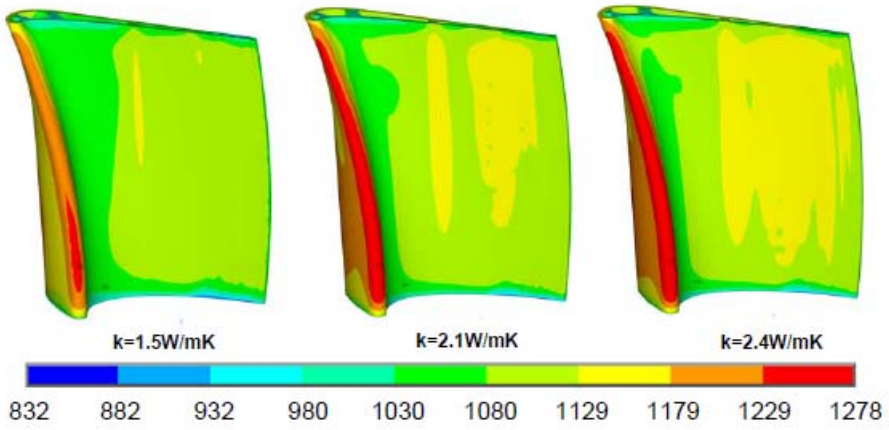

Figure 18. Temperature distribution, K. Hydrogen turbine, with thermal conductivity of the top coat k = 1.5, 2.1, and 2.4 W/mK.

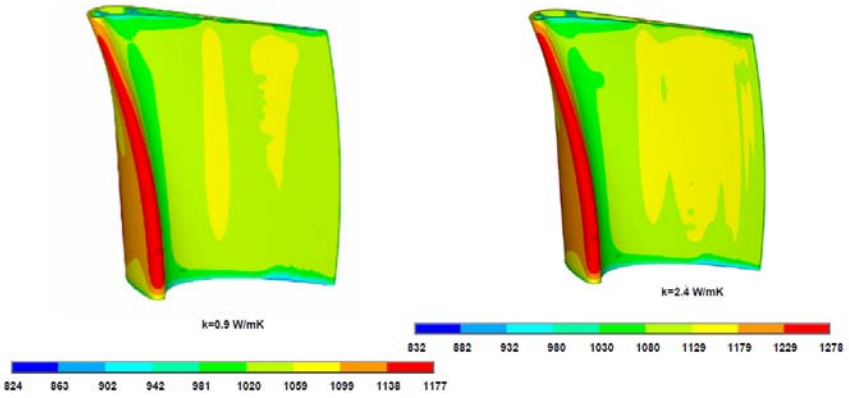

Figure 19. Temperature distribution, K. Hydrogen turbine, with thermal conductivity of the top coat k = 0.9 and 2.4 W/mK.

It is clearly shown that maximum temperature on the leading edge has increased by 100 degrees for k=2.4 W/mK. Thermal distribution is also different over the airfoil. Since all failure mechanisms discussed so far are, indeed, temperature dependant, the effects of YSZ property changes should be included in the modeling process based on availability of performance data

for the YSZ in the expected working temperature window. Some newly developed high purity APS coatings sintering and phase transition were found not significant if the YSZ temperature does not exceed 1300^{o}C [31]. For hydrogen-fired turbine that might not be an issue, however, the oxy-fuel's turbine inlet temperature is significantly higher and more attention is needed to ensure this requirement is satisfied.

3.3 OXY-FUEL TURBINE MODELLING

In this chapter we look in more detail at the oxy-fuel turbine. TBC material parameters used in this effort are listed in table 4. Thermal conductivity of the bond coat is taken at it maximum reported value. Conductivity for the YSZ is assumed at 1.0 W/mK as for advanced coating being continuously kept under 1300^{o}C [31].

Table 4. TBC properties

	Thermal Conductivity, k [W/mK]	Thickness, l [μm]
Top Coat (a)	1.0	250
Thermally grown oxide (b)	1.0	5
Bond Coat (c)	35	200

Figure 20 shows substrate temperature distribution for Oxy-fuel turbine with h_c = 3000W/m^{2}K. For lower values of h_c the maximum metal surface temperature will far exceed current material capabilities. Even at the maximum temperature of 1115^{o}C the component will have short life due to significant creep damage. It is obvious that with the metal surface temperature at this level the top coat temperature will also exceed the allowed maximum of 1300^{o}C. Figure 21

shows the temperature distribution on the surface of the YSZ assuming that its thermal conductivity is still k=1.0 W/mK. The maximum surface temperature is 1606°C.

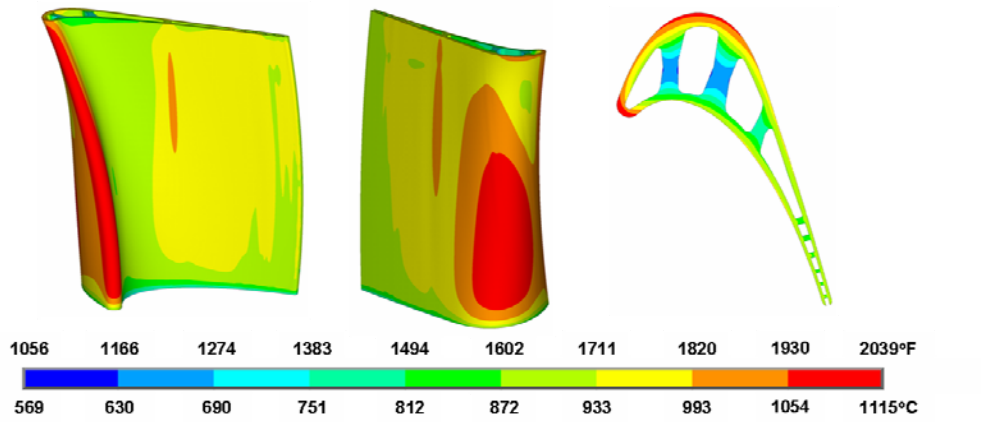

Figure 20. Substrate temperature distribution for Oxy-fuel turbine, h_c = 3000W/m^{2}K.

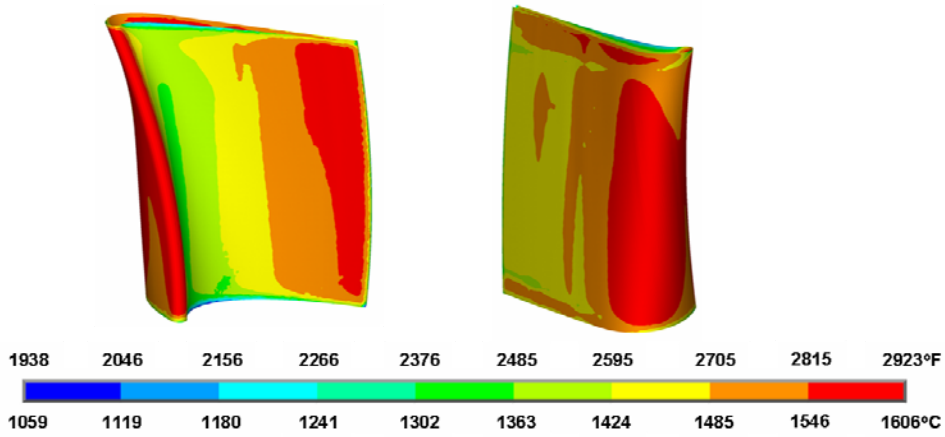

Figure 21. YSZ surface temperature distribution for Oxy-fuel turbine.

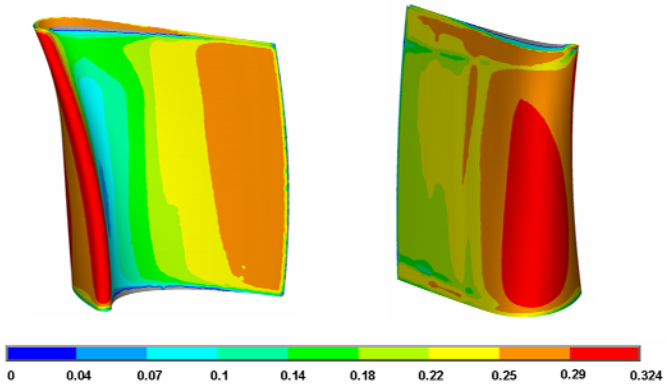

Figure 22. Minimum cooling effectiveness required to maintain YSZ temperature under 1300°C.

A combination of two possible solutions was considered: a low conductivity overlay coating and external film cooling. It was determined that the overlay coating could not, by itself, reduce the thermal load to an acceptable level. However, by introduction of external film cooling on the airfoil surface, it was shown that film cooling could, by itself, reduce the thermal load to acceptable level. On the other hand, one needs to consider the turbine loses associated with the cooling. External film cooling is achieved by placing cooling holes in the path of the hot gas ahead of areas with high temperature. It is possible to calculate a minimum external film cooling effectiveness that is required to maintain YSZ surface temperature as prescribed. Results of such calculation are shown in figure 22. With this level of cooling the maximum YSZ temperature is 1292^{o}C. If we recalculate the substrate temperature distribution, as shown in figure 23, we find a maximum temperature of 953^{o}C or 163^{o}C lower than before. It is also believed that the YSZ thermal conductivity can be maintain at the currently assumed k=1.0 W/mK.

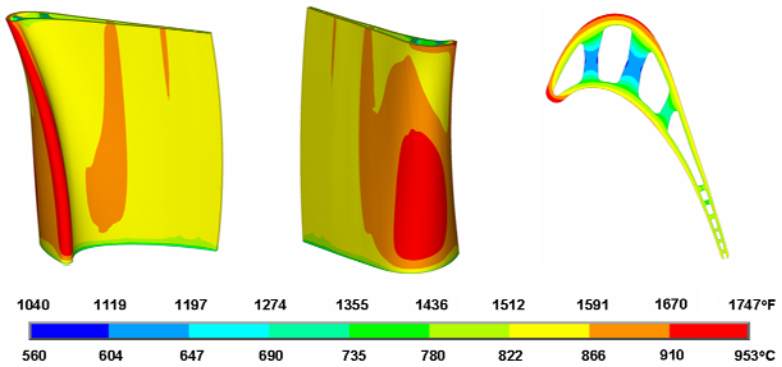

Figure 23. Substrate temperature distribution for Oxy-fuel turbine with external film cooling and $h_c = 3000 W/m^2K$.

With this new thermal loading we can run the creep-fatigue user routine and evaluate creep and fatigue damage for the oxy-fuel turbine. This simulation was extended to 800 hours where the first significant creep damage accumulation was found, similarly to the hydrogen turbine at 16000 hours. Compared to the hydrogen-fired turbine here the maximum temperature is 50^{o}C

higher and we find comparable level of damage accumulation 20 times faster. Here we find the maximum damage on the pressure side surface in areas that do not have much higher temperature but significant stresses initially. These stresses also drive the fatigue damage accumulation at those same spots. These stresses can be alleviated by change in the design as the internal cooling channels in our model blade are more or less arbitrary. Creep damage is D=~0.2 at these spots which is still in the steady state part of the creep curve.

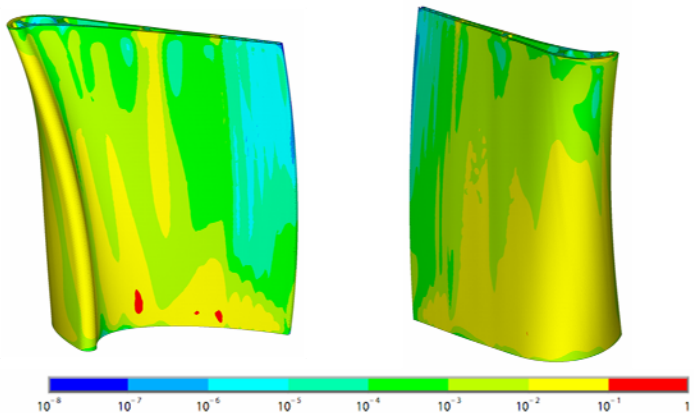

Figure 24. Creep damage evolution for oxy-fuel turbine with external film cooling at 800 hours.

Fatigue damage accumulation is again found biggest for R=0, where now its rate is faster but still orders of magnitude lower than this of creep damage. This means that failure would either be creep or fatigue related and no significant interaction is expected.

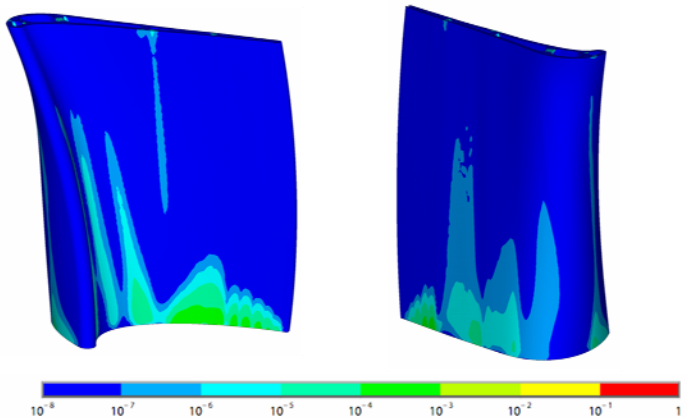

Figure 25. Fatigue damage for Oxy-fuel turbine, R=0.

4.0 THERMAL BARRIER COATINGS

Typical thermal barrier coatings are made of a top layer of yttria stabilized zirconia (YSZ) and a inter-metallic plasma sprayed bond coat (BC). Functionally the TBC system should provide low thermal conductivity and long life on a super alloy substrate.

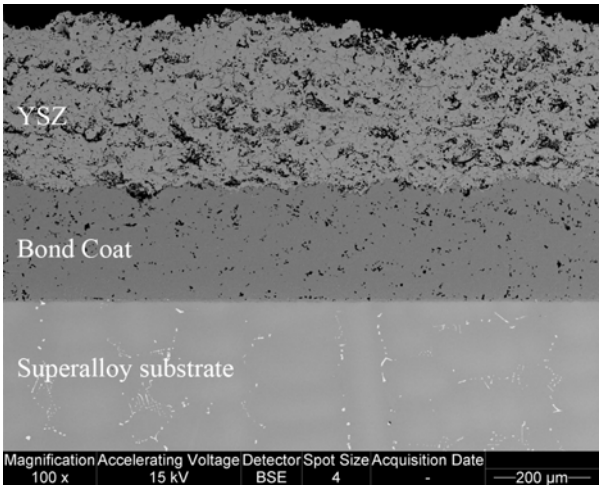

Figure 26. TBC system on Rene N5 superalloy: MCrAlY bond coat and YSZ top coat in as processed condition. (TGO is not present)

During high temperature exposure, the inter-metallic bond coat forms a thermally grown oxide scale (TGO) that consists predominantly of alumina. The formation of the TGO is found to have a critical role in the failure of the TBC system. The usual mechanism of failure is associated with spallation at or close to the TGO interfaces with YSZ or the bond coat. In the next two sections focus at the structural and functional changes in both: the YSZ and bond coat / TGO as well as modeling approaches to predict failure of TBC system.

4.1 THERMALLY GROWN OXIDE

Primary function of the bond coat is to protect the underlying substrate material from oxidative attack. The reliability of TBC systems is critically dependant on the oxidation behavior of the bond coat. In perfect conditions, the bond coat is expected to form a protective, slow-growing, non-porous, free of defects, and adherent $\alpha - Al_2O_3$ scale layer on its interface with the YSZ. Establishment of an aluminum rich scale depends on availability of critical content of aluminum, the structure of the alloy, and the oxidation conditions, in particular temperature and oxygen partial pressure. The growth of the TGO during isothermal oxidation can also be characterized by three stages [5, 10]:

- Transient – during this initial high temperature exposure stage a transient, heterogeneous scale is formed, constituting of several transitional Al_2O_3 structures such as $\gamma, \delta, and\ \theta$. These metastable structures grow at a faster rate than $\alpha - Al_2O_3$ and can considerably influence the overall amount of oxidation and the subsequent growth of stable $\alpha - Al_2O_3$ phase. Later transformation of metastable $\theta - Al_2O_3$ to the stable $\alpha - Al_2O_3$ produces 8-13% volume reduction, which can result in tensile stresses and cracking in the scale. In general this stage could last from seconds to hundreds of hours.
- Steady state – this stage begins with establishment of slow growing, long-term stable phase.
- Breakaway stage – this stage is characterized by the failure of the steady state phase and formation of less protective scales.

When the effects of property mismatch are combined with volumetric changes associated with the oxide formation, especially when the later are accompanied by a constrained expansion of the TGO, large stresses can develop upon cooling, which can lead to the nucleation of cracks at or near the interfaces of the oxide [32]. The magnitude of these stresses depends on the interface morphology, TGO thickness, temperature and on accumulated exposure time, and material properties. However, it is difficult to determine the relative effects of these factors, since all mechanisms are strongly coupled. Bond coat oxidation is believed to be one of the major degradation mechanisms controlling the lifetime of the TBC systems. The influence of oxidation has been described by the TGO thickness in most references, but in general there is no agreement on a single thickness value. Some publications are reporting thickness values as low as 3μm and as high as 10μm to have detrimental effect, whether others report even higher thicknesses without failure. It is obvious that TGO thickness should be evaluated as a system dependant and that adherence of the BC/TGO/YSZ interfaces should play an important role to describe the system failure. However, there is still a need to model the oxidation process properly in order to evaluate its contribution to the overall failure.

4.2 KINETICS OF THE THERMALLY GROWN OXIDE

The exposure of the bond coat – YSZ interface to elevated temperature and oxygen leads to formation of thermally grown oxide. The TGO grows in two directions – internally and externally. Next two sub-sections discuss the kinetics of both and the modeling approach.

4.2.1 External TGO growth and modeling

Externally, the TGO grows from the TGO/YSZ interface towards the YSZ. This is a compact oxide layer and its thickness is only slightly increasing with time, and usually consists of Al_2O_3. Depending on the system, it will be the only oxide visible for the first few hundred hours of exposure.

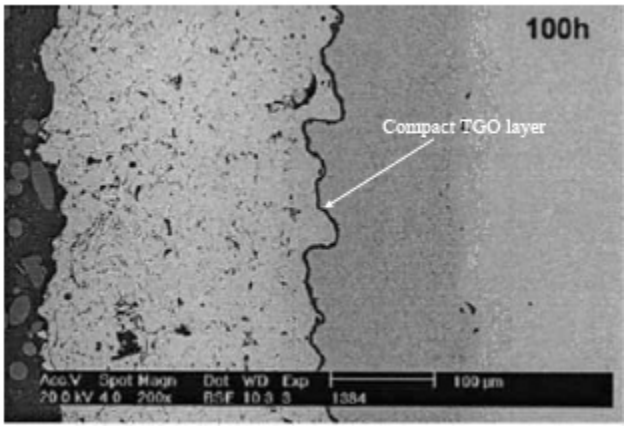

Figure 27. SEM of Compact TGO scale in 300μm APS YSZ system exposed to 1000°C for 100h [10].

It is possible after observing oxidation behavior for one particular system under several different temperatures and time exposures to obtain an average values for the compact scale thickness. This thickness can be fitted to equation of the type:

$$h = \left[t \exp\left(\frac{-Q}{\overline{R}T} \right) \right]^n . \tag{36}$$

Here h is the scale thickness, t is exposure time, Q is activation energy, $\overline{R}$ is universal gas constant, T is the temperature, and n is an exponent approximately equal to 0.33. This type equation was used by Meyer et al. [33] and later by other authors in slightly different form. We decided to use the following form (after [10]), which is dimensionally correct and straightforward:

$$h_{ox}(t,T) = K_n(T)\left(\frac{t}{t_0}\right)^n . \tag{37}$$

Here t_0 is for normalizing time, n has the same value, and $Kn(T)$ is temperature dependant growth rate constant as:

$$K_n(T) = K_0 \exp(-E_A / \bar{R}T), \tag{38}$$

where K_0 is a constant [m], E_A is activation energy [J mol^{-1}]. Echsler et al. observed the behavior of several TBC systems and were able to get an average values for the growth rate constant, as shown in Figure 28:

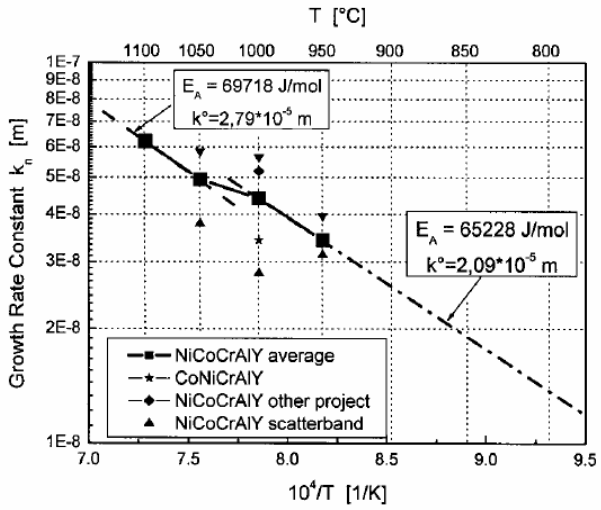

Figure 28. Temperature dependant growth rate constant for compact oxide scale [10].

The diagram clearly shows different rate of growth below 1000°C – suggesting the formation of metastable alumina, and over 1050°C – formation of stable $\alpha - Al_2O_3$.

We have implemented the approach based on equations (37) and (38) as a post-processor (in ANSYS) to the thermal solution for Hydrogen fired and Oxy-fuel turbines. Figure 29 a) shows the compact TGO thickness for Hydrogen turbine projected condition after 16000 h of exposure based on the above published data. A maximum thickness of 12.6 μm is attained at the areas exposed to the higher thermal load – at the leading edge and part of the suction side. We

have assumed that the thermal protection ability of the YSZ has not changed for the entire length of exposure. However, as shown in chapter 3.2, this may be underestimation because of increased thermal conductivity of the YSZ. It is also assumed that the oxidation behavior of the system will be the same with different working fluid in the turbine. Figure 29 b) shows the compact TGO thickness for Hydrogen turbine projected condition after 16000 h of exposure based on our experimental results for a TBC system provided by NETL as described in the next chapter.

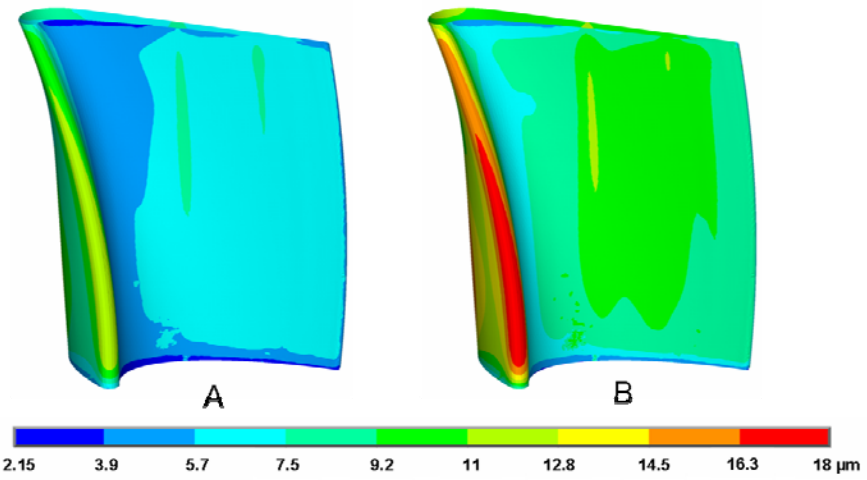

Figure 29. Compact TGO thickness for Hydrogen turbine projected conditions, 16000h:

a) published data [10], b) experimental results.

4.2.2 Internal TGO growth and modeling

Internally, the TGO grows from the TGO/BC interface towards the BC. This scale starts forming after a few hundred hours into exposure cycle, and has a "cauliflower-like" morphology when a cross section is examined. It has faster rate of growth than the compact layer and can be modeled by a similar equation:

$$h_{inward}(t,T) = A_n(T)\left(\frac{t}{t_0}\right)^m, \tag{39}$$

where $A_n(T)$ is temperature dependant rate constant in meters, m is time exponent found to be m=0.7 [26]. Using this approach and again implemented as a post-processor for the thermal solution one can obtain the expected TGO internal growth over the surface of the airfoil for different exposure to elevated temperature. Figure 30 shows the results from simulated hydrogen-fired turbine operating conditions at 16000h. Significant internal scale growth is expected at the leading edge and part of the suction side wall of the component. This growth is of course possible only if aluminum is still available in the bond coat. Perhaps this is a very good indicator to implement external cooling in those areas, everywhere else the scale formation is considerably lower.

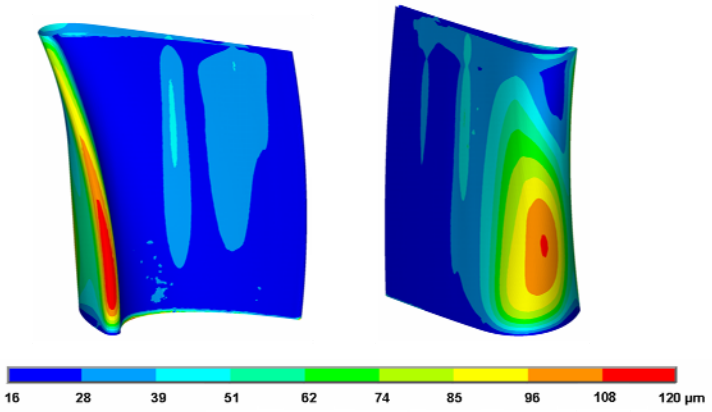

Figure 30. Inward TGO growth thickness for Hydrogen turbine projected conditions, 16000h.

4.2.3 β-Phase depletion and modeling

As the oxidation process continues and Al is being removed from the bond coat, a β-NiAl phase depleted zone is created with generally no more aluminum available to form a protective oxide. Indication for this is the dissolution of the Al rich β-phase. Aluminum form the bond coat can

also diffuse into the substrate and contributes to the total depletion of the bond coat. Observing and measuring the depleted zone thickness can provide data for the kinetics of the reaction. Echsler et al. fitted the curves of averaged values for the depleted zone thickness to equation:

$$h_{\beta-phase}(t,T) = B_n(T)\left(\frac{t}{t_0}\right)^p , \tag{40}$$

where $B_n(T)$ is temperature dependant depletion rate constant and p is the time exponent found to be between 0.6 and 0.85 for different system between 950 and 1100°C.

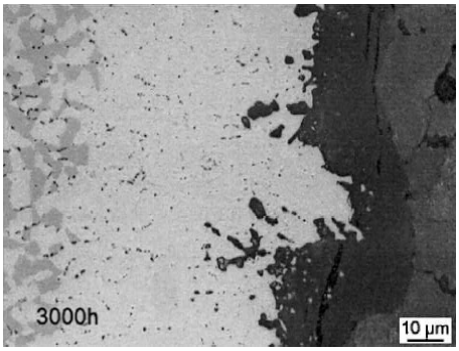

Figure 31. SEM of β phase depletion in 300µm APS YSZ system exposed to 1000°C for 3000h [10].

Based on the above kinetics, there is no obvious relation of how the compact layer and inward growth thickness would affect the reliability of the system. However, the depletion of the Al resource in the bond coat provides an opportunity to establish a damage state variable based on the TBC's ability to protect the underlying substrate from oxidation. Once the promotion of stable oxide phase is no longer active other more brittle oxides are formed and this should not happen within the useful time of the system. For this purpose we define a damage state variable over the surface of the airfoil that would indicate of how far this process has reached. Our new variable will again starts at zero for an "as processed" material, and attains value of one as the depleted zone reaches the bond coat thickness.

$$D_{coat} = \frac{h_{\beta-phase}}{h_{bond\ coat}}. \tag{41}$$

Implementing this approach, similarly to the ones for compact scale and inward growth, we can visualize the oxidation protection ability of the TBC system over the surface of the air foil as seen on figure 32.

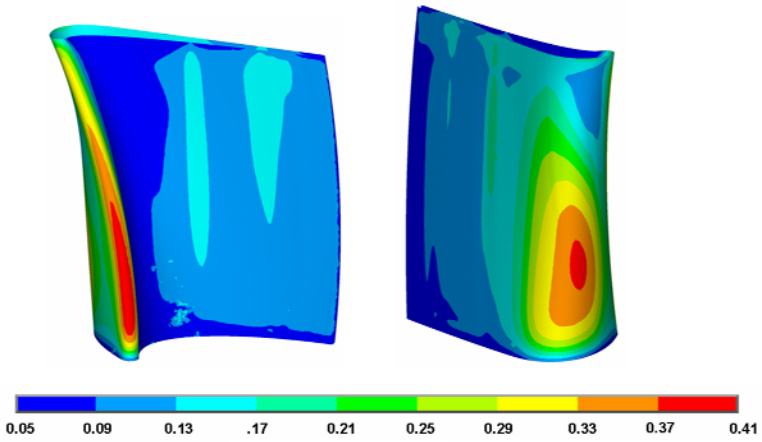

Figure 32. Normalized β phase Depletion for Hydrogen turbine projected conditions, 16000h, bond coat thickness is assumed at 200×10^{-6} m.

5.0 MATERIAL TESTING

In conjunction with model development, laboratory-scale experimental validation was executed to evaluate the influence of operational compressive stress levels on the performance of the TBC system. TBC coated single crystal coupons were exposed isothermally in air at 900, 1000, 1100^{o}C with and without compressive load. Exposed samples were cross-sectioned and evaluated with scanning electron microscope (SEM). Performance data was collected based on image analysis. Energy-dispersive x-ray (EDX) was employed to study the elemental distribution in TBC system after exposure. Nanoindentation was used to study the mechanical properties (Young's modulus and hardness) of the components in the TBC system and their evolution with temperature and time.

For this purpose NETL has provided 35 coupons with simple geometries (2.54 cm x 2.54 cm x 0.635 cm) made from representative nickel-based single-crystal René N5 matrices, coated with TBC systems (MCrAlY bond coat and 7% YSZ Air Plasma Sprayed (APS) top coat). Bond coat thickness is in the range of 150-200μm and top coat has thickness of 200-240μm.

Turbine airfoils have highly irregular geometries and under conditions found in service they are subjected to complex loadings. In most publications results are reported from either uniaxial isothermal tensile creep or thermal cyclic tests. The former usually providing data for the creep of the superalloy and the overhaul performance, and the later - on TBC spallation as a function of thermally-grown oxide (TGO) growth, surface roughness, temperature and thermal

mismatch between the layers. As both tests provide very valuable data there is little known to the effect of compressive stress on the performance of the superalloy / protective system.

5.1 HYPOTHESIS

A typical low pressure plasma sprayed MCrAlY bond coat for an APS YSZ TBC system has a high porosity and a highly irregular interface with the top coat, as seen in figure 36. It is hypothesized that a uniaxial in-plane stress will affect the rate of diffusion and densification in the bond coat and thus the rate of growth and cracking behavior of the thermally-grown oxide (TGO) layer. As a consequence, the time to coating failure will also be effected due to the altered rate of TGO growth and other microstructural changes being a direct consequence of applied stress.

To better understand the loading and failure mechanisms of the coating system under loading conditions, it will be equally important to characterize the evolution of the material's mechanical properties with temperature and exposure time, as it is expected that significant changes will be observed due to the microstructural and phase changes.

5.2 CONCEPT

The concept here is to place the sample in a slotted test fixture and both in laboratory furnace where they are exposed to elevated temperature without cycling. The difference in the coefficients of thermal expansion for the nickel superalloy substrate of the samples and for the

test fixture can be utilized to introduce thermally induced compressive stress in the samples. The fixture must be made of a material that can withstand the temperatures up to 1100ºC and has a coefficient of thermal expansion that is less than that of the samples. The choice was Silicon Carbide (SiC), in particular Hexoloy®SA by Saint-Gobain Advanced Ceramics. It has a maximum operating temperature of 1900°C, coefficient of thermal expansion of 4.02×10^{-6} mm/mmK, Young's modulus of 410 GPa, and Poisson ratio of 0.14. Saint-Gobain Ceramics produced three test fixtures by special order. Picture of the test fixture can be seen in figure 33. Test sample is "as processed" condition is shown on figure 34.

Figure 33. Test fixture (Hexoloy SA SiC by Saint-Gobain Ceramics)

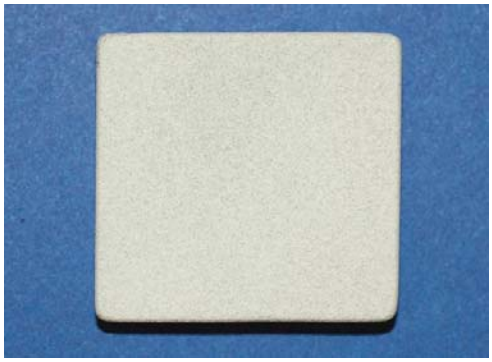

Figure 34. Test sample (ReneN5, MCrAlY, APS YSZ by NETL).

Prior to thermal exposure the coupons are initially subjected to non-destructive examination (NDE) techniques at West Virginia University (as a separate part of NETL program to evaluate the sample before exposure). The are subsequently subjected to uniaxial compressive stress at

elevated temperatures (i.e., 900-1100°C) for a maximum of 3,000 hours (as per test matrix provided in Table 5) in order to observe the effect on the TBC system.

Table 5. Test matrix

	900°C (1173K)		1000°C (1273K)		1100°C (1373K)	
	Stressed	unstressed	stressed	unstressed	stressed	unstressed
100 h						
300 h						
1000 h						
3000 h						

At all temperatures and running times, two samples were tested - one in the fixture's channel and one on the fixture's side top surface. The later one serves as a control in order to evaluate the role of the applied stress and strain in the sample.

The stress in the samples depends on the temperature, the effective cross sectional area of the fixture, and the clearance between the sides of the samples and the fixture. Both a basic one-dimensional analysis and three-dimensional finite element analysis of the thermal stress have been performed. The stress in the samples is highly sensitive to the aforementioned clearance. Therefore two sides of the samples were further modified to achieve the desired clearance value for each temperature. Table 6 lists the clearance required in order to achieve the stress levels desired at each testing temperature, as well as stress relaxation as a function of time.

Table 6. Clearances and stress level for different testing temperatures.

	900°C (1173K)	1000°C (1273K)	1100°C (1373K)
Clearance	0.007in (1.778×10^{-4}m)	0.008in (2.032×10^{-4}m)	0.009in (2.286×10^{-4}m)
Stress (initial)	235 MPa	245 MPa	250 MPa
Stress (1hour)	50 MPa	73 MPa	88 MPa

Figure 35 shows a contour plot of the expected initial third principal stress and total displacement for the case of exposure to 1000°C with clearance of 0.008in (2.032×10^{-4}m).

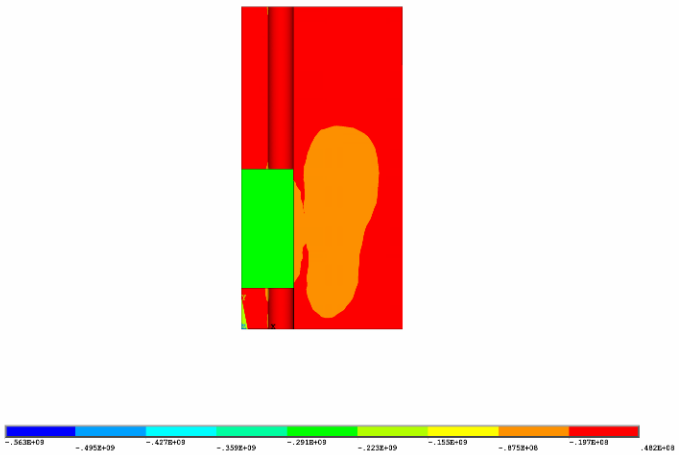

Figure 35. Third principal stress, MPa. Test fixture with sample @ 1273K.

The samples were placed in the test fixture and then together in laboratory bench furnace made by Carbolite, model CWF 13/13 capable of maintaining 1200^{o}C for extended periods of time, and maximum temperature of 1300^{o}C. After exposure to elevated temperature and stress all samples placed in test fixture exhibited a strong reaction between the SiC fixture and the Ni based René N5 quickly forming four interdiffusional layers. Removal of the samples was therefore impossible without damaging the side of the fixture. In order to prevent this unwanted reaction Alumina strips were utilized between the fixture and the sample. These strips were cut to size from rigid Alumina paper and subsequently compressed between two flat plates to achieve the almost final thickness. Based on this thickness, the sides of the samples were modified to accommodate the strips and maintain the required gap with the fixture. All tests were uninterrupted, non-cycled for the time length stated, except for the 1000 and 3000 hours test which ran simultaneously with the 1000 hour group in order to save time, thus they were thermally cycled once because of that and second time because of power outage.

5.3 SEM AND EDX EXAMINATION

After completing the test, samples were sent for NDT evaluation one more time and subsequently mounted in resin and cross-sectioned using standard metallographic preparation techniques. In order to avoid charging in the Scanning Electron Microscope (SEM), after polishing the sample is sputter coated with Palladium. Cross-sectioned samples are investigated using SEM Philips XL-30:

After exposure and cross sectioning all samples were subject to SEM examination including two unexposed samples dubbed as NETL#1 and NETL#2:

NETL# 1. One control sample in as processed condition which serves as reference point. Figure 36 shows SEM image of the top coat / bond coat / substrate system. The TGO scale is not present at this time;

NETL# 2. Sample which underwent ND testing - in order to evaluate destructiveness of this method when applied to our system. While examining the cross-section with the SEM, indents were difficult to identify, since surface roughness exceeds indentation depth. However, at regions earlier identified under the optical microscope containing indentations, no visible damage is found compared to regions where no indentations were performed, thus deeming the method non-destructive and safe to be used.

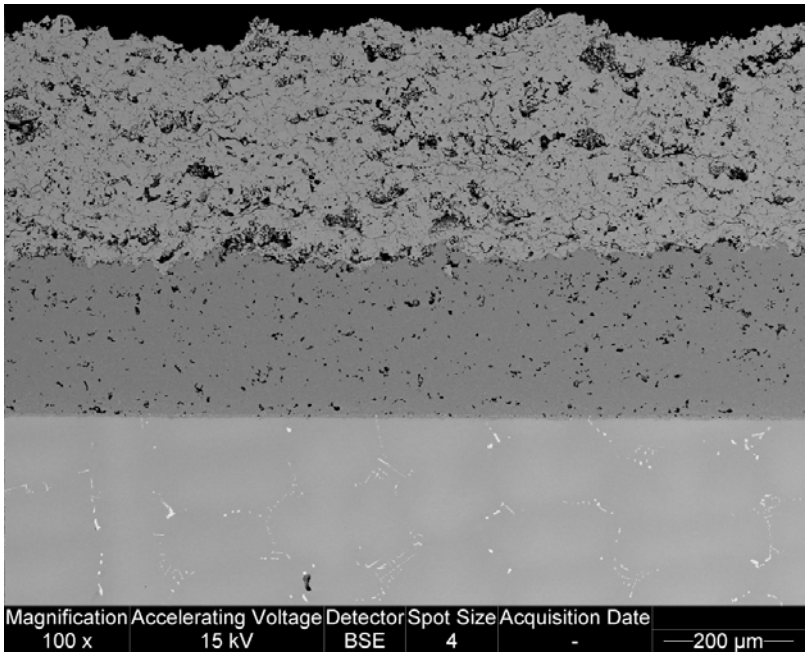

Figure 36. SEM Image of cross-sectioned sample prior to thermal exposure.

By using image analysis software on the SEM images several usually reported characteristics of the protective system were quantified as a function of exposure time and temperature:

- Nominal TGO thickness;
- Nominal YSZ thickness;
- Nominal bond coat thickness;
- Nominal interdiffusion layer thickness;
- Nominal coupon thickness.

When measuring the nominal thickness of the bond coat, we measured the length from the original bond coat / substrate interface to the bond coat / TGO interface after exposure. Compact TGO thickness was evaluated by measuring the length from the bond coat / scale interface to the oxide / YSZ interface in direction normal to the bond coat surface. This measurement was done in areas with well formed compact scale. These two measurements do not quantify neither the real amount of the oxide scale (both on the surface and internal) nor the amount of bond coat loss

due to oxidation around internal porosity. In order to assess the relation between the bond coat thickness, depletion, and the amount and quality of the resulting oxide scale we measured the mean vertical thickness of the bond coat and the oxide scale, including compact and internal. Mean vertical thickness is defined as the average thickness per unit length and is found from image analysis.

YSZ porosity was evaluated by point counting utilizing a grid of 16 point imposed over the image and counting the points falling over pores. This method has the advantage of being very quick and although the count needs to repeat many times it still obtains results much faster that area or line fraction techniques. Some of the relevant results are shown in the following discussion section.

5.4 INDENTATION TESTING

L. S. Cook et al. [34], measured the dynamic modulus and internal friction in low pressure plasma sprayed NiCrAlY bond coatings at different temperatures using a piezoelectric ultrasonic composite oscillator technique. They investigated coatings with different compositions: Ni-15.6Cr-5.2Al-0.20Y, Ni-17.2Cr-11.6Al-0.98Y, and Ni-33.0Cr-6.2Al-0.95Y. Reported values of Yong's modulus at room temperature were respectively: 205.0, 199.8, and 231.0 GPa. With increase of temperature the modulus in all compositions was found to reduce in a linear fashion to 137 (900^{o}C), 154.6 (900^{o}C), and 131.8 GPa (1000^{o}C) respectively. The authors concluded that, since the measured Young modulus for LPPS coatings at all temperatures was higher than the one for APS top coating (usually 20-60GPa) differences in the coating modulus would not account for TBC durability differences.

Franke et al. [35] investigated a single and two-phase platinum modified aluminade coating on nickel-based superalloy in as coated and after thermo-mechanical fatigue loading by SEM and nanoindentation. They followed the microstructural evolution in the β-NiAl grains as the PtAl2 phase dissolves and its influence on the associated mechanical properties. They found that both the Young's modulus and the hardness decreased after exposure. The change in the local mechanical properties was related to the microstructural and chemical changes in the coating. For their particular system they found a reduction of Young's modulus from 225 GPa to 150GPa and reduction of the hardness from 12 to 6 GPa. A strong influence of the Al concentration is also noted on the modulus of the NiAl phase, where a decrease of the Al content was found to lead to reduced modulus and increased hardness.

Li et al. [36] investigated the microstructural evolution of the NiCrAlY/CrON system after heat treatment. They measured the elastic modulus and residual stress of the coating system by nanoindentation and photo-stimulated luminescence spectrum methods. They concluded that the phase transformation $\beta \rightarrow \gamma' \rightarrow \gamma$ results in lower modulus for the heat treated sample, from 204.2GPa in annealed condition to 187.1 GPa at 100 hours exposure. Although this result coincides with the finding of Franke et al. [30] the reduction of the modulus for this particular system is not as great.

Measured values of the Young's modulus are influenced from both – the underlying crystal structure and the chemical composition of the coating. It should be expected that systems with different composition may have a dissimilar evolution of their mechanical properties. With respect to our testing program our goal is to obtain the evolution of the Young's modulus and hardness as a function of the exposure temperature and time, and operational level of stress in the substrate / protective layers system.

Mechanical properties of the substrate and coating layers of all exposed and two "as processed" samples were investigated by nanoindentation. Tribo Indenter by Hysitron was used in this investigation. It was fitted with 2D, three-plate capacitive force/displacement transducer and a three-faced pyramid Berkovich indenter. The Berkovich tip is the standard nanoindentation tip. It has a total included angle (angle from one edge to the opposite side) of 142.35 degrees. A typical radius of curvature for a standard Berkovich tip would be approximately 150nm.

Nanoindentation is used to determine two key material parameters - Young's modulus and hardness. With typical indentation depth between 100-300nm measured properties are local and several indents need to be performed to obtain an average value. Several calculations are performed based on the measured load-displacement curve [37]. A typical loading curves is shown of figure 37.

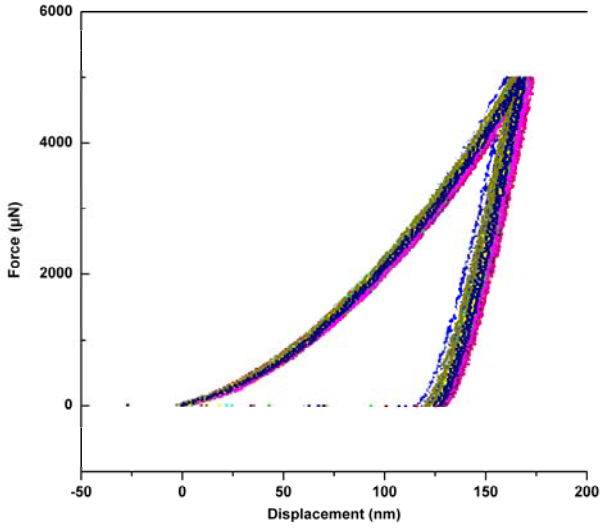

Figure 37. Typical load-displacement curves obtained by indenting with the same load within the substrate material.

Excluding both upper and lower ends, a select portion of the unload curve is used to fit the following power law:

$$P = A\left(h - h_f\right)^m \tag{42}$$

where P is the applied force, A is the contact area, and h is the indentation depth.

The first derivative of the force with respect of the indentation depth evaluated at the maximum force is the contact stiffness:

$$S = dP/dh\,. \tag{43}$$

The contact depth is calculated as:

$$h_c = h_{\max} - 0.75\frac{P_{\max}}{S} \tag{44}$$

where 0.75 is geometric constant to account for edge defects. From here the hardness is calculated as:

$$H = \frac{P_{\max}}{A(h_c)} \tag{45}$$

and the reduced modulus is:

$$E_r = \frac{\sqrt{\pi}}{2\sqrt{A\left(h_c\right)}}S\,. \tag{46}$$

The contact area is determined from the probe area function $A\left(h_c\right)$ where h_c is found by equation (44). This area function is experimentally obtained and accounts for imperfections and wear of the indentor tip. The obtained reduced modulus depends on both - the indentor and sample materials. The modulus of elasticity is related to the reduced modulus through the following equation:

$$\frac{1}{E_r} = \left(\frac{1-\nu^2}{E}\right)_{sample} + \left(\frac{1-\nu^2}{E}\right)_{indentor}\,. \tag{47}$$

Properties for standard diamond indentors are known and listed as:

- $E_{indentor} = 1140 GPa$
- $\nu_{indentor} = 0.07$.

In order to evaluate the modulus of all tested layers within the sample we need to assume a Poasson's ratio for every material. The representative values used in our calculations are:

- Substrate: $\nu = 0.3$
- Bond coat: $\nu = 0.3$
- YSZ: $\nu = 0.1$.

There are several mechanism by which the high temperature coatings degrade during service. These include oxidation, corrosion and interdiffusion with the underlying alloy substrate. Although MCrAlY coatings have good corrosion and oxidation resistance, after extended exposure to elevated temperature, element interdiffusion can greatly impart the stability of the coating and its ability to protect the substrate. During oxidation, aluminum from the bond coat diffuses to the coating interface with the YSZ to form a protective alumina scale. With continuous exposure this scale grows considerably and most prediction models link its thickness to the coating failure. This process continues until the aluminum concentration becomes insufficient to form a continuous protective scale. At this point less protective oxides of other elements (spinel) begin to form.

Elastic modulus is a key material parameter of interest and through nanoindentation we can asses its evolution with exposure time and temperature at different regions of the coating layers. Measurements were performed on already cross-sectioned and polished, exposed and "as processed" samples. Particular interest is placed on five regions: substrate bulk (SB), substrate interface diffusion zone with the bond coat (SI), bond coat bulk (BCB), bond coat interface

diffusion zone with the TGO (BCI), and the bulk of the top coat (TC). Figure 38 shows the measurements locations on a SEM image of the substrate / TBC system.

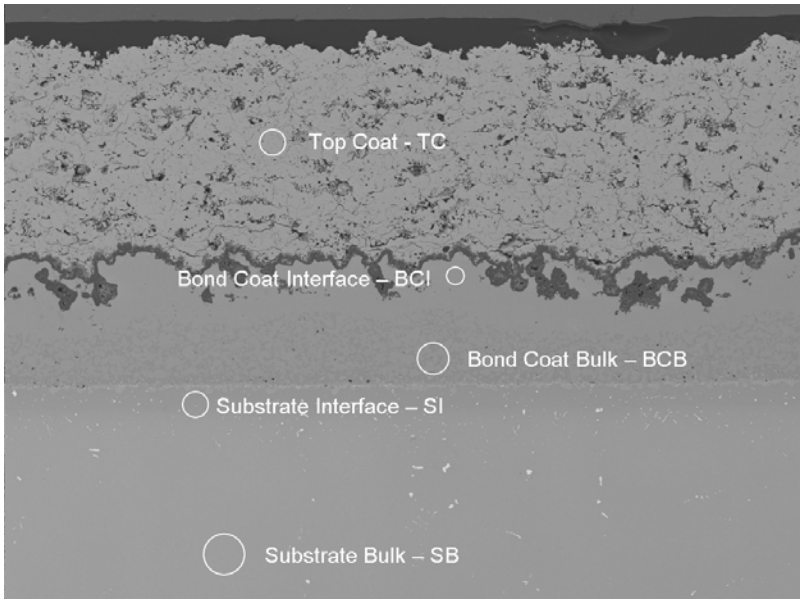

Figure 38. Indentation locations shown on SEM image of a sample exposed to 1100°C for 300 hours.

In order to determine the indentation load we initially performed indents with forces varying form 500μN to 7000μN at all locations. As reported in many publications, it was found that at small loads the indentation size effect played significant role and harness and modulus values were significantly higher. For indentation depth over 100nm both hardness and modulus become constant with a small deviation. Thus for indentations within the substrate and the bond coat we used a loading function 10 seconds load and unload, maximum force of 5000μN and no holding period. For indentations within the top coat we used a loading function 10 seconds load and unload, maximum force of 7000μN and no holding period. Indentations were performed in patterns of 4 x 3 indents, where the last two were removed to make the total of 10 indents in a pattern. By executing this kind of pattern we were able to correlate indentations results with an SEM image. For the bulk of the substrate and bond coat indentations were 10μm apart where in

the rest of the locations they were spaced at 5μm in order to fit the whole pattern in a smaller region. At each indentation location a minimum of three patterns per sample were executed to obtain an average value.

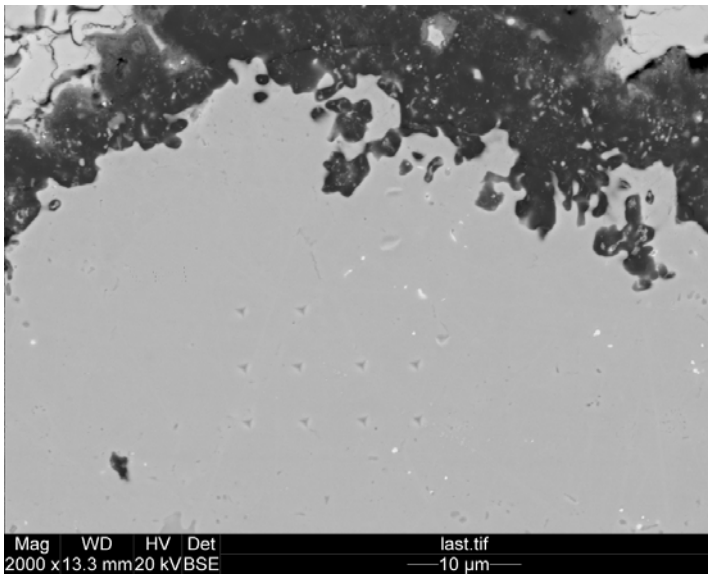

Figure 39. Indentation pattern - 10 indents, 5μm apart within the β-phase depleted zone of the bond coat (BCI).

5.5 RESULTS AND DISCUSSION

5.5.1 Exposure to 900°C

As per the test protocol in table 5, six samples in three pairs were exposed in air to 900°C for 100, 300, and 1000 hours respectively. Before and after the exposure they were tasted in a related study using non-destructive methods which were deemed to be unaffecting the samples in any significant way. Failure by loss of the protective coating did not occur in any of the 900°C samples. Figure 40 is composed of SEM images of cross sections of the above samples – A to F.

Several observations can be made:

- Bond coat / top coat interface is highly irregular shape and roughness. This is typical for APS top coat since it promotes better adhesion. As a consequence the oxide scale has the same irregular shape as oppose to the scale found in EBPVD top coats which shape can be approximated as a sine curve.
- The bond coat porosity is found to be progressively decreasing from A to F. The stressed 100h sample (B) had lower porosity compared to the unstressed (A). The same trend was observed at the higher temperatures. At the 300h stressed sample (D) porosity was almost non-existent except for pores with oxygen availability where oxide scale was formed.
- The APS YSZ has progressively densified from A to F sample, where the 1000h stressed sample (F) has lower porosity than the unstressed (E).
- With exposure to elevated temperature and oxygen the bond coat consistently forms a compact oxide scale which thickness is listed in table 12 as a function of time at constant temperature.
- Except for scale growth around existing pores there is very little internal oxidation.

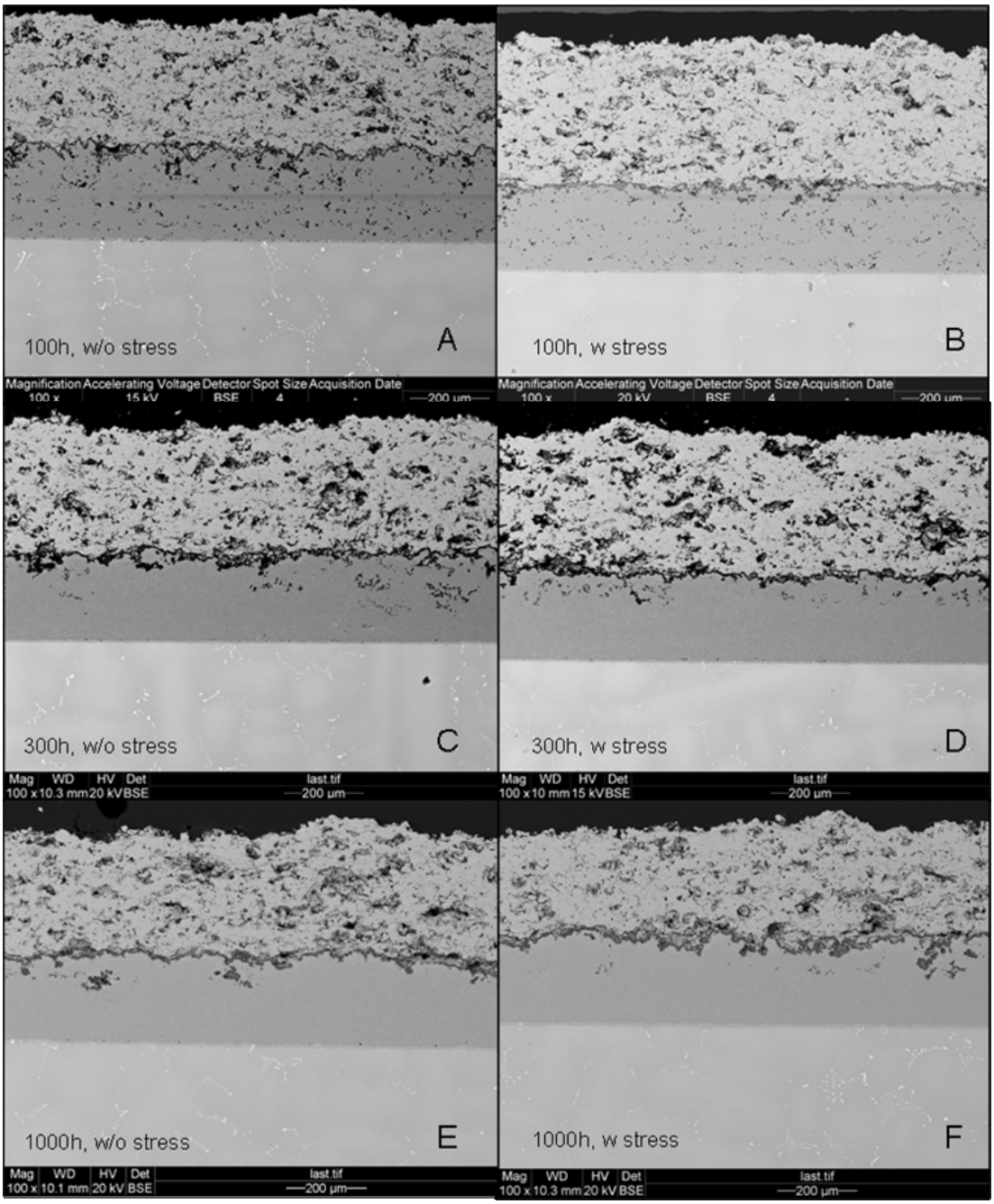

Figure 40. SEM images of cross section samples exposed to 900°C for 100, 300 and 1000 hours. Unstressed samples are shown at left column, stressed at the right.

- There is small interdiffusion zone between the bond coat and the substrate increasing with exposure time and temperature (in the following cases). At 900°C there is little or no influence from the applied stress on the thickness of this zone.

- At 100 and 300 hours exposure there were no cracks associated with the oxide scale. At 1000 hours, there are cracks found within the oxide scale propagating from / into imperfections on the interface between the scale and the top coat or splat boundaries. These cracks were local and did not propagate into the next undulation of the scale.
- Initially the bond coat is a two phase material consisting of the ordered intermetallic β-NiAl and the face centered cubic γ-Ni. In presence of oxygen and elevated temperature the β-NiAl is capable of forming a protective α-Al_2O_3 scale by diffusion of Al towards the interface with the oxygen permeable top coat. However, there is also an inward Al diffusion towards the Ni-based superalloy which can lead to a loss of Al to the superalloy

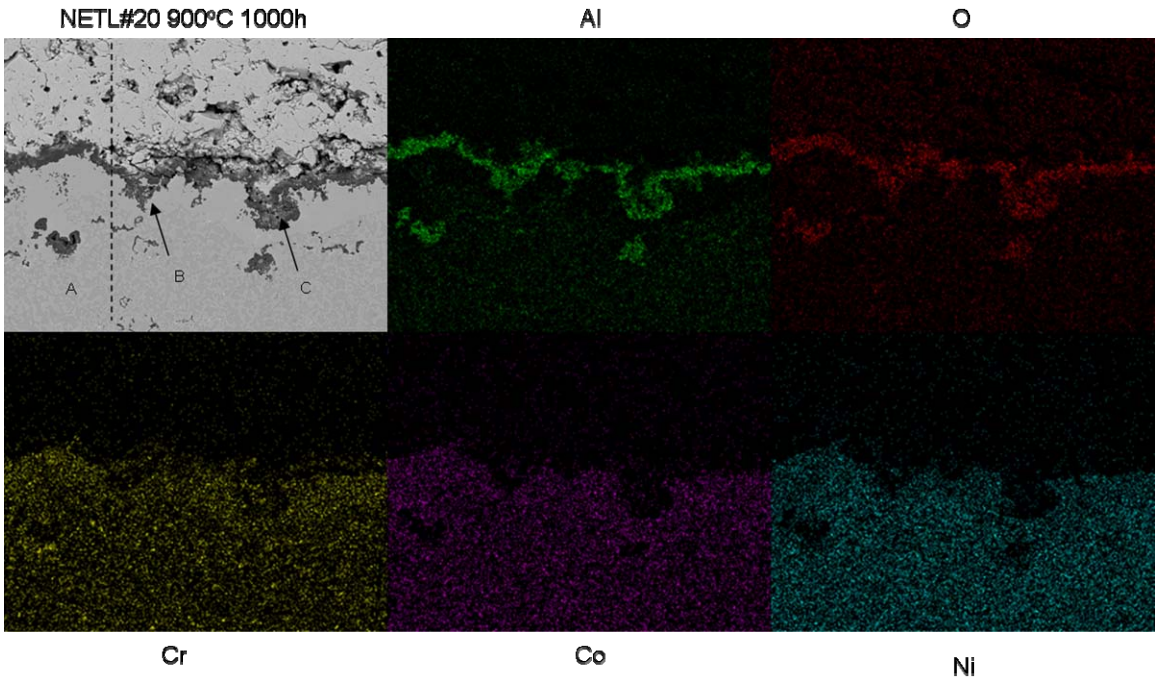

Figure 41. Spectrum mapping of bond coat / oxide scale, 900°C, 1000 hours

and promote unwanted topologically close packed (TCP) phase formation. In our 900oC exposed samples this TCP formation can in found as a thin uniform layer below the bond coat interface with the substrate. According to Gleeson et al. [38] and [39] a bond coat

with Al content over 10 at.% (4.8 wt.%) has the potential to form exclusively α-Al_2O_3 . In particular a Ni-Al alloy needs at least ~34 at.% Al in order to form an exclusive α-Al2O3 and only ~10 at.% Al if it has 6 at.% Cr. EDX analysis of our bond coat's β and γ phases revealed an Al content of ~(25 – 38) and ~(13-16) at.% respectively, where Cr was ~ (4 – 6) at.% in β- and ~(13-16) at.% in γ-phase. Taking into account the error of the EDX system (2-3%), we are still over the critical Al level in both the β- and γ-phase. Spectrum mapping of a bond coat/TGO/top coat region on 900°C /1000 h. sample, as seen in Figure 41 (region A), reveals the elemental distribution and exclusively Al and O in the TGO part of this segment. Further testing on points within the TGO showed a 100% α-Al_2O_3. Regions B and C show scales formed on the top of the alumina where some Cr inclusions are visible suggesting the presence of other oxides.

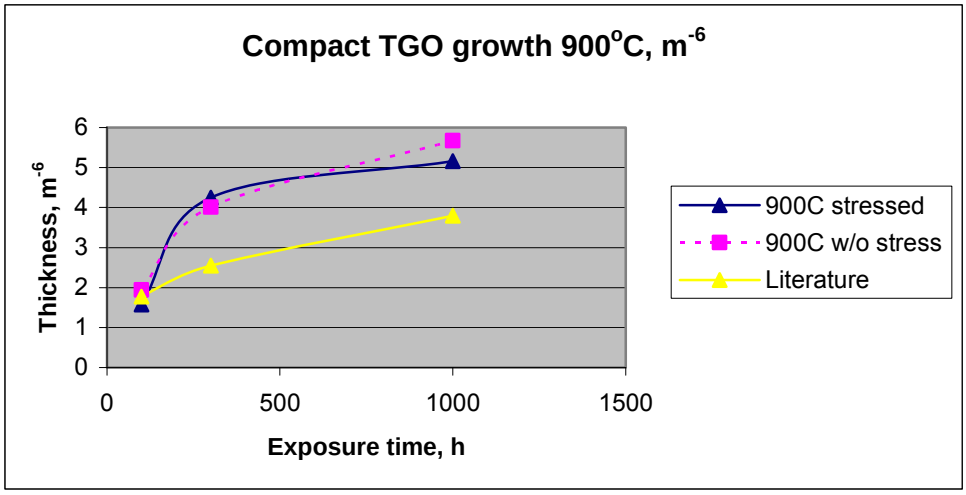

Figure 42. Compact TGO thickness at 900°C, measured and data from literature.

- After 100 hours exposure to 900°C both samples (stressed and non-stressed) achieved basically the same compact TGO thickness as seen in figure 42. After taking into account the deviation of the thickness results, the same is true for 300 and 1000

hours exposure. There is no evidence that the stress applied to the sample had any effect on the TGO thickness in all of the 900°C cases. The yellow line in figure 42 shows TGO thickness prediction based on published average data by Ecshler et al. [10] on APS YSZ / MCrAlY systems. Prediction and measurement from our system agree at 100 hours. However, in our specimens we find a more exponential growth in the next 200 hours where date from other systems indicates almost linear thickening. From 300 to 1000 hours the rate is the same between both systems. Therefore we can expect significantly different oxide scale thickness than the one modeled by the average data. If we assume that the activation energy in equation 38 is still the same, the best fit to our experimental data is found by changing the pre-exponent coefficient to 3.0x10-5.

So far, when measuring the nominal thickness of the bond coat, we measured the length from the original bond coat / substrate interface to the bond coat / TGO interface after exposure. Compact TGO thickness was evaluated by measuring the length from the bond coat / scale interface to the oxide / YSZ interface in direction normal to the bond coat surface. This measurement was done in areas with well formed compact scale. These two measurements do not quantify neither the real amount of the oxide scale (both on the surface and internal) nor the amount of bond coat loss due to oxidation around internal porosity. In order to assess the relation between the bond coat thickness, depletion, and the amount and quality of the resulting oxide scale we now measure the mean vertical thickness (MVT) of the bond coat and the oxide scale, including compact and internal. Mean vertical thickness is defined as the average thickness per unit length and is found from image analysis. For the case of 1000 hours exposure to 900°C the mean vertical scale thickness was found to be 16.03 and 15.98 μm for the stressed and non-stressed samples respectively. The mean vertical bond coat thickness was 200.07 and 203.26μm

respectively. These results illustrate the amount of internal oxidation not captures by the compact TGO thickness. In this particular case there is ~10 µm internal oxide scale compared to ~ 6 µm for the compact external growth showing significant amount of Al being lost internally. It also confirms that there is no significant difference between stressed and non-stressed samples as both samples had the same MVT of oxide scale and bond coat.

Material properties were evaluated by nanoindentation on all 900°C samples. The complete data set is listed in table 11. Plotted data for Young's modulus and Hardness in all measured regions as described in section 5.4 are in figure 43 and 44 respectively.

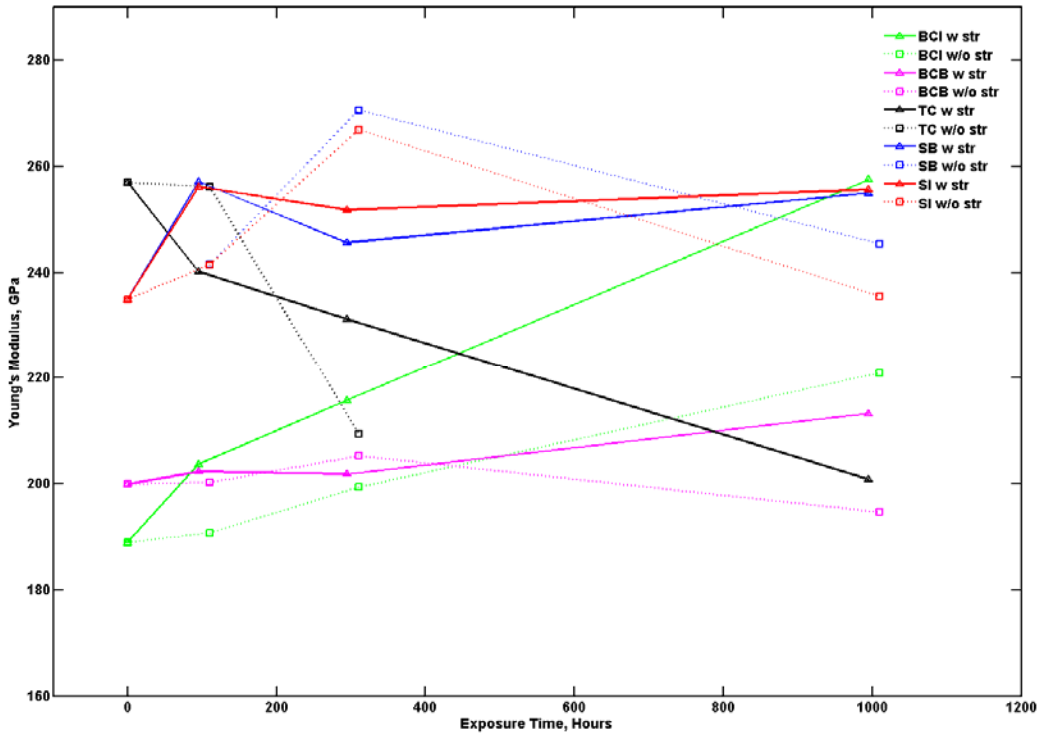

Figure 43. Young's modulus of substrate bulk (SB), substrate interface (SI), bond coat bulk (BCB), bond coat interface (BCI), and top coat bulk (TC) at 900°C, all samples.

During the preparation of our samples the controlled direction of the single crystal (substrate) was <001> through the sample's thickness. Subsequently the other directions were not

controlled. When the samples were cross sectioned we didn't know the exact orientation of the indentation surface with respect to the crystal lattice. Thus, as expected, the results for the Young's modulus from indentations in the substrate varied randomly between the samples from ~235 GPa to ~270 GPa. As the interdiffusion zone at 900^{o}C is very small values for the substrate interface were strongly influenced form the bulk lattice orientation. Measured values from the bond coat bulk have a large deviation which is to be expected because of the two phase composition of the coating. At 900^{o}C there is no significant evolution in the modulus with exposure time increase, however, a larger deviation is noticeable at 1000 hours as the relative amount of β- and γ-phase started to change. Measured values for the interface are the same with the bulk at 0 hours (for both substrate and bond coat) because there are no significant diffusion processes started. At 100 and 300 hours it is very difficult to evaluate the bond coat interface values as the γ-phase zone under the TGO is very small, thus values for BCB and BCI are essentially the same. At 1000 hours, where the γ-phase zone is easily identifiable under the optical microscope of the nanoindentor there is significant deviation of the modulus of BCI compared to the bulk especially for the stressed sample. This increase of the modulus can be attributed to the higher concentration of Cr and Co found in the γ-phase close to the interface (Ni-50, Al-14, Cr-18, Co-16 at.%) compared to those in the β-phase (Ni-49, Al-38, Cr-4, Co-8 at.%) and γ-phase (Ni-51, Al-16, Cr-15, Co-18 at.%) in the bulk of the coating. Measured modulus values from the bulk of top coat within one sample also showed a large deviation (+/- 10%) and significant drop in the modulus is observed with exposure time. Data from the one of the 1000h samples was not usable and therefore missing from the plot.

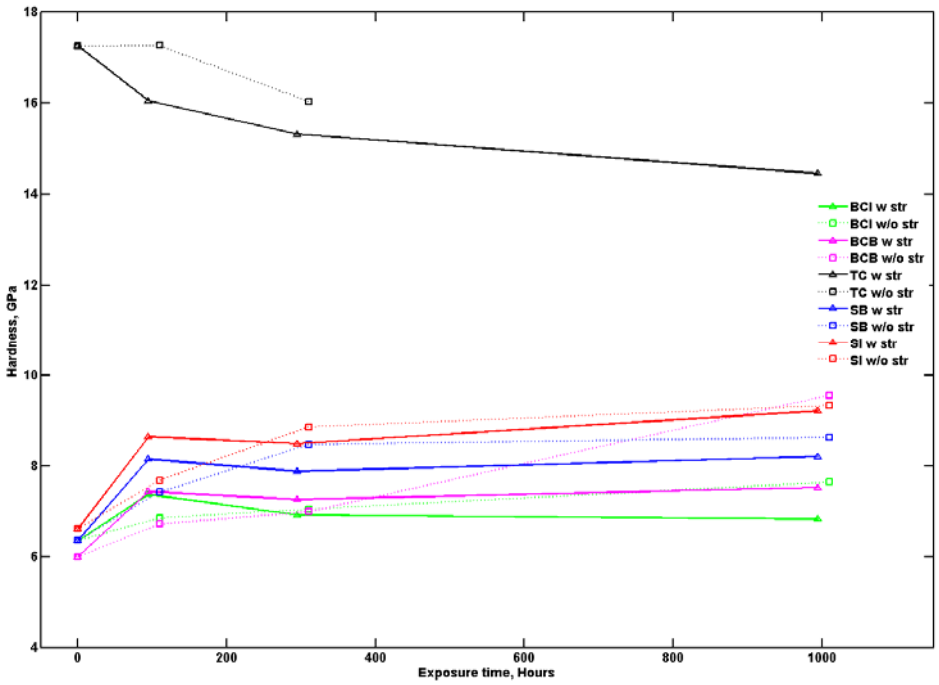

Figure 44. Hardness, GPa, of substrate bulk (SB), substrate interface (SI), bond coat bulk (BCB), bond coat interface (BCI), and top coat bulk (TC) at 900^{o}C, all samples.

There is general increase in the hardness in all locations except the YSZ, most significantly at the substrate interface. The bulk of the top coat, however, showed a significant decrease in the modulus from ~257GPa in as processed condition to ~200GPa after 1000 hours exposure in air to 900^{o}C.

5.5.2 Exposure to 1000°C

Two pairs of samples were exposed to 1000°C for 100 and 300 hours. There was no failure in all samples. These samples were fully investigated with SEM and nanoindentation. Currently two more pairs are being exposed to 1000 and 3000 hours. Since these tests are not competed at this time the 1000°C exposure will not be discussed in detail in this work. However, all measured data is found in tables 11 and 12. SEM images form the 100 and 300 hours samples are found in figure 45 and material property data is plotted in figures 46 and 47.

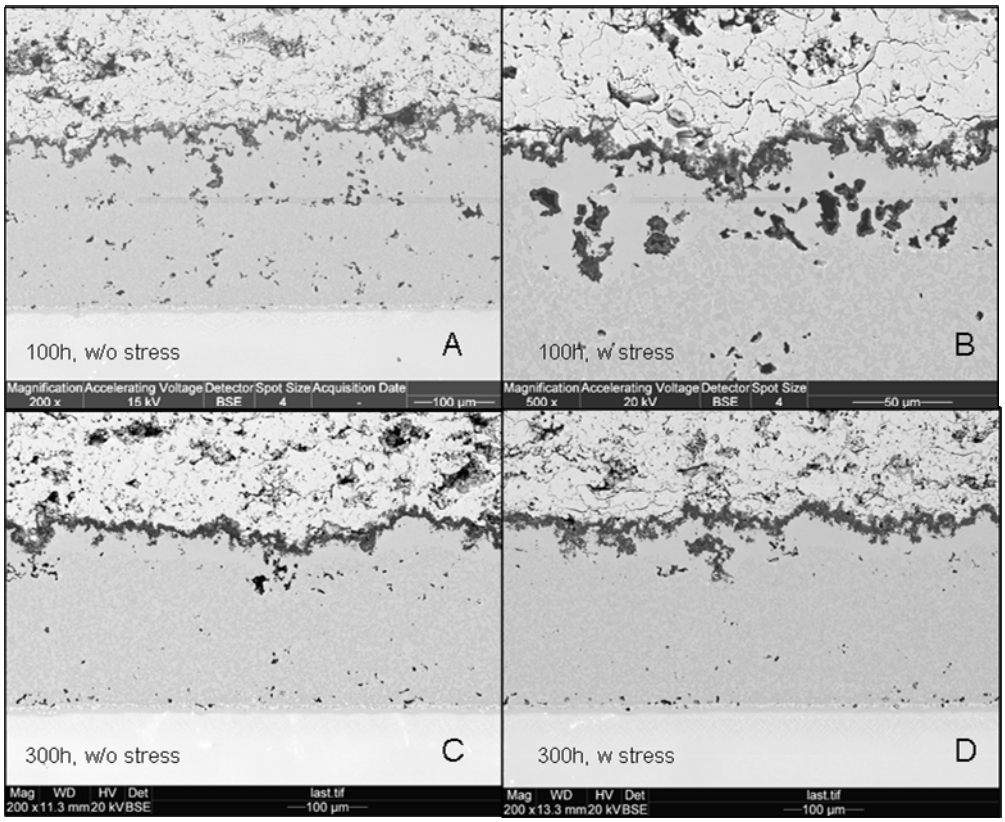

Figure 45. SEM images of cross section samples exposed to 1000°C for 100 and 300 hours. Unstressed samples are shown at left column, stressed at the right.

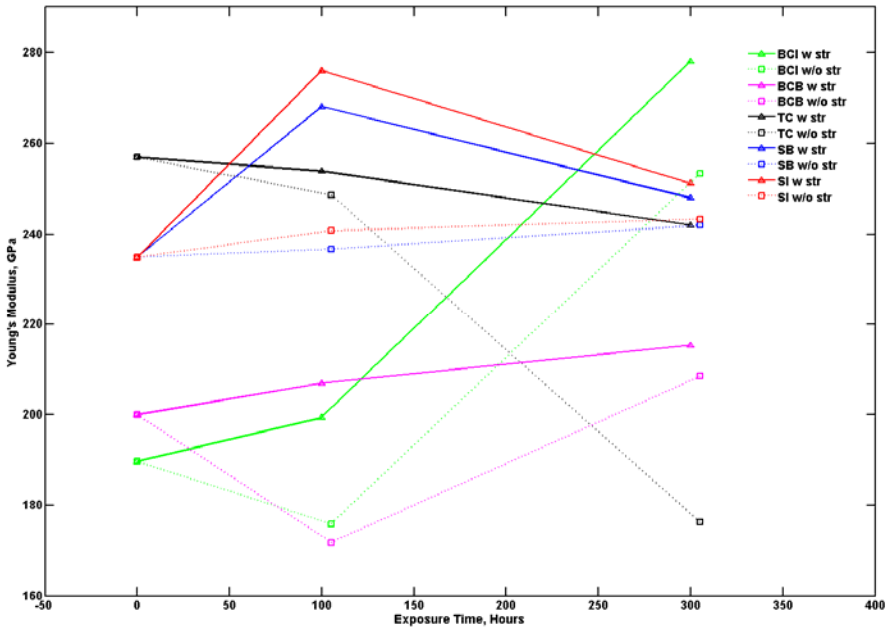

Figure 46. Young's modulus of substrate bulk (SB), substrate interface (SI), bond coat bulk (BCB), bond coat interface (BCI), and top coat bulk (TC) at 1000°C, all exposed samples.

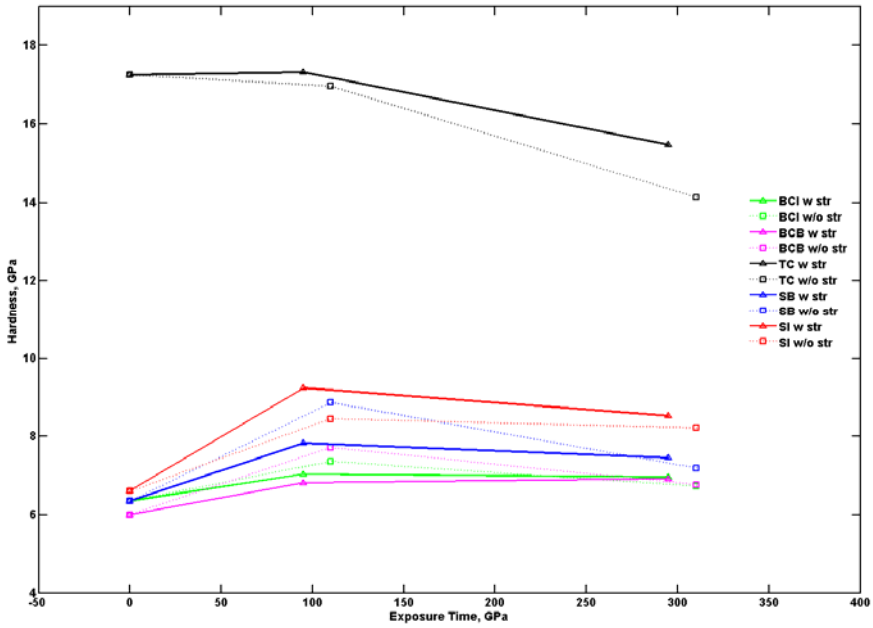

Figure 47. Hardness, GPa, of substrate bulk (SB), substrate interface (SI), bond coat bulk (BCB), bond coat interface (BCI), and top coat bulk (TC) at 1000°C, all exposed samples.

5.5.3 Exposure to 1100^{o}C

There were two pairs of samples exposed for 100 and 300 hours, and 6 samples in three pairs exposed to 600 hours. Figure 48 is composed of SEM images of the above samples. At 100 hours a compact oxide layer is visible, its thickness reaching 5.9 (+/- 1.91) μm in the stressed sample and 5.11 (+/- 1.66) μm in the unstressed one. There is an oxide scale formed around enclosed pores in the bond coat (with access to oxygen) and depleted β-phase surrounding them. Between 100 and 300 hours the compact oxide scale thickened as well as the internal oxide. Although being 8.6 – 9.1 μm thick there is no significant cracking in the scale. However, cracks are found (even at 100 hours) near or at existing imperfections on the bond coat / YSZ interface as seen in figure 48 B). Between 300 and 600 hours the internal oxidation developed more aggressively and the distinction of the compact scale became more difficult, and was measured only in the segments where it was well defined. The achieved thickness is plotted in fig. 49 along with data from literature [10]. There is again deviation between our experimental and the published data where it predicts 1.5 – 3.5 μm less then measured even at 100 hours. However, both the predicted and measured have approximately the same curvature and by modifying k_o to $4.0x10^{-5}$ in eq. 38 we can get a good fit to the experimental data. Thus now we can estimate the potential compact scale growth in the models shown in chapter 4 with respect to our current material capabilities. The compact scale was examined with EDX and was found to be 100% Al_2O_3 in the dark regions (on the SEM images) and ~95% Al_2O_3 and ~5% Y_2O_3 around some of the lighter spots within the TGO. Compact oxide scale growth does not show any dependence on the applied stress in the samples. However, porosity in the bong coat is being eliminated faster in the stressed samples, best seen in images C and D of fig. 48.

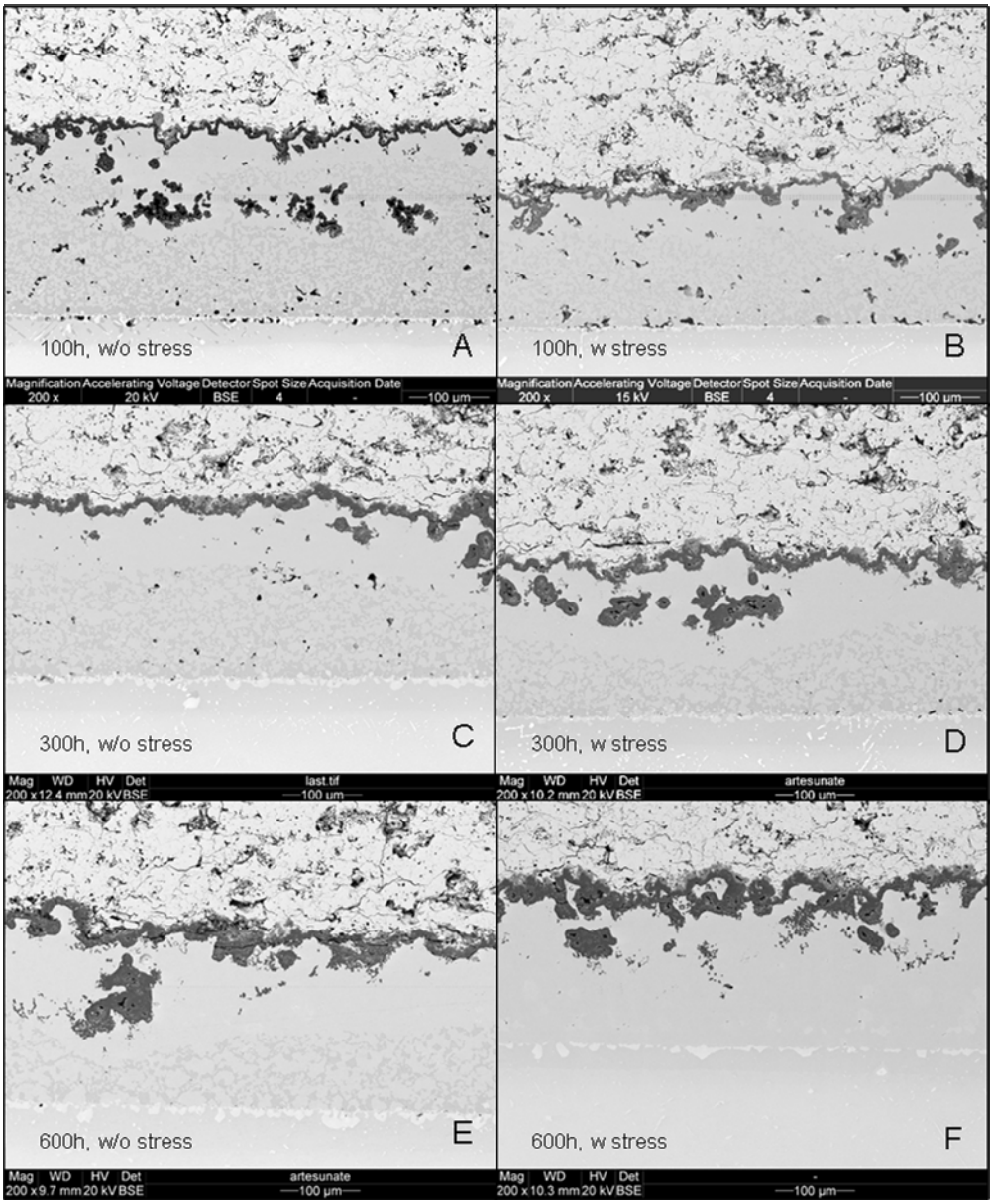

Figure 48. SEM images of cross section samples exposed to 1100°C for 100, 300 and 600 hours. Unstressed samples are shown at left column, stressed at the right.

Of all 600 hours exposed samples one failed after exposure and sitting on the desktop for 3 days. Failure occurred by crack propagation within the TGO scale. Propagation started from the edge of the sample and extended towards the middle. The top coat did not completely come off. This sample was not stressed during exposure. For the rest of the samples failure did not occur.

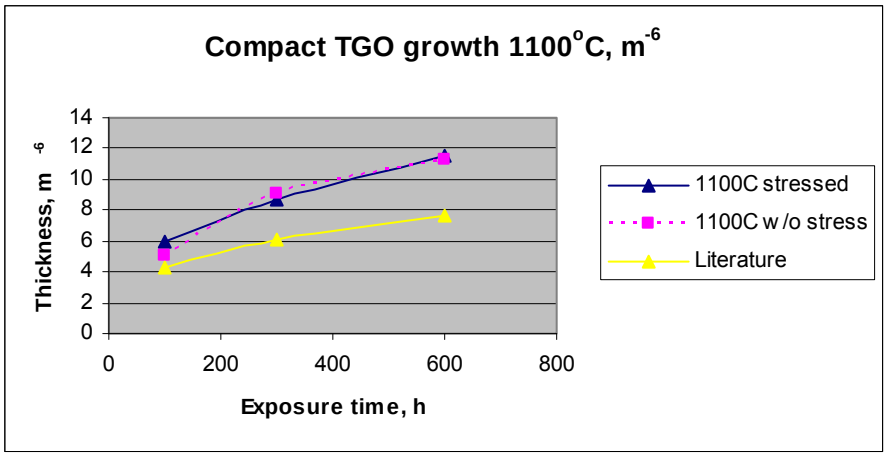

Figure 49. Compact TGO thickness at 1100°C, measured and data from literature.

However, in all of the 600 hours samples a severe cracking and coalescent cracks extending for more than 100µm can be seen at the samples' edges, as seen in figure 50.

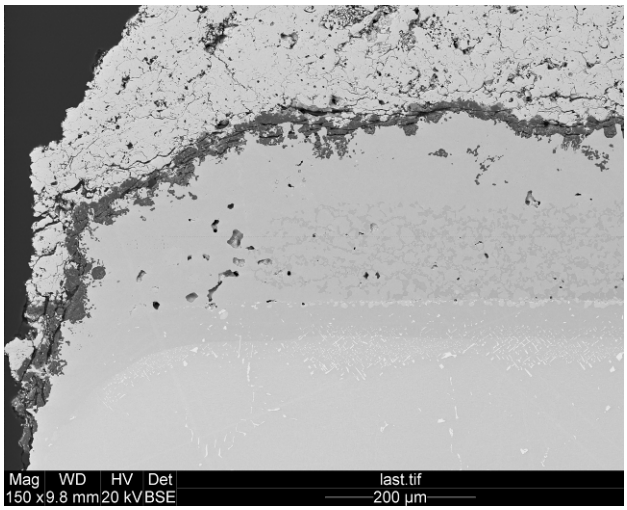

Figure 50. Coalescent cracks within the oxide scale at the edge of the sample at 600 hours, 1100°C.

Several observations can be made for the samples with 600 hours exposure:

- All samples featured vertical cracks within the YSZ either starting from the surface or embedded.

- All samples featured a significant oxide scale formation in the form of:

  - Compact TGO.

  - Internal growth around porosity with oxygen availability.

  - "Cauliflower" like internal growth.

  - Spinnel.

- Cracking within and around the TGO was observed in all samples.

- Cracking around and in the oxide scale can be characterized as:

  - Cracks contained within the scale.

  - Separation between the scale and the bond coat possibly propagating from / into the scale.

  - Separation between the scale and the top coat.

  - Cracks starting in the TGO and propagating within the YSZ possibly connecting with other neighboring cracks.

  - There could be more than two parallel cracks through the thickness of the scale.

While all samples featured cracks within the oxide scale, an important distinction can be made that oxide scales over well depleted β-NiAl phase zones of the bond coat (fig.48 F)) had fewer and smaller cracks than scales over less depleted zones (fig.48 E)). On other hand, β-phase depletion in the bond coat was uniform neither between the samples nor within the sample. No direct correlation could be made between the depletion and test conditions (induced stress in the sample). The following table summarizes these results.

Table 7. Summary of bond coat depletion behavior in all 1100°C, 600 hours exposed samples.

				Bond coat β-phase depletion		
				Full	Partial	Uniform
1100 C	100	str	3		x	x
	100		24		x	x
	300	str	16		x	x
	300		7		x	x
	600	str	15	x		x
	600		17		x	x
	600	str	8		x	x
	600		21	x	x	
	600	str	26	x	x	
	600		23	x	x	

There was one sample with uniformly and fully depleted bond coat, two with uniformly partially depleted bond coat and three samples featuring zones with full and zones with partial depletion. As explained earlier, in order to assess the relation between the bond coat thickness, depletion, and the amount and quality of the resulting oxide scale we now measure the mean vertical thickness (MVT) of the bond coat and the oxide scale, including compact and internal. MVT was evaluated for all 600h samples. Results are listed below, in table 8.

Table 8. Mean vertical thickness of the oxide scale and bond coat in all 1100°C, 600 hours exposed samples.

				Mean vertical thickness, µm		
				Scale	BC	BC not depl.
1100 C	600	str	15	42.43	173.25	0
	600		17	27.25	213.2	101.96
	600	str	8	28.15	191.22	101.72
	600		21	32.68	171.46	0
	600		21	27.53	212.42	112.09
	600	str	26	43.83	173.82	0
	600	str	26	31.1	210.25	120.4
	600		23	46.04	168.36	0
	600		23	34.66	194.72	60.33

It can be seen that the samples (and regions within the samples) with thinner bond coat (168.3-173.8µm) had formed thicker scale (32.68 – 46.04µm), but their bond coats were fully β-phase

depleted. The samples (or the regions within one sample) with thicker bond coats (191.2-213.2μm) had formed less scale (27.25-34.66μm), and featured a non-depleted β-phase zone.

Table 9 lists measurement for all 600h samples made in the "traditional" way. In all cases the thickness of the scale (from table 8) far exceeded the thickness of the compact scale because it includes the internal oxidation.

Table 9. Measured sample and coatings dimensions in all 1100°C, 600 hours exposed samples.

Exp. Hours	str	Sample #	Comp. TGO		Bond Coat		Depleted zone		Interdiffusion zone	
			μm	std. dev.	μm	std. dev.	μm	std. dev.	μm	std. dev.
600	str	15	12.84	6.96	196.28	11.26	196.28	11.26	110.73	16.36
600		17	13.1	4.57	233.4	14.7	121.45	23.1	145.22	11.3
600	str	8	10.39	1.63	210.12	13.52	108.16	11.74	91.63	17.56
600		21	10.71	1.48	210.7	15.28	108.98 – 210.7	23.61	95.9	16.46
600	str	26	11.25	3.65	199.21	13.73	134.35 - 199.21	14.4	86.81	15.43
600		23	10.04	2.26	188.44	25.97	52.21 – 188.44	8.88	90.2	11.36

As described above, regions with full bond coat depletion featured a more compact oxide scale containing less cracking and separation than those regions without full depletion. Several such regions were investigated with EDX spectral mapping to determine the elemental distribution within and around the scale. Two of these are discussed below.

- Fully depleted bond coat and compact scale:

Figure 51 shows a region with full depletion of the bond coat and thick but compact oxide scale formed on the bond coat / YSZ interface (dark grey areas), other oxides formed on the top of the compact scale (light grey areas) as well as some internal oxidation. From the spectrum mapping can be seen that the compact scale consists of aluminum and oxygen, which was confirmed by spot composition analysis to be Al_2O_3 and some Y_2O_3 (~5%). Traces form Cr, Ni and Co which other oxides can be seen on the top of the scale (or the light gray areas).

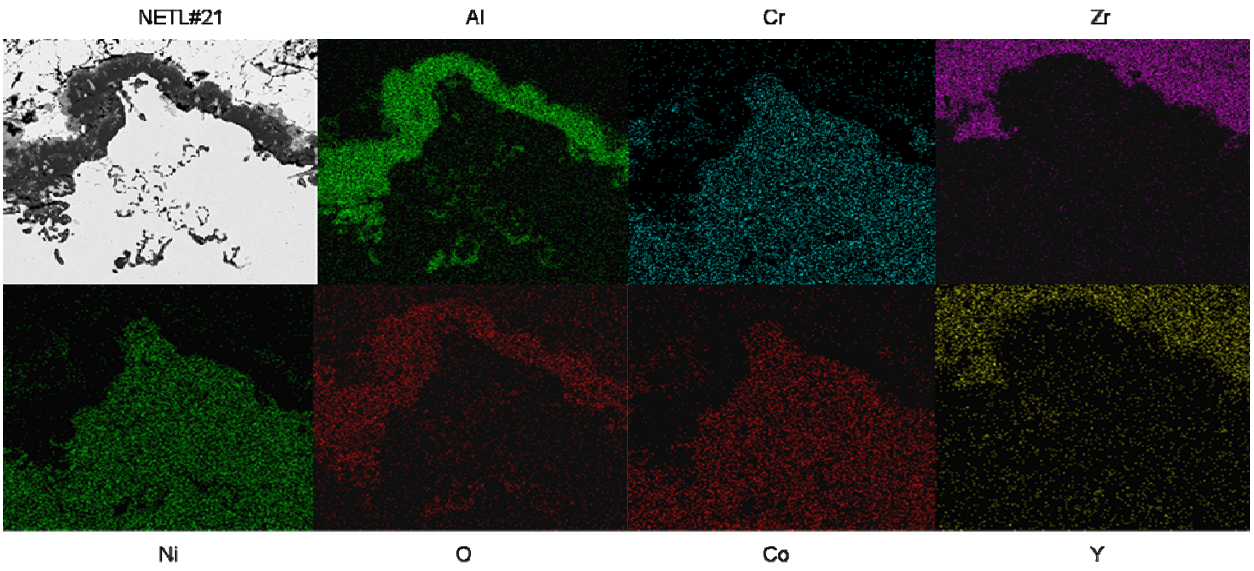

Figure 51. SEM image of the mapped area and spectrum maps - fully depleted bond coat.

- Not fully depleted bond coat and non-compact scale:

Figure 52 shows a region with not fully depleted bond coat within the same sample as above. Although the example is given for one sample the same is found true for samples that are

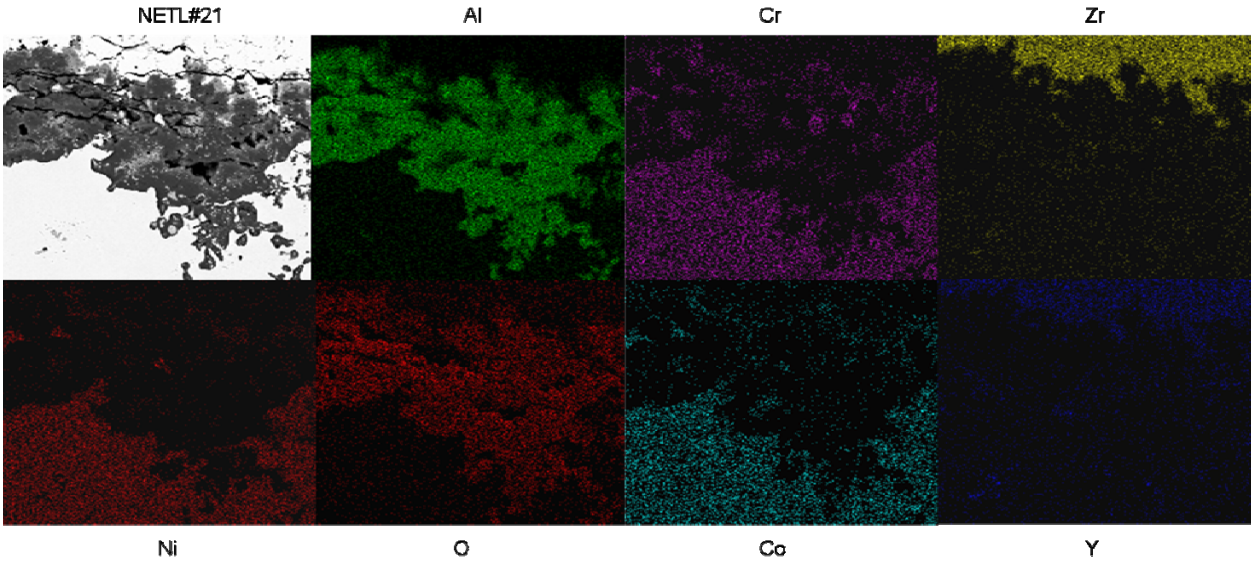

Figure 52. SEM image of the mapped area and spectrum maps - not fully depleted bond coat.

uniformly, fully or not fully, depleted. In this case a significant oxide growth can be seen on the bond coat interface with the YSZ. A compact scale cannot be distinguished because of severe

internal growth around pores that connected with the compact scale. The scale also features several parallel cracks. From the spectrum mapping can be seen that the scale consists predominantly of aluminum and oxygen, which was confirmed by spot composition analysis to be Al_2O_3 and some Y_2O_3. However, higher concentrations from Cr and Co are found embedded in the scale forming oxides other than alumina. Cr and Co oxides can also be found on the top of the scale (or the light gray areas). Chemical composition analysis at several positions of this sample is shown in table 10:

Table 10. Chemical composition sample #21, 1100°C, 600 hours. Abbreviations as described in fig.36.

location\element	Al at%	Cr at%	Co at%	Ni at%
BCB β-phase	36	6	8	49
BCB γ-phase	16	15	18	51
BCI	14	16	18	50
SI	16	15	17	51

As expected the β-phase in our NiCoCrAlY bond coat has Al content of 38 at%, where the γ-phase is down to 16 at% but has an increase in the Cr and Co. Moving closer to the interface with the oxide scale the aluminum content in the γ-phase drops with additional 2 at%. There is no significant difference in the content between the γ-phase found in the bulk and at the interdiffusion zone with the substrate. According to the ternary diagram for Ni-Cr-Co [39] at 1000°C as seen in figure 53, an alloy containing 6 at.%Cr would need at least ~10 at.%Al for exclusive Al_2O_3 scale growth (region III). In our sample's β-phase there is ~36at.% Al where in the γ-phase is ~16at.%. This Al concentration should be sufficient for exclusive Al_2O_3 growth even after the β-phase is fully depleted and only γ-phase is left in the bond coat. At higher temperatures, as in our case 1100°C, the amount Al required to promote formation of external scale should be lower. The compositional analysis was performed with an EDX system which has an error of 2-3%, but even at 3% error the Al concentration of the γ-phase (13at.%) would still be sufficient.

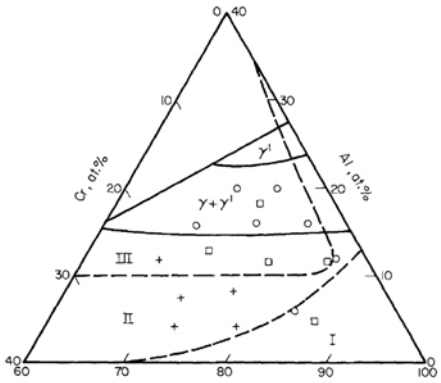

Figure 53. Oxide map of the ternary system Ni-Cr-Al at 1000°C [39]. Regions: I - NiO + internal Ox, II - Cr_2O_3 + internal Al_2O_3, III - Al_2O_3.

Young's Modulus and hardness were evaluated by nanoindentation on all 1100°C samples in all regions as described in section 5.4. Complete set of data is listed in table 11. Plotted data for Young's modulus and Hardness are in figure 54 and 55 respectively.

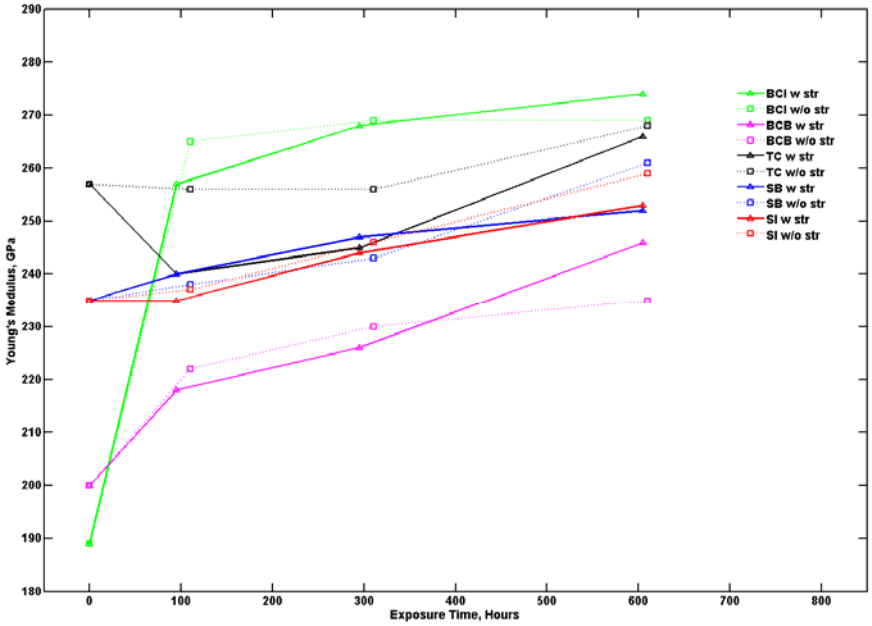

Figure 54. Young's modulus, GPa, of substrate bulk (SB), substrate interface (SI), bond coat bulk (BCB), bond coat interface (BCI), and top coat bulk (TC) at 1100°C, all samples.

Measured values for the Young's modulus of the substrate bulk (SB) and substrate interface (SI) showed good correlation with each other confirming the observed at 900°C dependence. There

was a steady increase in the modulus from ~235 GPa in " as processed" condition to ~ (253-261) GPa at 600 hours. There is no significant difference between the stressed and non-stressed samples.

The modulus of BCB and BCI in "as processed" are essentially the same because of the large deviation in the measured values - 199.8 (+/- 15.1) and 189.6 (+/- 19.6) respectively, which is expected for the two phase coating. After 100 hours exposure a significant increase (~65 GPa) is measured in the modulus of the interface region, where the β-phase is depleted and the γ-phase is predominant. The deviation in the modulus in BCI is now lower than in the BCB. The bulk of the bond coat has an increase of ~20 GPa - much lower than the interface. From 100 to 600 hours both the BCB and BCI show a steady increase in modulus with approximately the same slope, achieving an average of ~240 and ~272 GPa at 600 hours respectively. This result is significantly different from reported data in [35] on platinum modified aluminade coating and [36] on NiCrAlY/CrON system, where for their particular systems both authors found a decrease in the modulus by 75 and 17 GPa respectively as the β → γ-phase transformation occur. Measured values of the Young's modulus are influenced from both – the underlying crystal structure and the chemical composition of the coating. As expected, systems with different composition have dissimilar evolution of their mechanical properties. However, in our case the modulus increase cannot be simply explained by the β → γ-phase transformation. Obviously if this was the case we would have measured a lower modulus. Since we find this material behavior consistently at all temperatures and showing dependence of both temperature and exposure time, we are confident that the measurements are correct. At this point we can hypothesize that perhaps an internal formation of harder oxides in this area or higher yttria inclusion concentration is responsible for the change in the elastic material behavior. However,

in order to explain this particular modulus increase and to further characterize the material phase composition close to the oxide scale interface a transmission electron microscope (TEM) study would be appropriate.

The modulus of the top coat (bulk) of the non-stressed samples had a steady behavior to 300 hours and then showed an increase to 600 hours by approximately 17 GPa. The stressed samples showed initial decrease in modulus in 100 and 300 hours but no difference at 600hours where it achieved the same value as the non-stressed samples. It is important to note that while the bulk of the YSZ has local modulus of ~250 GPa initially the modulus of the top coat as a whole is much lower - ~50 GPa.

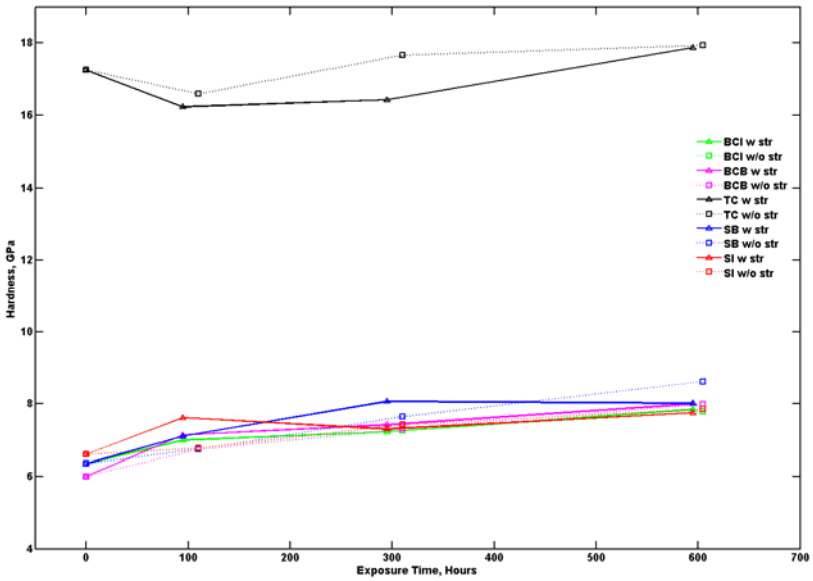

Figure 55. Hardness, GPa, of substrate bulk (SB), substrate interface (SI), bond coat bulk (BCB), bond coat interface (BCI), and top coat bulk (TC) at 1100°C, all samples.

Hardness data for 1100°C exposed samples is plotted in figure 55. The hardness values for all points of interest in the substrate and the bond coat are very close, most of them within the

standard deviation. As seen at 900°C, at 1100°C there is a general increase (~1.65 GPa) in the harness and a linear dependence of the hardness with time is found. At 1100°C the deviation in values is smaller than this at 900°C. The increase in hardness and lower deviation could be linked to the densification of the initially porous coating. YSZ's hardness had a drop at 100 hours exposure and recovered to achieve the same value at 600 hours for both stressed / non-stressed samples, increased by approximately 0.65GPa. Dependence on the test conditions (stress) was not found in the hardness measurements at 1100°C.

The above results show no dependence of the material property evolution on the stress imposed on the sample, thus indicating that test results obtained in non-loaded samples can be well correlated to actual working components.

Such knowledge of the local materials properties and their evolution with exposure time and temperature can be used to create better models of the coating systems and thus gain knowledge of its actual loading and performance, to the ultimate goal of component life prediction. Current commercial finite element software packages as ANSYS, facilitate a change in the loading from time step to the next. However, they do not offer the ability to change the materials properties with time thus presenting a challenge in the modeling of materials working in high temperature environments and exhibiting evolution in their properties. One possibility is a creation of specific material models well approximating the actual material behavior that can be implemented as user defined materials within those commercial packages.

Table 11. Material properties evaluated by nanoindentation, all samples.

	Exp. Hours	str	Sample #	Substrate Bulk				Substrate Interface				Bond Coat Bulk				Bond Coat Interface				APS YSZ			
				E, Gpa	std. dev.	H, Gpa	std. dev.	E, Gpa	std. dev.	H, Gpa	std. dev.	E, Gpa	std. dev.	H, Gpa	std. dev.	E, Gpa	std. dev.	H, Gpa	std. dev.	E, Gpa	std. dev.	H, Gpa	std. dev.
900 C	100	str	12	257.2	6.06	8.15	0.32	256.19	10.86	8.64	0.38	202.35	19.49	7.43	0.56	203.71	23.27	7.37	0.68	240.22	22.59	16.04	2.71
	100		11	241.53	9.55	7.42	0.34	241.49	6.63	7.68	0.3	200.29	14.62	6.72	0.55	190.75	19.33	6.85	0.45	256.2	22	17.26	1.25
	300	str	9	245.68	9.06	7.88	0.35	251.86	8.96	8.49	0.19	201.86	19.78	7.26	0.62	215.83	26.85	6.92	0.48	231.24	24.09	15.31	2.59
	300		14	270.62	9.41	8.47	0.32	266.98	10.62	8.85	0.45	205.32	20.03	6.99	0.52	199.41	29.7	7.04	0.44	209.5	15.96	16.03	1.59
	1000	str	13	255.04	9.28	8.2	0.31	255.7	12.71	9.21	0.78	213.31	25.71	7.52	0.77	257.61	16.44	6.83	0.26	200.88	20.59	14.45	1.43
	1000		20	245.46	9.83	8.62	0.44	235.6	11.26	9.33	0.66	194.7	11.86	9.55	0.96	220.97	22.58	7.64	0.41	-	-	-	-
	3000	str																					
	3000																						
1000 C	100	str	4	268.14	10.31	7.83	0.32	276.08	10.18	9.24	0.63	207	25.34	6.82	0.33	199.41	29.7	7.04	0.44	253.95	23.82	17.32	2.01
	100		5	236.76	8.07	8.87	0.39	240.8	40.51	8.45	0.69	171.78	17.75	7.72	0.49	175.9	24.22	7.36	0.56	248.65	29.52	16.96	1.16
	300	str	10	248.8	9.87	7.46	0.21	251.24	8.7	8.53	0.6	215.39	30.39	6.92	0.39	278.15	19.9	6.96	0.46	242.08	33.46	15.47	3.05
	300		6	242.01	8.63	7.19	0.16	243.37	7.14	8.22	0.8	208.5	30.88	6.77	0.38	253.4	22.88	6.73	0.3	176.26	27.61	14.13	2.06
	1000	str																					
	1000																						
	3000	str																					
	3000																						
1100 C	100	str	3	239.92	9.59	7.11	0.23	235.72	7.27	7.62	0.27	218.02	27.96	7.14	0.38	257.08	19.54	7	0.66	239.58	31.76	16.23	1.98
	100		24	238.33	9.84	6.75	0.23	237.67	7.09	6.78	0.19	222.34	35.36	6.74	0.34	265.07	9.73	6.76	0.24	256.6	26.8	16.59	2.24
	300	str	16	247.05	10.95	8.07	0.45	244.83	6.72	7.3	0.28	226.3	35.31	7.42	0.54	268.42	13.23	7.23	0.31	245.24	27.54	16.43	1.46
	300		7	243.99	6.81	7.64	0.33	246.18	8.15	7.42	0.27	230.31	37.25	7.31	0.49	269.71	11.79	7.26	0.27	256.68	29.85	17.66	1.61
	600	str	ave	252.28	13.43	8.02	0.53	253.68	9.01	7.745	0.29	246.76	27.85	8	0.44	274.39	10.27	7.85	0.35	266.41	20.13	17.87	1.49
	600		ave	261.3	18.6	8.62	0.65	259.41	17.25	7.85	0.28	235.91	32.93	7.98	0.36	269.73	13.65	7.78	0.34	268.23	25.1	17.93	1.49
	0		1	235.42	5.96	6.35	0.2	235.46	8.39	6.61	0.42	199.83	15.12	6	0.49	189.64	19.6	6.35	0.8	257.62	19.16	17.24	1.21

Table 12. Nominal dimensions of TBC system components and substrate after exposure, all samples.

	Exp. Hours	str	Sample #	Comp. TGO		Bond Coat		Depleted zone		Interdiffusion zone		YSZ		Substrate		Sample thickness		YSZ porosity
				µm	std. dev.	µm	std. dev.	µm	std. dev.	µm	std. dev.	µm	std. dev.	µm	std. dev.	µm	std. dev.	%
900 C	100	str	12	1.57	0.38	209.98	9.65			12.73	1.13	353.9	16.18			3649.3	13.08	17.5
	100		11	1.94	0.51	229.94	10.63			10.03	2.55	311.81	19.48			3615.23	16.56	16.46
	300	str	9	4.25	1.25	214.06	7.2	9.4	5.36	13.27	1.25	349.9	13.2	3104.8	3.47	3679.29	14.21	18.44
	300		14	4.01	1.35	215.13	11.34	16.4	6.76	15.11	0.66	316.8	16.73	3099.3	18.53	3638.93	18.03	21.25
	1000	str	13	5.16	1	197.33	21.96	33.4	10.63	21.13	0.89	290.16	29.83	3090.33	6.56	3595.95	22.94	
	1000		20	5.67	1.5	210.72	4.88	20	5.19	20.42	2.77	312.7	19.66	3012.54	13.39	3559.8	28.52	
	3000	str																
	3000																	
1000 C	100	str	4	4.03	1.16	190.97	13.4			20.86	2.81	296.49	14.06			3597.55	25.91	15.21
	100		5	3.89	1.21	212.78	15.28			15.88	2.43	349.97	25.09			3607.24	23.53	15.42
	300	str	10	9.89	3.91	221.57	8.54	35.82	7.78	43.86	7.48	328.41	13.71	3082.99	15.99	3624.12	23.38	14.58
	300		6	7.14	2.55	211.24	13.49	33.29	4.8	36.87	3.9	307.31	13.55	3111.5	14.07	3672.75	22.97	17.9
	1000	str																
	1000																	
	3000	str																
	3000																	
1100 C	100	str	3	5.9	1.91	181.91	15.39			47.4	3.97	334.15	14.7			3581.65	22.7	14.8
	100		24	5.11	1.66	230.04	10.17			30.6	3.55	346.04	11.28			3637.66	25.76	15.63
	300	str	16	8.67	2.47	190.4	11.2	93.94	14.7	74.64	9.19	326.63	11.92	3096.1	11.53	3603.43	19.1	16.45
	300		7	9.1	2.38	211.21	6.77	84.07	13.18	62.75	6.59	325.03	19.6	3082.04	5.14	3622.5	20.25	15.83
	600	str	15	12.84	6.96	196.28	11.26	196.28	11.26	110.73	16.36	382.79	18.3	3065.76	11.28	3646.57	25.3	17.7
	600		17	13.1	4.57	233.4	14.7	121.45	23.1	145.22	11.3	365.7	13.8	3153.23	17.22	3745.8	34	16.25
	600	str	8	10.39	1.63	210.12	13.52	108.16	11.74	91.63	17.56	356.01	14.81	3112.46	26.83	3679.13	41.77	
	600		21	10.71	1.48	210.7	15.28	108.98 *	23.61	95.9	16.46	328.79	29.26	3069.69	6.3	3610.42	26.02	
	600	str	26	11.25	3.65	199.21	13.73	134.35 *	14.4	86.81	15.43	294.33	12.68	3100.35	3.96	3614.05	14.6	
	600		23	10.04	2.26	188.44	25.97	52.21 to full	8.88	90.2	11.36	356.03	18.02	3068.36	13.12	3669.79	26.31	

6.0 CONCLUSIONS

6.1 MODELING

In the presented work we took a first look at some of the challenges the coal based advanced turbine systems present for the turbine designers and material scientists. In a related study by Mazzotta et al. [6], computational fluid analysis was performed for both hydrogen fired and oxy-fuel systems using real airfoil geometry (NASA E^3).

6.1.1 Thermal solutions

Based on the results from [6] we obtained three-dimensional thermal solutions for hydrogen-fired and oxy-fuel turbines and determined the following:

- For the hydrogen fired turbine there will be a maximum substrate temperature of about 900^{o}C based on the assumed thermal properties of the TBC system (table 3), an internal cooling (800K, 3000W/m2K), and no external film cooling.
- The dynamic nature of both the micro-structure and phase composition of the top coat were considered. An increase in YSZ thermal conductivity from 0.9 to 2.4 W/m^{2}K was found to result in 100^{o}C increase in the maximum substrate temperature for the hydrogen

- For the oxy-fuel turbine concept, the maximum temperature on the YSZ surface will be about 1600^{o}C, which is ~300^{o}C higher than the allowed 1300^{o}C for state-of-the-art low-density, high purity APS YSZ coatings. A combination of two possible solutions were considered:
    - An additional low-conductivity overlay coating. It was determined that the overlay coating could not, by itself, reduce the thermal load to an acceptable level.
    - The introduction of extensive external film cooling on the airfoil surface. It was shown that film cooling could, by itself, reduce the thermal load to an acceptable level. However, one needs to consider the turbine losses associated with the cooling. We calculated the minimum cooling effectiveness needed to maintain sustainable thermal load on the top coat and subsequently on the rest of the system. Under this assumption we found maximum substrate temperature of 953^{o}C for the oxy-fuel turbine.
- Surface maps were created showing the development of the oxide scale and β-NiAl depletion of the bond coat as a function of substrate temperature and thermal properties of the bond coat. Based on our experimental results we found a maximum scale thickness of 18μm for the hydrogen turbine after 16000 hours, compared with ~12μm based on published results.

6.1.2 Structural, creep and fatigue modeling

Damage mechanics based creep and fatigue models were used to model the substrate material damage behavior of the airfoils in advanced turbine systems at elevated temperatures. Both models used a scalar damage parameter and allowed for interaction if required.

- We introduced a formulation for damage equivalent stress for material with cubic symmetry in order to perform three-dimensional analysis and related the multi-axial state of stress in the component to the one-dimensional stress in the damage mechanics formulation and experimental data.
- Creep and fatigue models were implemented as a user-modified creep routine in the commercial FEA package ANSYS. This routine can be used in combination with different plastic or elastic material models. It is called at every time step and calculates and reports both creep and fatigue damage evolution.
- This routine was used to visualize the creep and fatigue damage evolution over airfoils for hydrogen-fired and oxy-fuel turbines concepts. We found substantial localized creep damage for the hydrogen-fired turbine at 16000 hours and at 800 hours for the oxy-fuel turbine system. In both cases, the highest damage occurred in regions of high stress near the root of the airfoil, which can be avoided by redesigning the cooling passage configuration.
- In our simulations, the creep strain increment was isotropic. If data are available for the creep strain in different crystallographic directions, it is possible to use Hill anisotropy with this creep routine to more accurately model the material behavior.

6.2 MATERIAL TESTING

In conjunction with model development, laboratory-scale experimental validation was executed to validate our hypothesis (section 5.1). APS YSZ / MCrAlY coated single crystal (Rene Ń5) coupons were exposed isothermally in air at 900, 1000, 1100^{o}C with and without compressive load for 100, 300, 600, 1000 and 3000 hours.

6.2.1 SEM and EDX observations

- First failure was found at 600 hours and 1100^{o}C, where delamination between the bond coat and the YSZ occurred in one of the six exposed samples.
- All 1100^{o}C samples featured extensive network of cracks within the TGO / YSZ at their edges, extending further that 1 mm.
- Failure did not occur up to 1000 hours exposure at 900 and 1000^{o}C.
- Bond coat porosity was found to eliminate faster under stress; however, after sufficiently long time both stressed and non-stressed samples would achieve the same dense coating.
- Apart from the influence on the bond coat porosity, there was no evidence that stresses up to 270MPa can significantly affect the performance of the coating system, thus disproving our hypothesis.
- After 600 hours at 1100^{o}C, an important distinction was made that oxide scales over well depleted β-NiAl phase zones of the bond coat had thicker scale but fewer and smaller cracks than scales over less depleted zones, which had more interface imperfections and formed chromium and cobalt oxides with the alumina scale.

- On the other hand, β-phase depletion in the bond coat was not uniform either between the samples or within the sample. No direct correlation could be made between the depletion and test conditions (induced stress in the sample).

6.2.2 Nanoindentation Material Testing

Nanoindentation was used to study the local mechanical properties (Young's modulus and hardness) of the components in the TBC system and their evolution with temperature and exposure time. Particular interest was placed on five regions: substrate bulk (SB), substrate interface diffusion zone with the bond coat (SI), bond coat bulk (BCB), bond coat interface diffusion zone with the TGO (BCI), and the bulk of the top coat (TC). At least thirty indentations were executed at each location to obtain a good average value.

- The modulus of the bulk YSZ showed a decrease at 900 and 1000^{o}C. At 1100^{o}C there was an initial decrease followed by a steady increase to 600 hours, where both stressed and non-stressed samples attained the same modulus.
- The moduli of the substrate and substrate interface within each sample were very close at all temperatures and exposure times. However, there was variation between the samples showing strong modulus dependence on the substrate crystal orientation.
- The modulus of BCB and BCI in the "as processed" state are essentially the same because of the large deviation in the measured values - 199.8 (+/- 15.1) GPa and 189.6 (+/- 19.6) GPa respectively, which is expected for the two phase coating. These values agree well with modulus values for MCrAlY bond coats in the "as processed" condition at room temperature from literature.

- At the lower temperatures, stressed samples reached a higher modulus in BCI quicker than the non-stressed samples. Ultimately, at 1100^{o}C after 300 hours modulus were the same.
- At 1100^{o}C, from 100 to 600 hours, both the BCB and BCI showed a steady increase in modulus with approximately the same slope, attaining an average of ~240 and ~272 GPa, respectively, at 600 hours. The deviation in the modulus in BCI at this point was lower than in the BCB.
- A significant increase (~65 GPa) was measured in the modulus of the interface region (BCI), where it was inferred that the β-phase is depleted and γ-phase is predominant. This increase was observed from 100 to 1000 hours for 900^{o}C, 100 to 300 hours for 1000^{o}C, and 0 to 100 hours at 1100^{o}C, thus showing temperature and time dependences. This result is significantly different from reported data, where for their particular systems different authors had found, a decrease in the modulus as the β- → γ-phase transformation occurs. In our case the local properties of the coating layer close to the interface with the oxide scale cannot be simply explained by the β- → γ-phase transformation. In order to explain this particular modulus increase and to further characterize the material phase composition, a transmission electron microscope study would be appropriate.

APPENDIX A

DAMAGE EQUIVALENT STRESS

From eq. (18), expressing $\sigma_{ij} S_{ijkl} \sigma_{kl} \rightarrow \sigma_i S_{ij} \sigma_j$, also using cubic material symmetry:

$$\left|\sigma_1\ \sigma_2\ \sigma_3\ \sigma_4\ \sigma_5\ \sigma_6\right| \begin{bmatrix} S_{11} & S_{12} & S_{12} & 0 & 0 & 0 \\ S_{12} & S_{11} & S_{12} & 0 & 0 & 0 \\ S_{12} & S_{12} & S_{11} & 0 & 0 & 0 \\ 0 & 0 & 0 & S_{44} & 0 & 0 \\ 0 & 0 & 0 & 0 & S_{44} & 0 \\ 0 & 0 & 0 & 0 & 0 & S_{44} \end{bmatrix} \begin{vmatrix} \sigma_1 \\ \sigma_2 \\ \sigma_3 \\ \sigma_4 \\ \sigma_5 \\ \sigma_6 \end{vmatrix} =$$

$$= \left|\sigma_1 S_{11} + \sigma_2 S_{12} + \sigma_3 S_{12} \quad \sigma_1 S_{12} + \sigma_2 S_{11} + \sigma_3 S_{12} \quad \sigma_1 S_{12} + \sigma_2 S_{12} + \sigma_3 S_{11} \quad \sigma_4 S_{44} \quad \sigma_5 S_{44} \quad \sigma_6 S_{44}\right| \begin{vmatrix} \sigma_1 \\ \sigma_2 \\ \sigma_3 \\ \sigma_4 \\ \sigma_5 \\ \sigma_6 \end{vmatrix} =$$

$$= \sigma_1^2 S_{11} + \sigma_1\sigma_2 S_{12} + \sigma_1\sigma_3 S_{12} + \sigma_1\sigma_2 S_{12} + \sigma_2^2 S_{11} + \sigma_2\sigma_3 S_{12} + \sigma_1\sigma_3 S_{12} + \sigma_2\sigma_3 S_{12} + \sigma_3^2 S_{11} +$$
$$\sigma_4^2 S_{44} + \sigma_5^2 S_{44} + \sigma_6^2 S_{44} =$$
$$= \left(\sigma_1^2 + \sigma_2^2 + \sigma_3^2\right) S_{11} + 2\left(\sigma_1\sigma_2 + \sigma_1\sigma_3 + \sigma_2\sigma_3\right) S_{12} + \left(\sigma_4^2 + \sigma_5^2 + \sigma_6^2\right) S_{44} =$$
$$= \left(\sigma_{11}^2 + \sigma_{22}^2 + \sigma_{33}^2\right) S_{1111} + 2\left(\sigma_{11}\sigma_{22} + \sigma_{11}\sigma_{33} + \sigma_{22}\sigma_{33}\right) S_{1122} + 4\left(\sigma_{23}^2 + \sigma_{13}^2 + \sigma_{12}^2\right) S_{2323} \tag{A 1}$$

$$S_{ijkl}\delta_{ij}\delta_{kl} = 3S_{1111} + 6S_{1122} \tag{A 2}$$

For uniaxial loading case:

$$\sigma_{11} = \sigma^* \tag{A 3}$$

$$\sigma_H = \frac{\sigma_{kk}}{3} = \frac{\sigma_{11}}{3} = \frac{\sigma^*}{3} \tag{A 4}$$

$$\sigma_{ij}^D = \sigma_{ij} - \sigma_H \delta_{ij} \rightarrow \sigma_{11}^D = \sigma_{11} - \frac{\sigma_{11}}{3} = \frac{2}{3}\sigma_{11} = \frac{2}{3}\sigma^* \tag{A 5}$$

$$\sigma_{22}^D = \sigma_{33}^D = 0 - \frac{\sigma_{11}}{3} = -\frac{\sigma^*}{3} \tag{A 6}$$

$$\sigma_{12}^D = \sigma_{13}^D = \sigma_{23}^D = 0 \tag{A 7}$$

Using equation (21) for the energy density release rate:

$$Y = \frac{1}{2(1-D)}\left[\left(\sigma_{11}^{D^2} + \sigma_{22}^{D^2} + \sigma_{33}^{D^2} + \frac{\sigma_{kk}^2}{3}\right)S_{1111} + 2\left(\sigma_{11}^D\sigma_{22}^D + \sigma_{11}^D\sigma_{33}^D + \sigma_{22}^D\sigma_{33}^D + \frac{\sigma_{kk}^2}{3}\right)S_{1122} + 4\left(\sigma_{23}^{D^2} + \sigma_{13}^{D^2} + \sigma_{12}^{D^2}\right)S_{2323}\right] =$$

$$= \frac{1}{2(1-D)}\left[\left(\frac{4}{9}+\frac{1}{9}+\frac{1}{9}\right)\left(\sigma^*\right)^2 S_{1111} + 2\left(\left(\frac{2}{3}\right)\left(-\frac{1}{3}\right)+\left(\frac{2}{3}\right)\left(-\frac{1}{3}\right)+\left(-\frac{1}{3}\right)\left(-\frac{1}{3}\right)\right)\left(\sigma^*\right)^2 S_{1122} + 4S_{2323}(0)\left(\sigma^*\right)^2\right] +$$

$$+ \frac{1}{2(1-D)}\left[\frac{\left(\sigma^*\right)^2}{9}\left(3S_{1111} + 6S_{1122}\right)\right] =$$

$$= \frac{1}{2(1-D)}\left[\frac{2}{3}\left(\sigma^*\right)^2 S_{1111} - \frac{2}{3}\left(\sigma^*\right)^2 S_{1122} + \frac{\left(\sigma^*\right)^2}{3}S_{1111} + \frac{2}{3}\left(\sigma^*\right)^2 S_{1122}\right] =$$

$$= \frac{1}{2(1-D)}S_{1111}\left(\sigma^*\right)^2 = \frac{1}{2(1-D)}S_{11}\left(\sigma^*\right)^2 \tag{A 8}$$

APPENDIX B

USER CREEP-FATIGUE ROUTINE

```
*deck,usercreep       parallel  user
      SUBROUTINE usercreep (impflg, ldstep, isubst, matId , elemId,
     &                      kDInPt, kLayer, kSecPt, nstatv, nprop,
     &                      prop  , time  , dtime , temp  , dtemp ,
     &                      toffst, Ustatev, creqv , pres  , seqv  ,
     &                      delcr , dcrda)
c**********************************************************************
c     input arguments
c     ===============
c      impflg   (in ,sc   ,i)            Explicit/implicit integration
c                                        flag (currently not used)
c      ldstep   (in ,sc   ,i)            Current load step
c      isubst   (in ,sc   ,i)            Current sub step
c      matId    (in ,sc   ,i)            number of material index
c      elemId   (in ,sc   ,i)            Element number
c      kDInPt   (in ,sc   ,i)            Material integration point
c      kLayer   (in ,sc   ,i)            Layer number
c      kSecPt   (in ,sc   ,i)            Section point
c      nstatv   (in ,sc   ,i)            Number of state variables
c      nprop    (in ,sc   ,i)            size of mat properties array
c
c      prop     (dp ,ar(*),i)            mat properties array
c                                        This array is passed all the creep
c                                        constants defined by command
c                                        TBDATA associated with TB,CREEP
c                                        (do not use prop(13), as it is used
c                                        elsewhere)
c                                        at temperature temp.
c      time                              Current time
c      dtime                             Current time increment
c      temp                              Current temperature
c      dtemp                             Current temperature increment
c      toffst   (dp, sc,   i)            temperature offset from absolute zero
c      seqv     (dp ,sc  , i)            equivalent effective stress
c      creqv    (dp ,sc  , i)            equivalent effective creep strain
c      pres     (dp ,sc  , i)            hydrostatic pressure stress, -(Sxx+Syy+Szz)/3
c
c     input output arguments             input desc     / output desc
c     ======================             ==========       ===========
c      Ustatev  (dp,ar(*), i/o)          user defined iinternal state variables at
c                                        time 't' / 't+dt'.
c                                        This array will be passed in containing the
c                                        values of these variables at start of the
c                                        time increment. They must be updated in this
c                                        subroutine to their values at the end of
c                                        time increment, if any of these internal
```

```
c                                       state variables are associated with the
c                                       creep behavior.
c
c     output arguments
c     ================
c      delcr    (dp ,sc  , o)           incremental creep strain
c      dcrda    (dp,ar(*), o)           output array
c                                       dcrda(1) - derivitive of incremental creep
c                                                  strain to effective stress
c                                       dcrda(2) - derivitive of incremental creep
c                                                  strain to creep strain
c
c     local variables
c     ===============
c      c1,c2,c3,c4 (dp, sc, l)          temporary variables as creep constants
c      con1        (dp ,sc, l)          temporary variable
c      t           (dp ,sc, l)          temporary variable
c
c*********************************************************************
c
c --- parameters
c
#include "impcom.inc"

      INTEGER          ldstep, isubst, matId , elemId,
     &                 kDInPt, kLayer, kSecPt, nstatv,
     &                 impflg, nprop , mcomp , i

      DOUBLE PRECISION HALF, THIRD, ONE, TWO, SMALL, ONEHALF,
     &                 ZERO, TWOTHIRD, ONEDM02, ONEDM05, sqTiny, OONE,
     &                 VZERO, CZERO, HONE, HTWO, AZERO, AONE,
     &                 EPSZERO, WALKER, OEIGHT, HOUR
      PARAMETER       (ZERO       = 0.d0,
     &                 HALF       = 0.5d0,
     &                 THIRD      = 1.d0/3.d0,
     &                 ONE        = 1.d0,
     &                 TWO        = 2.d0,
     &                 SMALL      = 1.d-08,
     &                 sqTiny     = 1.d-20,
     &                 ONEDM02    = 1.2d-02,
     &                 ONEDM05    = 1.d-05,
     &                 ONEHALF    = 1.5d0,
     &                 TWOTHIRD   = 2.0d0/3.0d0,
     &                 mcomp      = 6,
     &                 i          = 8.d0,
     &                 OONE       = 4.d0,
     &                 VZERO      = 12.2d0,
     &                 CZERO      = 4.3d-04,
     &                 HONE       = 9.98d+03,
     &                 HTWO       = 47.9d+03,
     &                 AZERO      = 4250d+06,
     &                 AONE       = 8.d-02,
     &                 EPSZERO    = 1.06d+20,
     &                 WALKER     = 7.7d-01,
     &                 OEIGHT     = 8.d-01,
     &                 HOUR       = 3.6d+03)

      DOUBLE PRECISION dtime , time  , temp  , dtemp , toffst,
     &                 creqv , seqv  , pres
      DOUBLE PRECISION prop(*), dcrda(*), Ustatev(nstatv)

      EXTERNAL         get_ElmData
      DOUBLE PRECISION sigElp(mcomp), dsdeEl(mcomp,mcomp), G(mcomp),
     &                 sigDev(mcomp), JM    (mcomp,mcomp), dfds(mcomp),
     &                 sigv  (mcomp), strainEl(mcomp)

c
c --- local variables
c

      DOUBLE PRECISION c1    , c2    , c3    , c4    ,
```

```
     &                con1  , delcr , t     , c11   ,
     &                c12   , c44   , uts   , smine ,
     &                con2  , con3  , con4  , con5  ,
     &                skk   , str   , con6  , CM    ,
     &                wf    , Tr    , w     , seff  ,
     &                de1   , D     , con7  , dw    ,
     &                CE    , con8  , con9  , de2   ,
     &                de3   , de4   , de1ds , de2ds ,
     &                de3ds , de4ds , SY01  , EPSDOT,
     &                fcon1 , fcon2 , dwfat , fcon3 ,
     &                fcon4 , dwfat2 , dwfat3 , fcon5 ,
     &                fcon6
c
c
c
c**********************************************************************
c
c     if (seqv.LE.ZERO.AND.creqv.LE.ZERO) GO TO 550
c
c --- Calculation of damage equivalent stress (str)
c
      call get_ElmData ('SIG', elemId,kDInPt, mcomp, sigv)
c
      sigdev(1) = sigv(1)+pres
      sigdev(2) = sigv(2)+pres
      sigdev(3) = sigv(3)+pres
      sigdev(4) = sigv(4)
      sigdev(5) = sigv(5)
      sigdev(6) = sigv(6)
c
      skk = sigv(1) + sigv(2) + sigv(3)
c
      con2 =
     &  sigdev(1)*sigdev(1) + sigdev(2)*sigdev(2) +
     &  sigdev(3)*sigdev(3)
c
      con3 = (skk*skk)*THIRD
c
      con4 =
     & sigdev(1)*sigdev(2) + sigdev(1)*sigdev(3) +
     & sigdev(2)*sigdev(3)
c
      con5 =
     & sigdev(4)*sigdev(4) + sigdev(5)*sigdev(5) +
     & sigdev(6)*sigdev(6)
c
      con6 =
     & (prop(2)*two*(con4 + con3) +
     & two*two*con5*prop(3))/prop(1)
c
      str = sqrt( con2 + con3 + con6 )
c
c --- Calculation of time to rupture (Tr) and effective stress (seff)
      CM =
     & ONE / (Ustatev(10) * exp( Ustatev(15)/Ustatev(16) /
     & temp) + Ustatev(11) * exp( - ustatev(15) /
     & Ustatev(16) / temp))
c
      con7 = prop(4)-str
c
      IF (con7 . LE . ZERO) GO TO 550
c
      IF (str . GE . prop(4)) GO TO 550
c
      wf = (prop(4) - str) / prop(4)
c
      IF (wf . LE . ZERO) GO TO 550
c
      IF (Ustatev(19) . GE . wf) GO TO 550
c
      Tr =
```

```
     & exp( (Ustatev(13)+1) * log(prop(4)-str) -
     & Ustatev(13)*log(str) - log(CM*(ustatev(13)+ONE)*prop(4)))
c
      IF (time . GE . Tr) GO TO 600
c
      IF (Ustatev(19) . GE . ONE) GO TO 700
c
      seff =
     & str/(ONE - Ustatev(19))
c
c --- Calculation of the strain increment
c
      de1 = ZERO
c
c     &4.525d-21*(seqv**4.525d-01)*exp(Ustatev(15)/Ustatev(16)/temp)*
c     &(time**3.d-01)
c
      de2 = ZERO
c
c     &4.525r-21*(seqv**4.525d-01)*exp(Ustatev(15)/Ustatev(16)/temp)*
c     &((time - dtime)**3.d-01)
c
      de3 =
     &9.72d+08*((seqv/(prop(4)-seqv))**Ustatev(26))*
     &exp(-Ustatev(15)/Ustatev(16)/temp)*(time)
c
      de4 =
     &9.72d+08*((seqv/(prop(4)-seqv))**Ustatev(26))*
     &exp(-Ustatev(15)/Ustatev(16)/temp)*(time-dtime)
c
      delcr = de1 - de2 + de3 - de4
c
c --- fatigue strain rate dependance
c
      EPSDOT = delcr / dtime
c
      IF (EPSDOT . EQ . ZERO) GO TO 310
c
      IF (EPSDOT . LT . ONEDM02) EPSDOT = ONEDM02
c
      fcon1 = (EPSDOT / EPSZERO)**(-AONE)
c
      fcon2 = (one - fcon1 * exp(-HTWO/Ustatev(16)/temp))
c
      SY01 = AZERO * exp(-HONE/Ustatev(16)/temp) * fcon2
c
      if (SY01 . LE . ZERO) GO TO 310
c
      GO TO 320
c
 310  SY01 = OEIGHT * prop(4)
c
 320  continue
c
c --- fisrt fatigue function state variables R-27(inpt),Hz-28(inpt),dam-29(out)
c
      IF (Ustatev(29) . GE . ONE) GO TO 350
c
      fcon3 = (ONE - Ustatev(28))**WALKER
c
      fcon4 = Ustatev(27) * HOUR * dtime
c
      dwfat =
     & fcon4 * CZERO *
     & (str * fcon3 / SY01 / (ONE - Ustatev(29)))**VZERO
c
      Ustatev(29) = Ustatev(29) + dwfat / OONE
c
      GO TO 360
c
 350  continue
```

```
c
      Ustatev(29) = ONE
c
 360  continue
c
c --- second fatigue function state variables R-21(inpt),Hz-20(inpt),dam-22(out)
c
      IF (Ustatev(22) . GE . ONE) GO TO 400
c
      fcon5 = (ONE - Ustatev(21))**WALKER
c
      fcon6 = Ustatev(20) * HOUR * dtime
c
      dwfat2 =
     & fcon6 * CZERO *
     & (str * fcon5 / SY01 / (ONE - Ustatev(22)))**VZERO
c
      Ustatev(22) = Ustatev(22) + dwfat2 / OONE
c
      GO TO 410
c
 400  Ustatev(22) = ONE
c
 410  continue
c
c --- third fatigue function state variables R-0,Hz-2.78e-4(1cyc/h),dam-7(out)
c
      IF (Ustatev(7) . GE . ONE) GO TO 440
c
      c1 = (ONE - ZERO)**WALKER
c
      c2 = 2.778d-04 * HOUR * dtime
c
      dwfat2 =
     & c2 * CZERO *
     & (str * c1 / SY01 / (ONE - Ustatev(7)))**VZERO
c
      Ustatev(7) = Ustatev(7) + dwfat2 / OONE
c
      GO TO 450
c
 440  Ustatev(7) = ONE
c
 450  continue
c  ---  fourth  fatigue  function  state  variables  R-0.33(inpt),Hz-4.6296e-5(1cyc/6h),dam-
c 8(out)
c
      IF (Ustatev(8) . GE . ONE) GO TO 480
c
      c3 = (ONE - 3.33d-01)**WALKER
c
      c4 = 4.6296d-05 * HOUR * dtime
c
      dwfat2 =
     & c4 * CZERO *
     & (str * c3 / SY01 / (ONE - Ustatev(8)))**VZERO
c
      Ustatev(8) = Ustatev(8) + dwfat2 / OONE
c
      GO TO 490
c
 480  Ustatev(8) = ONE
c
 490  continue
c
c --- Calculations of creep damage evolution
c
      con8 = log(CM) + (Ustatev(13) * log(seff/(prop(4)-seff)))
c
      dw = exp( con8 ) * dtime
c
```

```
      Ustatev(19) = Ustatev(19) + dw / OONE
c
      IF (Ustatev(19) . GT . ONE) GO TO 700
c
      IF (Ustatev(19) . GE . wf) GO TO 700
c
      GO TO 800
c
 550  continue
c
 600  continue
c
 700  continue
c
c --- Values of parameters if failure occurs by creep
c
      Ustatev(19) = ONE
c
      dw = ZERO
c
      delcr = ZERO
c
      de1 = ZERO
c
      de2 = ZERO
c
      de3 = ZERO
c
      de4 = ZERO
c
      wf = ONE
c
c     GO TO 900
c
 800  continue
c
c --- calculating derivative of delcr wrt seqv
c
      de1ds = de1 * Ustatev(7) / seqv
c
      de2ds = de2 * Ustatev(7) / seqv
c
      de3ds = de3 * Ustatev(26) * prop(4) / seqv / (prop(4) - seqv)
c
      de4ds = de4 * Ustatev(26) * prop(4) / seqv / (prop(4) - seqv)
c
 900  dcrda(1) = de1ds - de2ds + de3ds - de4ds
c
      dcrda(2) = ZERO
c
c --- Output
c
      D = Ustatev(19)/wf
c
      Ustatev(25) = creqv
      Ustatev(1) = D
      Ustatev(2) = str
      Ustatev(3) = seff
      Ustatev(4) = Ustatev(19)
      Ustatev(5) = Ustatev(22)
      Ustatev(6) = Ustatev(29)
      Ustatev(9) = Tr
c
 990  continue
c
      return
      end
```

Sample input for the creep-fatigue routine as it was used in our simulations:

```
tb,creep,1,7,4,100

tbtemp,773
tbdata,1, 0.093532e-10, -0.035542e-10, 0.098191e-10, 1020e+6

tbtemp,873
tbdata,1, 0.0962e-10,-0.0365e-10, 0.1019e-10, 1060e+6

tbtemp,1073
tbdata,1, 0.1031e-10, -0.0392e-10, 0.1092e-10, 1200e+6

tbtemp,1123
tbdata,1, 1.051e-11, -3.9949e-12, 1.1146e-11, 1170e+6

tbtemp,1173
tbdata,1, 1.071e-11, -4.06985e-12, 1.13725e-11, 1050e+6

tbtemp,1273
tbdata,1, 0.1111e-10, -0.0422e-10, 0.1183e-10, 770e+6

tbtemp,1373
tbdata,1, 0.1163e-10, -0.0442e-10, 0.1221e-10, 480e+6


tb,statev,1,,30
tbdata,1,0, 0, 0, 0,0
tbdata,6, 0, 0, 0, 0
tbdata,10, 3.1e-10, 2.63e+12, 1.66e-7, 3.2, 4.0
tbdata,15, 278e+3, 8.314472,0,0,0
tbdata,20, 100,0.95,0, 0, 0
tbdata,26, 4, 100, 0.85, 0, 0
```

BIBLIOGRAPHY

[1] R.A.Dennis, “FE Research Direction – Thermal Barrier Coatings and Health Monitoring Techniques,” Workshop on Advanced Coating Materials and Technology for Extreme Environments, Pennsylvania State University, State College, PA, September 12 - 13, 2006.

[2] Mazzotta D.W., Chyu M.K., Siw S., Karaivanov V.G., Slaughter W.S., Alvin M.A., 2008, “Gas-Side Heat transfer in Syngas, Hydrogen-fired and Oxy-fuel Turbines”, GT2008-51474 in preparation for *Proceedings of ASME Turbo Expo*, Berlin, Germany

[3] Alvin, M.A., Pettit, F., Meier, G, Yanar, N., Chyu, M., Mazzotta, D., Slaughter, W., Karaivanov, V., Kang, B, Feng, C., Chen, R., and Fu, T.C., “Materials and Component Development for Advanced Turbine Systems,” 5th International Conference on Advances in Materials Technology for Fossil Power Plants, Marco Island, Florida, October 2-5, 2007.

[4] Reed R.C., 2006, "*The Superalloys Fundamentals and Applications*", Cambridge University Press, Cambridge CB2 2RU, UK.

[5] Gleeson B., 2006 “Thermal Barrier Coatings for Aeroengine Applications”, Journal of propulsion and power, vol.22, No2, pp. 375-383.

[6] Bose S., 2007, "*High Temperature Coatings*", Butterworth-Heinemann

[7] Mazzotta D.W., Chyu M.K., Alvin M.A., 2007, “Airfoil heat transfer characteristics in syngas and hydrogen turbines”, GT2007-28296 *Proceedings of ASME Turbo Expo*, Montreal, Canada.

[8] Evans A.G., Mumm D.R., Hutchinson J.W., meier G.H., Pettit F.S., "Mechanisms Controling the Durability of Thermal Barrier Coatings", Progress in Materials Science 46, 505-553, 2001.

[9] Schlichting K.W., Padture N.P., Jordan E.H., Gell M., "Failure Modes in Plasma-sprayed Thermal Barrier Coatings", Materials Science and Engineering A342, 120-130, 2003.

[10] Echsler H., Renusch D., Schutze M., “Bond coat oxidation and its significance for life expectancy of thermal barrier coating systems”, 2004, Material science and technology, vol. 20, pp. 307-318.

[11] Bhadeshia H.K.D.H. Nickel based superalloy: dislocation structure. http://www.msm.cam.ac.uk/phase-trans/2002/Zhang.html

[12] MacLachlan, D.W. and Knowles, D.M., 2001, "Modelling and Prediction of the Stress Rupture Behaviour of Single Crystal Superalloys", Materials Science and Engineering A302, pp. 275–285.

[13] Matan N., Cox D.C., Carter P., Rist M.A., Rae C., Reed R.C., "Creep of cmsx4 superalloy sinle grystals : Effects of misorientation and temperature", Acta mater., vol 47, No5, pp. 1549-1563, 1999.

[14] MacLachlan, D.W. and Knowles, D.M., 2000, "Creep-Behavior Modeling of the Single-Crystal Superalloy CMSX-4", Metallurgical and materials transactions 31A, pp. 1401-1411.

[15] MacLachlan, D.W., Wright L.W., Gunturi S. and Knowles, D.M., 2001, "Constitutive modeling of anisotropic creep deformation in single crystal blade alloys SRR99 and CMSX-4", International Journal of Plasticity 17, pp. 441-467.

[16] MacLachlan D.W., Knowles D.M., 2001, "Fatigue behaviour and lifing of two single crystal superalloys", Fatigue Fract Engng Mater Struct 24, 503-521.

[17] Chaboche J.-L., Gallerneau F., 2001, "An Overview of the Damage Approach of Durability Modeling at Elevated Temperature", Fatigue Fract Engng Mater Struct 24, pp. 405-418.

[18] Lemaitre, J., 1984, "How to Use Damage Mechanics", Nuclear Engineering and Design 80**,** pp. 233-245.

[19] Kachanov, L.M., 1986, *Introduction to Continuum Damage Mechanics*, Kluwer academic publisher group*,* Dordrecht*.*

[20] Lemaitre, J. and Desmorat, R., 2005, *Engineering damage mechanics,* Springer-Verlag Berlin Heidelberg*,* New York*.*

[21] Lemaitre, J., 1996, *A course on Damage Mechanics*, Springer-Verlag Berlin Heidelberg*,* New York.

[22] Cunha, F.J., Dahmer, M.T., and Chyu, M.K., 2005, "Thermal-Mechanical Life Prediction System for Anisotropic Turbine Components", *Proceedings of ASME Turbo Expo*, Reno, U.S.A..

[23] Chen L., Liu Y., Xie L., "Power-exponent function model for low-cycle fatigue life prediction and its applications – Part II: Life prediction of turbine blades under creep–fatigue interaction", 2007, International Journal of Fatigue, 29, pp. 10–19.

[24] Browell R., "Update on the ANSYS Fatigue Module," ANSYS solutions, vol.7, issue 1, 2006, www.ansys.com

[25] Claudio R.A. et al., "Fatigue Life Prediction and Failure Analysis of a Gas Turbine Disc Using the Finite Element Method," Fatigue and Fracture of Engineering Materials and Structures 27, pp. 849-860.

[26] Thulin R.D., Howe D.C., Singer I.D., 1984, "NASA Energy Efficient Engine. High-Pressure Turbine Detailed Design Report", NASA CR-165608.

[27] Karaivanov V.G., Mazzotta D.W., Chyu M.K., Slaughter W.S., "Three-dimensional Modeling of Creep Damage in Airfoils for Advanced Turbine Systems", GT2008-51278, Proceedings of ASME Turbo Expo, Berlin, Germany, 2008.

[28] Mills, K., 2002, *Recommended values of thermo-physical properties for selected commercial alloys,* Woodhead Publishing Limited, Abington Hall, Abington Cambridge CBl 6AH, England.

[29] Scott H.G. "Phase relationships in the zirconia-yttria system" Journal Of Materials Science 10 (1975) 1527-1535.

[30] Trice R.W., Su J., Mawdsley J.R., Faber K.T., De Arellano-Lopez A.R., Wang H., Porter W.D. "Effect of heat treatment on phase stability, microstructure, and thermal conductivity of plasma sprayed YSZ." Journal of materials science 37 (2002) 2359-2365.

[31] Helminiak M.A., Yanar N.M., Pettit F.S., Meier G.H., Taylor T.A. " Advanced APS Thermal Barrier Coatings" 23rd Annual Conference on Fossil Energy Materials, Pittsburgh, PA, May 12-14, 2009.

[32] Busso E.P. et al., "A physics-based life prediction methodology for thermal barrier coating systems", 2007, Acta Materialia, 55, pp. 1491-1503.

[33] Meyer S.M., Nissley D.M., Sheffler K.D., Cruse T.A., 1992, "Thermal barrier coating life prediction model development", Journal of Engineering for gas turbines and power", vol. 114, pp. 258-263.

[34] Cook L.S., Wolfenden A., Brindley W.J. " Temperature dependence of dynamic Young's modulus and internal friction in LPPS NiCrAlY" Journal of Materials Science 29 (1994) 5104-5108.

[35] Franke O., Durst K., Goken M. "Microstucture and local mechanical properties of Pt-modified nickel aluminades on nickel-based superalloys after thermo-mechanical fatigue" Materials Science and Engineering A 467 (2007) 15-23.

[36] Li W.Z., Wang Q.M., Bao Z.B., Yao Y., Gong J., Sun C., Jiang X. "Microstructural evolution of the NiCrAlY/CrON duplex coating system and its influence on mechanical properties" Materials Science and Engineering A 498 (2008) 487-494.

[37] TriboIndenter User Manual, Hysitron Incorporated, Minneapolis, MN.

[38] Gleeson B., Mu N., Hayashi S. “Compositional factors affecting the establishment nad maintenance of Al_2O_3 scales on Ni-Al-Pt systems” Journal of Materials science, Interface science 02/2009.

[39] Wallwork G.R., Hed A.Z. "Some limiting factors in the use of alloys at high temperatures" Oxidation of Metals, Vol 3, No 2,1971.